NASA Technical Memorandum 83479

Influence of Cobalt, Tantalum, and Tungsten on the High Temperature Mechanical Properties of Single Crystal Nickel-Base Superalloys

Michael V. Nathal
Lewis Research Center
Cleveland, Ohio

January 1984

NASA

TABLE OF CONTENTS

INFLUENCE OF COBALT, TANTALUM, AND TUNGSTEN ON THE HIGH TEMPERATURE MECHANICAL PROPERTIES OF SINGLE CRYSTAL NICKEL-BASE SUPERALLOYS

Michael Victor Nathal

National Aeronautics and Space Administration
Lewis Research Center
Cleveland, Ohio 44135

INTRODUCTION

Materials for use in aircraft gas turbine engines must be able to withstand high temperatures and stresses in an aggressive environment. Nickel-base superalloys possess a suitable combination of properties for such applications. These alloys are frequently very complex, as a specific alloy may contain a dozen elemental additions. The present state of development of superalloys is the result of research on both the composition of the alloys and the processing steps necessary for fabrication of engine parts. Controlled directional solidification to form single crystal superalloys is one example of an innovation in processing that enables further improvements in engine performance. Such advances also allow further research on compositional variations to take full advantage of the new processes.

Recently, however, research and development efforts have been directed towards a new restriction on the use of gas turbine materials. Some of the most commonly used elements in superalloys, such as cobalt, chromium, tantalum, and niobium, have come to be placed in the "strategic" category of materials in that their supply and availability have become increasingly uncertain (1,2). Thus, attention has been turned toward identifying the roles which

these strategic elements play, with the goal of reducing or eliminating their content in superalloys. The research described below is directed towards the influence of cobalt, tantalum, and tungsten levels on the microstructure and high temperature strength, ductility, and creep resistance of single crystal MAR-M247.

THE METALLURGY OF NICKEL-BASE SUPERALLOYS

Phases Present in Superalloys

Nickel-base superalloys may contain a large number of alloying additions, including aluminum (Al), Chromium (Cr), Titanium (Ti), cobalt (Co), iron (Fe), molybdenum (Mo), tungsten (W), vanadium (V), niobium (Nb), tantalum (Ta), hafnium (Hf), rhenium (Re), boron (B), zirconium (Zr), and carbon (C) (3). A wide variety of alloys has resulted from the various combinations of these elements, and a general understanding of the roles of the individual elements has been reached. Superalloys consist of a face centered cubic (FCC) solid solution, γ, an ordered FCC precipitate, γ', and various minor phases such as carbides, borides, sigma(σ), and mu(μ). The γ matrix is a solid solution of Ni with substantial amounts of Cr. Other elements commonly found in the γ phase of modern superalloys include Co, W, Mo, and smaller amounts of Al and Ta. These additions serve as solid solution strengtheners of the γ phase.

Superalloys contain from 15 to 70 volume percent of γ', an ordered phase based on Ni_3Al. Ti, Nb, and Ta are common additions which replace Al atoms in γ', whereas Co substitutes solely for Ni. Tungsten, Cr, Mo, and Hf are also present to some extent in the γ' of superalloys (3,4). The γ' phase is useful for a number of reasons. The precipitate is coherent with the matrix, resulting from the small difference in lattice parameters between γ and γ'. This small mismatch, typically less than one percent, allows homogeneous nucleation of γ' and stability against coarsening at elevated temperature. Gamma prime has the unusual property of increasing strength as temperature increases (5), and also has enough inherent ductility to prevent embrittlement. Antiphase boundary (APB) strengthening, which arises from the ordered $L1_2$ structure, is a major strengthening contribution of γ'.

Several different carbides can be present in modern superalloys, including MC, $M_{23}C_6$, and M_6C, where M stands for the various carbide forming elements (3). Because they are preferentially located at grain boundaries, carbides retard grain boundary sliding and thus improve creep resistance of polycrystalline superalloys. However, some carbide morphologies, such as needles, plates, and grain boundary films, may reduce stress-rupture life or ductility.

Topologically Close Packed (TCP) phases such as σ and μ are also found in superalloys. These phases usually form from the γ

matrix during long time exposure at high temperatures. Because of their plate-like morphology, TCP phases are considered deleterious to mechanical properties.

Tensile Properties of Superalloys

The yield strength of nickel-base superalloys is relatively high at room temperature, and remains high up to temperatures near 750°C (6). This strength is dependent on both the properties of the individual phases and the characteristics of the dispersion of γ' precipitates. Some of the factors that may contribute to the strength include: solid solution strengthening of γ and γ', APB energy of the γ', coherency strains between γ and γ', and volume fraction, particle shape, and particle size of γ'. The relative contributions of each of these factors is dependent on the specific alloy and the testing conditions.

Solid solution hardening of γ involves the increase in flow stress resulting from changes in lattice parameter, elastic modulus, stacking fault energy, and other mechanisms (7). In concentrated solid solutions, a strengthening contribution from short range order may also exist (7,8). Titanium, Al, Cr, Mo, and W are potent hardeners of Ni, whereas Co and Fe are weak hardeners (9,10).

Solid solution hardening of γ' has also been studied (11). A major contribution to the hardening of γ' is believed to be a change in APB energy caused by elements such as Ti, Nb, and W

(12-18). A pair of dislocations is required to shear the γ' phase, whereby the APB created by the leading dislocation is annihilated by the trailing dislocation. Many workers have studied the increase in yield stress of γ' as a function of temperature (12-18). This phenomenon is considered to be the result of thermally assisted cross-slip of 1/2 <110> dislocations from {111} planes to {100} planes. It is postulated that only the leading dislocation cross-slips onto the cube plane, making the pair immobile and thereby acting as a barrier to further dislocation motion. The decrease in yield strength above 750°C is caused by the onset of primary cube slip, which is characterized by slip of both dislocations on {100} planes. Under some conditions faults other than pure APB's may be formed. For example, superlattice stacking faults produced by 1/3 <112> dislocations have been observed in several alloys (15,19-21).

Several mechanisms by which γ' precipitates act to impede dislocation motion have been proposed. For small particle sizes, the γ' particles are normally sheared by a pair of dislocations. For large particle sizes, dislocations can bypass the particles by the Orowan mechanism (22). Both shearing and bypassing have been observed in γ' strengthened alloys, sometimes in the same specimen (23,24).

In most studies (20,25-33), order hardening and coherency strain hardening are considered to be the major contributions to the strength of nickel base superalloys. Coherency hardening

arises from the elastic interaction between the strain fields of the dislocations and precipitates, which results from the lattice parameter mismatch between γ and γ' (7,34). Order hardening arises from the APB created by shearing of the γ' particles. Modulus hardening, which results from the difference in modulus between the two phases (7,35), has only been proposed by one author (27). Hardening associated with the creation of new surface by shearing of the particles, and with differences in stacking fault energies of the precipitate and matrix are considered to be negligible (7,36).

Creep Properties of Superalloys

Creep processes often limit the useful life of turbine materials. These processes are important at temperatures in excess of about one half of the absolute melting point. Creep deformation is frequently described by an equation of the form:

$$\dot{\varepsilon}_s = A\ \sigma_a^{\ n} \exp \frac{-Q}{RT} \qquad [1]$$

where $\dot{\varepsilon}_s$ is the steady state strain rate, σ_a is the applied stress, n is the stress exponent, Q is the activation energy for the deformation process, R is the gas constant, T is the absolute temperature, and A is a constant that depends on the structure of the material and the deformation mechanism involved. The specific mechanisms which occur under a given set of conditions can be identified by the stress exponent n and activation energy Q.

Sherby and co-workers (37-40) have demonstrated that Q is frequently equal to the activation energy for self diffusion, resulting in the replacement of the exponential term in Equation [1] with the diffusion coefficient D. The bulk diffusion coefficient is most frequently used, but grain boundary or dislocation pipe diffusion may also be applied for certain mechanisms. The equivalence of the activation energies is contingent upon the temperature dependence of the elastic modulus (E). Equation [1] is modified to account for the modulus effect in Equation [2].

$$\dot{\varepsilon}_s = A_2 \frac{\sigma_a^n}{E} \exp \frac{-Q}{RT} \qquad [2]$$

An additional pre-exponential term was also found to improve the representation of creep data (40-42), producing Equation [3],where b is the Burgers vector.

$$\dot{\varepsilon}_s = A_3 \frac{Eb}{RT} \frac{\sigma_a^n}{E} \exp \frac{-Q}{RT} \qquad [3]$$

In some cases, particularly at high stresses, the power law dependence of creep rate on stress does not hold. In this case, an exponential or hyperbolic sine function is frequently more appropriate. This is often called the power law breakdown region and is described by Equation [4], where B is another constant (38).

$$\dot{\varepsilon}_s = A_4 \exp (B\sigma_a) \exp \frac{-Q}{RT} \qquad [4]$$

Creep in superalloys occurs by a combination of thermally assisted dislocation motion within the grains and diffusional flow involving grain boundaries. The creep rupture strength of superalloys is dependent on the following parameters: grain size and shape, grain boundary precipitates, γ and γ' strength, diffusivity of γ and γ', γ' volume fraction, γ' precipitate size, and phase stability.

Nabarro-Herring (43,44) and Coble (45) creep, which involve diffusional flow from transverse to longitudinal grain boundaries, can contribute to the creep of superalloys. Grain boundary sliding, which occurs in conjunction with other mechanisms to maintain grain continuity, or as an independent mechanism, is also important (46,47). Superalloys are designed to minimize the contribution from these mechanisms. Carbide morphology at grain boundaries is a primary consideration. Carbide particles can act to pin the grain boundaries and thus are beneficial to creep resistance (5). However, continuous grain boundary films and acicular morphologies are considered deleterious (5,48). The morphology of grain boundary γ' is also important. A γ' film along boundaries is believed to retard creep crack propagation (49,50).

Diffusional creep may produce γ' denuded zones at transverse grain boundaries, which provide preferred sites for cracking (51,52). Minute additions of B and Zr, which segregate to grain boundaries, have produced dramatic improvements in creep rupture life by retarding the formation of denuded zones (53). Hafnium is

also considered to be a grain boundary strengthener, and has a strong influence on the formation of grain boundary carbides and γ' (50,54-56). Hafnium, Zr and B also have significant roles in the prevention of sulfur and oxygen embrittlement (56).

Finally, an important method for improving the resistance to grain boundary creep is to control the grain size. Increasing the grain size can increase the creep resistance of an alloy, although section size effects many obscure this trend (5). In addition, improved strength, creep resistance, and ductility can be attained by directional solidification to produce columnar grains (57,58). These improvements are related to the elimination of weak transverse grain boundaries and to the preferred [100] orientation developed during solidification.

Single crystal superalloys have been developed as an improvement over the columnar grained superalloys. Although a superalloy in single crystal form had only minor advantages over the same alloy in columnar grained form, alloys designed specifically for single crystal applications exhibited more significant improvements in properties (59-62). One major adjustment involves the removal of the grain boundary elements C, B, Zr, and Hf, which are no longer necessary for single crystals. This adjustment causes a significant increase in the incipient melting temperature, which allows higher heat treatment temperatures that can completely dissolve the coarse γ' present in as-cast structures, followed by reprecipitation of the γ' as a fine dispersion (59). In addition

to the removal of the grain boundary elements, other compositional variations are being developed (59,63).

In addition to grain boundary strengthening, superalloys are also designed to have a resistance to dislocation creep mechanisms. A dispersion of γ' particles is an effective means of reducing the rate at which dislocations can move through the crystals. At high stresses, dislocations may shear through or loop around the γ' particles, as discussed for the higher strain rate tensile properties. At lower stresses, bypassing of the particles by climb is also possible (64,65).

Superalloys are similar to other two phase alloys in that their behavior deviates from the behavior of single phase pure metals and alloys. In the dislocation creep or "power-law creep" regime, single phase materials are characterized by stress exponents in the range of 3-5 and activation energies equal to that of self diffusion. These stress exponents are relatively well understood in terms of models based on climb controlled (66-68) and viscous glide controlled (41,42,68) mechanisms. However, alloys hardened by a second phase exhibit stress exponents much greater than five, sometimes as great as 40 for oxide dispersion strengthened (ODS) alloys (69,70). In addition, activation energies much greater than that for diffusion are also measured.

One approach that is frequently used to explain these high n and Q values is the concept of an effective stress(σ_e) (70-81).

$$\sigma_e = \sigma_a - \sigma_i \qquad [5]$$

Here σ_i is an internal stress, also termed a "back stress," "friction stress," "threshold stress" or "resisting stress." This internal stress is considered to be a measure of the resistance of the material to deformation, and it has been applied to both single and two-phase alloys. If the creep rate is plotted as a function of σ_e rather than σ_a, the desired results of reducing n and Q to levels appropriate for simple alloys are frequently obtained. The internal stress is considered to arise from a combination of dislocation substructure, second phase particles, and the lattice friction stress. The contribution from the precipitate has frequently been related to the Orowan stress or the stress necessary for climb around particles (64,81). In spite of the popularity of this approach, however, the area remains controversial. The major areas of conflict involve the stress decrement methods used for σ_i measurements, and the physical interpretation of the measured quantities (71,81).

An alternate approach to the problem of high n and Q values is the use of an exponential relationship instead of a power law. Equivalent or better fit of experimental data (81-83) and an improvement in Q (84) have resulted from this approach, but few authors have chosen the exponential law to represent their results.

Superalloys have exhibited n values ranging from 5 to 15 and Q values from 360 to 700 Kjoules/mole, with typical values of $n \sim 8$ and $Q \sim 500$ Kjoule/mole. In contrast, pure Ni and several binary solid solutions have exhibited $n \sim 5$ and Q equal to the activation energy for diffusion, in the range of 240 to 300 Kjoules/mole (40,85). Factors which influence the resistance to power law creep in superalloys include the solid solution elements in γ and γ', volume fraction and particle size of the γ', γ-γ' mismatch, γ' coarsening rate, and precipitation of TCP phases.

The creep strength of the γ matrix is determined by the elements in solid solution with Ni. Solid solution elements can reduce the creep rate by increasing the lattice friction stress, decreasing diffusion, and by decreasing stacking fault energy. These same mechanisms would also pertain to the deformation of the γ' phase, with the additional influence of the ordered structure.

Several workers have demonstrated that an increase in creep resistance occurs with an increase in γ' volume fraction (86-89). Consequently, many modern superalloys have volume fractions in the range of 40 to 60 percent. However, the effect of volume fraction must be balanced with other factors, as seen in the comparison of two superalloys, IN738 and IN713. Even though IN738 possesses a lower volume fraction of γ', its creep strength is somewhat higher than that of IN713 (90). In addition, optimum properties are obtained when the γ' is present as a fine dispersion rather than

the coarse particles and eutectic colonies present in cast structures (91).

An area related to the size distribution of the γ' particles is the stability of the γ' dispersion. The coarsening of γ' particles is almost always described by theories based on the Lifshitz-Slyozov-Wagner (LSW) theory of Ostwald ripening (92,93). This theory is based on diffusion controlled particle growth and predicts a $t^{1/3}$ time dependence. The $t^{1/3}$ dependence is invariably found (94-100) although some authors have noted the difficulty in distinguishing between a $t^{1/3}$ and a $t^{1/2}$ dependence. Another prediction of the LSW theory involves the particle size distribution that is approached at long aging times. The experimental size distributions frequently are significantly wider than the theoretical distribution. This discrepancy appears to be the result of a finite volume fraction of precipitate, as the LSW theory is strictly true only for zero volume fraction. Modifications of the LSW theory to incorporate the effects of volume fraction have been successful to varying degrees (101-105).

The coarsening of particles is described by the LSW theory as

$$\bar{r}^3 = \bar{r}_0^3 + Kt \qquad [6]$$

where $\bar{r}_0$ and $\bar{r}$ are the average particle sizes at times zero and t, respectively, and K is the rate constant given by:

$$K = \frac{8 \sigma Vm Ce D}{9RT} \qquad [7]$$

Here σ is the particle/matrix interfacial energy, Ce is the concentration of solutes in equilibrium with a particle of infinite radius, Vm is the molar volume of precipitate, and D is the effective diffusion coefficient of the atomic species involved. From Equation [7], it can be seen that variations in alloy composition can affect the coarsening rate by influencing σ, D, and Ce. In superalloys, the γ-γ' lattice mismatch is considered to effect σ and thus the coarsening rate (5,48). The lattice mismatch δ is given by Equation [8] with a_γ and $a_{\gamma'}$ representing the lattice parameters of the two phases.

$$\delta = 2 \frac{a_{\gamma'} - a_\gamma}{a_\gamma + a_{\gamma'}} \qquad [8]$$

The partitioning of elements between γ and γ' is related to Ce, as an element that partitions equally between γ and γ' would not be expected to strongly influence the coarsening rate, whereas an element that strongly partitions to either phase could be the rate controlling species (24).

In studies of nickel-base alloys, Davies et al. (104) showed that increasing Co level decreased the γ' coarsening rate. Although Co additions decreased δ, the authors suggested that the major influence of Co content was probably due to the change in effective diffusion coefficient. Bergman (24) observed that in-

creasing the Ti/Al ratio in a series of alloys caused a decrease in coarsening rate even though the increased Ti resulted in higher misfit values. Several other workers (87,99,100) have reached similar conclusions. Thus, there is a considerable amount of evidence that conflicts with the concept that higher lattice mismatch causes an increase in γ' coarsening rate. Some workers have suggested that increased δ values decrease the coarsening rate by providing an obstacle to the flow of atoms across the interface (99). Although this concept has not been ruled out, the influence of alloying on the diffusion coefficient and the partitioning of elements appears to be at least as important as the γ-γ' mismatch.

At sufficiently large particle sizes, the γ' can become semi-coherent with the matrix. The γ-γ' interface is then characterized by a hexagonal grid of $\frac{a}{2}$ <110> misfit dislocations (106). Weatherly and Nicholson (107,108) have discussed the nature of the misfit dislocations and the processes involving the loss of coherency. It is energetically favorable for a particle to become semi-coherent once the particle exceeds a critical size. This critical size is dependent mainly on the magnitude of δ. Once it is favorable for a particle to become semi-coherent, there are two important mechanisms by which loss of coherency can occur. The particle can capture dislocations from a source in the matrix, or it can nucleate dislocation loops by a punching mechanism. The latter mechanism requires that the coherency stresses and thus δ must exceed a critical value (107-109). Although the

sign of δ is not predicted to be important, it appears that alloys with negative δ values obtain misfit dislocations easier (110,111). The lattice mismatch also affects the spacing of the misfit dislocations, with the spacing d given by the Brooks formula (107).

$$d = \frac{b}{\delta} \qquad [9]$$

The influence of misfit dislocations on γ' coarsening rate is unclear, with evidence showing that the loss of coherency has both enhanced (110) and decreased (112,113) coarsening.

A number of workers have related creep resistance to the stability of the γ' dispersion. Coarsening of the particles during the creep test is considered to be a cause of a gradual loss in strength which results in the onset of tertiary creep and failure (80,114-118). These results are supported by tests whereby the creep life of a specimen is prolonged by heat treatments designed to restore the original particle distribution (80,115,118). Some workers have reported that the γ' coarsening during creep is the same as the coarsening during unstressed aging. However, other authors have noted that the application of a stress changes the coarsening behavior. Frequently, the coarsening γ' particles become irregularly shaped (80,115) or coarsen into rod or plate morphologies (116,117,119-123). The coarsening under an applied stress is dependent on the orientation of the grains and the sign of the applied stress. For <100> oriented single crystals of

Udimet 700, γ' plates form perpendicular to an applied tensile stress, and γ' rods form parallel to an applied compressive stress (120). Pineau (124), using the ideas of Eshelby (125,126), predicted the response of γ' shape changes under various conditions. Important factors include the lattice and elastic modulus mismatch between γ and γ'. The predictions of Pineau are consistent with some observations (120,122) but not with others (123,127,128).

The observations of particle coarsening during creep have led to the concept of alloy design to reduce this coarsening. Again, the approach of minimizing δ is often quoted (5,48,89). Although some studies have produced data in support of this concept (88,129), other studies have indicated that the reverse is true (24,87,130,131). The observation that alloys with higher mismatch had improved creep strength could be the result of both coherency strain hardening and simultaneous influences on diffusion, coarsening, and APB energy caused by the compositional variations. It is also possible that an optimal misfit which is dependent upon composition and testing conditions would exist as a balance between the effects of hardening and coarsening.

In one alloy, the coarsening of γ' was actually considered beneficial. Studies by Pearson, et al. (127,128) on an alloy with large misfit ($\delta = -0.8$ percent) showed that the γ' coarsened very rapidly into plates perpendicular to the applied stress. These plates were very finely spaced and were quite stable once they were formed (127). The formation of these plates prevented dislo-

cation bypassing of γ', and thus forced the more difficult shearing mode to operate. This is in contrast to other alloys where the coarsening occurred gradually throughout the test and was treated as an overaging process whereby bypassing was enhanced (115,116).

Another factor to consider in the analysis of these data is that δ should be measured at the testing temperature. Whereas some of the authors (20,100,104) have made the elevated temperature measurements, many performed the measurements at room temperature (24,48,87,88,128,129, 130, 131). From the data of Grose and Ansell (20), $\delta \sim +0.2$ percent would correspond to $\delta \sim 0$ at 700°C. Even after accounting for this change in misfit with temperature, the data from references 24, 87, 88, and 130 still do not indicate that a zero misfit is desirable.

It must be emphasized, however, that published experimental work is frequently limited to temperatures in the range of 600-800°C, and to alloys with γ' volume fractions less than 30 percent. Many modern superalloys are designed to contain volume fractions greater than 50 percent, and to operate at temperatures in the range of 900 to 1100°C. As temperature is increased into this range, the influence of γ' coarsening may be more pronounced. Although studies of the creep behavior of superalloys in this group have been performed (80,83,91,114-118, 127,128), no compositional studies with systematic variations in volume fraction, δ, and APB energy have been published. In addition, δ values of

these alloys are rarely reported, at least partly because the values may be unmeasurably small.

Another aspect of microstructural stability is the formation of TCP phases. The formation of these phases in polycrystalline superalloys has been shown to be deleterious to creep strength and ductility, because the acicular morphology provides interfaces for crack propagation, and also because the formation of these phases depletes the matrix of solid solution elements (5,48,132). Although no studies have been concerned with the influence of TCP phase formation in single crystal alloys, these phases are still considered undesirable.

Thus it can be seen that knowledge of the creep mechanisms of nickel-base superalloys is far from complete, and in many cases apparent contradictions between different studies are found. Much knowledge has been gained, as evidenced by the steady improvement in creep strength through alloy development. Although factors such as diffusivity, γ' volume fraction and particle size, APB energy, and γ-γ' mismatch are all widely recognized as contributing to the creep resistance of an alloy, the relative importance of each microstructural factor and their inter-relations are unclear. In addition, the affects of different alloying elements on these factors is not completely understood. It is likely that the factors controlling the creep of superalloys are strongly dependent on the composition of the alloy and the testing conditions.

Influence Of Cobalt And Tantalum In Superalloys

The role of Co on the microstructure and properties of nickel-base superalloys has received renewed attention. Reviews of early work can be found in (1,133,134). These studies found that additions of 10-20 w/o Co were beneficial for creep-rupture properties in most cases. These property changes were discussed in relation to the influences of Co on the amount of γ', the amount and type of carbides, stacking fault energy, the formation of grain boundary denuded zones, and the formation of TCP phases.

Recent work on modern polycrystalline superalloys has confirmed many of the earlier conclusions. In studies of superalloys with a range of γ' volume fractions, Waspaloy (135), Udimet-700 (136), and MAR-M247 (133,134), it was found that Co additions increased the creep resistance of the alloys but had only minor effects on tensile properties. However, it did appear that Co levels could be reduced to about one-half of the present levels in these alloys. Again, these results were related to γ' volume fraction, carbide type and morphology, and stacking fault energy.

The study of the influence of Co on MAR-M247 has produced some interesting results (133,134). Reduction of Co from 10 to 0 weight percent caused a reduction in rupture life by a factor of 3. This reduction in life was rationalized by the observed decrease in γ' volume fraction and the formation of a grain boundary carbide film as Co level was reduced. However, comparison of two

alloys in a study on single crystals (63) indicated that removal of Co actually increased the creep life. No reasons were given for the effect of Co in the single crystal alloys, and in fact, published data on single crystal alloys are quite limited. It is suggested here that the difference in the response of polycrystalline and single crystal materials is the result of the removal of the grain boundary elements, C, B, Zr, and Hf. In polycrystalline MAR-M247, Ta is present mostly in the MC carbides, whereas in the single crystal version, carbon is absent and the Ta is free to partition between the γ and γ' phases. In addition, the partitioning of Ta is influenced by Hf (137,138), which is present in the polycrystalline form and absent in the single crystal version of MAR-M247. However, the influence of Co and how it is affected by Ta level is not clear.

The role of Ta in superalloys is not well characterized. Tantalum is known to act as a solid solution hardener and a γ' former (5), but its relative effectiveness compared to other refractory elements is unclear. It is also considered to be beneficial for environmental resistance (59,139), but excessive amounts may degrade these properties (140). Because Ta segregates to interdendritic regions during solidification, it decreases the occurrence of casting defects known as "freckles" (141,142).

In summary, cobalt appears to have beneficial effects on the creep resistance of most but not all superalloys. It affects deformation processes both within grains and at grain boundaries

by influencing the formation of the several phases possible in superalloys. This influence appears to be dependent on the total composition of the specific alloy. In MAR-M247, the role of Co appears to change when grain boundary strengthening elements are removed to produce singly crystal versions. The role of Ta is also strongly influenced by the presence of grain boundary elements, but its precise role and its interaction with Co have not been investigated.

The Present Study

The primary purpose of the present study is the determination of the influence of Co and Ta on the microstructure and elevated temperature mechanical properties of a nickel-base superalloy single crystal. In addition, the correlations between composition, microstructure, and mechanical properties may provide additional insight into the basic creep mechanisms involved.

Accordingly, a matrix of compositions which formed the basis for the study was prepared and is exhibited in Table I. Alloy G is the standard MAR-M247 stripped of C, B, Zr and Hf. Nickel replaces Co to form Alloy E with 5 weight percent Co and Alloy B with 0 percent Co. The role of Ta was investigated by replacing Ta with Ni at each Co level, producing Alloys A, D and F. However, replacing Ta with another refractory element is expected to be a more likely choice for maintaining creep strength. Tungsten was chosen because it is close to Ta in the periodic table, it is

known to partition to γ' in some alloys, and it is not considered a strategic element. Consequently, W was substituted for Ta in Alloys C and H. In all of the alloys studied, Cr, Al, Ti and Mo were kept constant at the levels appropriate for MAR-M247.

MAR-M247 was chosen as the base alloy so that comparisons could be made to previous work. Alloys A, D and F are close to the compositions of the polycrystalline versions of MAR-M247 studied in (133,134). The reduced Ta levels in Alloys A, D, and F would approximate the partitioning of Ta to the carbides in the polycrystalline versions of MAR-M247. Alloy B is also known as NASAIR 100 (63), and Alloy E is very close to the composition of Alloy 3 in (63).

MATERIALS AND PROCEDURES

Specimen Preparation

The single crystal castings were produced by the withdrawal process in the production facilities of TRW, Inc. in Minerva, Ohio. A total of nine castings was poured, one for each of the eight compositions, and one additional casting of Alloy B. Each casting consisted of 19 cylindrical bars arranged around a central riser. The bars were handled carefully to prevent the occurrence of recrystalization during subsequent heat treatments.

A small section from the top of each bar was cut and prepared for metallographic inspection. Determination of crystal orientation by the Laue back-reflection technique was performed on the samples that were observed to be single crystals. One of the multigrained bars from each casting was used for solution treatment trials. These trials consisted of holding the specimens at a given temperature for four hours. The results of these trials revealed that the γ' in all compositions could be completely solutionized in the temperature range 1288 to 1316^{o}C. On the basis of these results, a solution temperature of 1302 $\pm$ 3^{o}C was selected for all the alloys.

A standard commercial heat treating schedule was employed for all compositions. A solution treatment batch consisted of 9 bars arranged in a single layer across a tray. After holding at 1302^{o}C for 4 hours under argon, the tray was removed and the bars were forced-air quenched to room temperature. This quench cooled the bars to a grey color in less than 2 minutes. To simulate the cycle used to apply a protective coating, an age of 982^{o}C for 5 hours was performed. The coating cycle was included in this study in order to compare the proprties and microstuctures observed in the present study with those of previous studies (59,63). A final aging treatment of 871^{o}C for 20 hours completed the heat treatments.

The bars were sandblasted and macroetched in order to detect any polycrystalline specimens. No more than three tensile specimens were machined from each bar. In many cases, the occurrence of spurious grains limited the number of tensile specimens obtained from each bar. The specimen geometry is shown in Figure 1.

Chemical analysis was performed on fully heat treated samples from the bottom of the castings, and are given in Table II. Two methods of analysis of the major elements were employed. The first method, labelled "a" in Table II, used wet chemistry techniques in combination with ion exchange separation. The second method, labelled "b" in Table II, involved wave length dispersive X-ray flourescence of bulk samples. Minor elements were deter-

mined by a spectrographic method.

Mechanical Testing

Tensile tests were performed in air at 925 and 1000°C. The 0.2 percent offset yield stress, ultimate tensile stress, percent elongation, and percent reduction in area were determined. The bars were heated to the testing temperature in approximately 1.5 hours, with less than 5°C "overheating." Two Pt/Pt-13Rh thermocouples located on the specimens were used to control the temperature to ± 3°C. The tensile tests were performed with an Instron tensile testing machine at a constant crosshead speed, with an initial strain rate of 2.2×10^{-4} sec $^{-1}$. Boron nitride powder was employed as a parting agent to prevent bonding of the test bar to the MAR-M246 specimen grips.

Creep-rupture tests were performed in air at 925 and 1000°C. Temperature was controlled to ± 1°C by two Pt/Pt-13Rh thermocouples attached to the specimen. Loads were applied using 10:1 or 20:1 constant load lever arms. Creep strain was measured using linear variable differential transformers in conjunction with extensometers. The knife edges of the extensometers were placed in grooves machined in the shoulders of the tensile specimen, as illustrated in Figure 1. Boron nitride was used as a parting agent, and specimen grips were made of either MAR-M246 or IN-713C. Steady-state creep rate, time to failure, time to the onset of tertiary creep, time to the onset of secondary creep,

percent elongation, and percent reduction in area were measured. Interrupted creep specimens were cooled under load. In a few cases, a test was interrupted by a failure in the MAR-M246 grips. Although these specimens were not cooled under load, they were still considered as interrupted creep specimens suitable for observation of γ' morphology.

Compression testing was performed in air with an Instron machine at constant crosshead speed. Cylindrical specimens 10 mm long and 5 mm diameter were utilized. Pieces of 25 μm thick tungsten foil were inserted between the ends of the specimens and the SiC push bars to prevent welding. Two thermocouples controlled temperatures to within ± $2^{o}C$. In order to maintain specimen alignment, a 5 MPa stress was applied while the specimen was heated to the test temperature. One compression creep test was performed under constant load conditions. The specimen dimensions for this test were 20 mm length and 5 mm diameter.

Metallography

Detection of spurious grains was accomplished by macro-etching. The specimens were immersed in a fresh solution of 10 percent HCl in H_2O_2 (70 percent grade) for approximately 30 seconds. The effectiveness of the etchant varied from batch to batch, and higher HCl concentrations were frequently used. Examination of the surface and ends of each specimen effectively screened out the majority of the polycrystalline samples. The few

polycrystalline specimens which were not detected in this stage were easily distinguished by examination of their fracture surfaces and by their poor mechanical properties.

Samples for optical and scanning electron microscopy (SEM) were prepared by grinding on SiC papers to 600 grit, then polishing on 3 μm diamond and .05 μm Al_2O_3 wheels. The samples were etched between polishing steps. The etchant consisted of a solution of 33 percent HNO_3, 33 percent CH_3COOH, 33 percent H_2O, and 1 percent HF, and was applied by swabbing for approximately 5 seconds.

Transmission electron microscopy (TEM) specimens were prepared by twin jet electropolishing. Three electrolytes were used: a mixture of 10 percent perchloric acid in methanol at $-78^{o}C$, a solution 45 percent butylcelusolve, 45 percent acetic acid, and 10 percent percloric acid at $+ 3^{o}C$, and a solution of 10 percent perchloric acid in acetic acid at room temperature.

Quantitative measurements on micrographs were performed with the aid of a Hewlett Packard 9835A computer and plotter. Locations on a micrograph could be digitized with the use of a digitizing sight which fitted into the pen holder of the plotter. A simple program was written to extract the number of intercepts, the mean and standard deviation of the intercept lengths, and the area fraction of the phases from a line scan across a micrograph. Several scans were made across each photograph, and four photographs were typically used to characterize a given specimen.

Phase Extraction Techniques

Phase extractions were performed according to standard procedures (143). Weight percent of the phases, chemical composition, and lattice parameters of the phases were obtained. A platinum wire was spot welded to the sample, which was immersed in an electrolyte. A platinum mesh was used as a cathode. All extractions were run at room temperature with a current density of 75-85 ma/cm^2.

The γ' particles were extracted from heat treated samples with an electrolyte consisting of 1 w/o $(NH4)_2\ SO_4$ and 1 w/o citric acid in water. This electrolyte separates the γ' and TCP phases from the γ matrix. A sample was cleaned, weighed, and then immersed in the electrolyte for about one hour. After extraction, the solution was filtered through preweighed filters of 0.22 μm pore size. Vigorous scraping of the sample was necessary to remove adherent γ' particles. The sample was dried, weighed, lightly sandblasted, and then reweighed. The weight fraction of γ' was calculated as the weight of residue remaining on the filter, plus the weight of the adherent residue removed by sandblasting, divided by the total weight loss. Arc emmission spectroscopy was used for chemical analysis of the γ and γ' phases. The γ' residues were dissolved in a solution of 70 percent concentrated HF and 30 percent HNO_3 in preparation for the chemical analysis. The electrolyte used in the phase extraction procedure

contained the γ phase already in solution. A mixture of 70 percent HF and 30 percent HNO_3 was added to stabilize the solution prior to the chemical analysis. Lattice parameters were also obtained from the γ' residues by X-ray diffractometer scans.

An electrolyte consisting of 10 v/o HCl and 1 w/o tartaric acid in methanol was used for extraction of TCP phases. A sample was cleaned, weighed, and connected in the electrolytic cell for 3 hours. After extraction, the electrolyte was filtered, and the weight of the residue remaining on the filter divided by the total weight loss of the sample was taken to be the weight percent of TCP phases. The residues were used for chemical analysis and for lattice parameter measurements.

Gamma-Gamma Prime Mismatch Measurements

X-ray diffraction using copper Kα radiation was used to measure the lattice mismatch between the γ and γ' phases. Single crystal disks with faces parallel to (210) planes were polished and used for the X-ray experiments. Diffractometer scans of the (420) fundamental reflections and of the (210) superlattice reflection were used to measure the misfit. The percent misfit was determined from the difference in lattice parameters calculated from the γ and γ' (420) peaks. The sign of the misfit was confirmed by comparison of the (420) peaks with the (210) superlattice peak. The misfit was determined on samples given a full

heat treatment and also on samples which had been given an additional aging treatment of 100 hours at 1000^{o}C.

The mismatch of Alloy B was also determined as a function of temperature. A single crystal disc with a <100> orientation was prepared as for the room temperature measurements. A high temperature camera was used to record the γ and γ' (400) peaks in 50^{o}C increments. The sample was held at each test temperature for 2 minutes before the scan was performed, and then heated to the next temperature. Although the samples were heated in a nitrogen atmosphere, small leaks in the chamber caused oxidation of the samples, limiting the measurements to temperatures below 850^{o}C.

RESULTS AND DISCUSSION

RESULTS

Microstructural Characterization

Chemistry

The results of the chemical analysis are presented in Table II. There are slight differences between the results from the two analysis techniques, and there are also deviations from the aim compositions. In particular, Alloys A, C, D, F, and H exhibited W contents approximately 1 percent below the aim level. (All compositions are in weight percent unless otherwise noted.) Thus, although Alloys A, D, and F were intended as a series with Ta removed from the baseline level, these alloys have an additional reduction of 1 percent W. Similarly, Alloys C and H were intended as a series with 3 percent W substituted for the baseline 3 percent Ta, but actually only 2 percent W was substituted for the 3 percent Ta. Thus, in the remainder of this paper, the following notation will be used to designate the alloys:

Alloys B, E, and G will be designated as the 3Ta-10W series.

Alloys A, D, and F will be designated as the 0Ta-9W series.

Alloys C and H will be designated as the 0Ta-12W series.

As-Cast Microstructure

Optical photomicrographs of samples in the as-cast condition are presented in Figure 2 and illustrate the dendritic structure. The primary dendrite arm spacing varied along the length of a bar from a single casting, reflecting the changes in thermal gradient and growth rate during the solidification process. Typical primary arm spacings were about 200 μm at the bottom of the bar and 550 μm at the top. Because solidification parameters such as mold temperature and withdrawal rate were varied in attempts to improve single crystal yield, the dendrite arm spacings also varied from casting to casting. The percentage of test specimens that were single crystals varied from 25 to 89 percent for the nine castings. Of the bars that were single crystals, approximately 35 percent were within 5^{o} of [001], and an additional 60 percent were between 5 and 10^{o} of [001]. Freckles (141,142) were present in all bars, but they were removed by machining to the gage dimensions.

The interdendritic regions were characterized by coarse γ' structures. In some alloys, large γ' eutectic pools were present, as in Figure 2a. Other alloys did not exhibit eutectic pools but did contain areas of coarse γ', as shown in Figure 2b. Microprobe scans revealed that the interdendritic regions were high in Ti, Ta, Al, and Ni, and low in Cr and W.

Differential Thermal Analysis (DTA) was performed on the as-

cast samples to establish the influence of composition on the transformation temperatures. These results are summarized in Figure 3. It can be seen that Co level did not strongly influence the liquidus or solidus temperatures, but there were some effects caused by the Ta and W contents. The γ' solvus was strongly influenced by both Co and refractory metal concentrations. The solvus increased by as much as $53^{o}C$ as Co level was reduced from 10 to 0 percent, depending on the refractory metal content. Removal of 3 percent Ta and 1 percent W in alloys, A, D, and F caused a drop in solvus of 57^{o}, whereas replacement of Ta with 2 percent W resulted in a decrease of 45^{o}. The difference between the solvus and solidus can be considered as the solution treatment "window," and it can be seen that all alloys had an adequate range for complete solutionizing of the γ' without the danger of incipient melting. These DTA results were confirmed by trial heat treatments in conjunction with optical metallography.

Heat Treated Microstructure

Figure 4 illustrates the fully heat treated microstructure of Alloy B. The coarse as-cast γ' structures were almost completely dissolved by the 4 hour solution treatment. In addition, dendritic segregation was reduced to below the sensitivity of the microprobe. However, some residual segregation was still present, because the dendritic pattern was still revealed by etching. In Alloy B, W-rich precipitates were present after the solution

treatments. These precipitates decorated the dendrite cores, again indicating that some residual segregation remained after the solution treatment.

It also appeared that the solution treatments increased the amount of porosity compared to the as-cast structure. About 0.7 percent porosity was present after heat treatment; the pores were typically spherical in shape and located in interdendritic areas. In contrast, shrinkage porosity was typically irregular in shape. The spherical pores can also be distinguished from incipient melting, as illustrated in Figure 5. This example of incipient melting resulted from a trial heat treatment at 1324^{o}C. In addition, a higher magnification view of a pore, Figure 6, shows no evidence of melting, but instead reveals that the γ' precipitate structure is the same both in and away from the pores.

Also evident in Figure 4 is a fine network of subgrain boundaries. Gamma prime nucleation on these boundaries is illustrated in Figure 7. Alloy B, and to a lesser extent Alloy C, were the only compositions to exhibit subgrains.

The fine distribution of γ' precipitates is illustrated in Figure 8 a-c. The γ' particles ranged from a cubical shape, as in Alloy B, to more rounded shapes, as in Alloys A and G. The γ' size varied slightly from alloy to alloy. The variations in size were probably caused by a combination of the changes in composition and variations in quenching rate and heat treatment. In addition, only slight variations in γ' size existed between the

top and bottom of the bars, and across dendritic and interdendritic areas. The average γ' particle size of fully heat treated Alloy B was 0.25 μm.

The amount of γ' precipitate in each alloy is shown in Figure 9. The weight percent of γ', as measured by phase extraction experiments, was significantly influenced by Ta and W levels, but not the Co levels in the alloys. The weight fraction of γ' was reduced from 68 percent for the 3Ta-10W Alloys B, E, and G, to 63 percent for 0Ta-9W Alloys A, D, and F. Alloys C and H, with 0 percent Ta and 12 percent W, exhibited a γ' weight fraction of 66 percent. Also shown in Figure 9 are the results of quantitative metallography performed on failed rupture specimens. The amounts of γ' measured with this technique are lower in magnitude in comparison with the phase extraction technique, but they do show the same trends as the composition is varied. Again, removal of Ta from the baseline composition caused a decrease in γ' fraction of about 6 volume percent, and replacement of Ta with W caused a reduction of about 3 volume percent. A plot of the amount of γ' measured by the two techniques is shown in Figure 10. The slope of a least-squares line through the data is close to one, which again indicates the correspondence of the two methods. However, the data fell significantly below the line drawn for equal measurements by the two techniques. These discrepancies are discussed in more detail in later sections.

The composition of the γ and γ' phases can be determined using

phase extraction techniques. Analysis of the extracted γ' residues is illustrated in Figure 11. As Co level in the alloy was decreased from 10 to 0 percent, the Co concentration in γ' decreased from 6 to 0 a/o, with a corresponding increase in Ni level from 64 to 73 a/o. The other elements remained almost constant as the Co, W, and Ta contents were varied. The γ' phase consisted of 17 a/o Al, 4.5 a/o W, 3 a/o Cr, 2 a/o Ti, and 0.3 a/o Mo. In the alloys that contained Ta, the γ' phase had 2 a/o Ta and somewhat lower levels of Ni and Cr.

The γ phase compositions are shown in Figure 12. These were obtained by analysis of the electrolyte after extraction. As a check of the analysis procedures, a mass balance using the amounts and compositions of the two phases can be used to calculate the composition of the bulk sample. Comparison of this calculated composition with the actual analyzed composition of the bulk material revealed that both analysis techniques were in good agreement, with the exception of W and Ta levels. Both W and Ta levels analyzed in the phase extraction experiments were typically 1 percent greater than those measured in the analysis of the bulk material. No effort was made to correct these discrepancies because first, the discrepancies are not large, and second, it is unclear which of the analysis steps are incorrect.

In comparison to the γ' composition, the composition of the γ phase was more strongly influenced by alloying variations. As Co level in the alloys was decreased from 10 to 0 percent, the Co

level in γ decreased from 17 to 0 a/o, and the Ni level increased from approximately 54 to 70 a/o. In addition, the Cr level increased slightly as Co was removed. Whereas Al, W and Mo appear to remain constant in all the alloys at 5.0, 2.5, and 0.75 a/o, respectively, the Cr and Ni concentrations varied with the refractory metal content. Removal of the 3 percent Ta and 1 percent W from the baseline caused an increase in Ni by ~ 5 a/o. Substitution of the 3 percent Ta by 2 percent W resulted in an increase in Ni of ~ 4 a/o and a decrease in Cr of ~ 2 a/o.

The partitioning of elements between γ' and γ is represented by the ratio of the concentration of an element in γ' to the concentration in γ. The values for this ratio were essentially independent of the choice of the concentrations in terms of weight or atomic percent. The partitioning ratios are plotted as a function of Co content in Figure 13. Cobalt, Cr, and Mo partition preferentially to the γ phase, with ratios of 0.35, 0.15, and 0.5, respectively. Titanium and Ta partition almost completely to γ', and exhibited partitioning ratios approaching infinity. Although there was some scatter in the ratios for W and Al, no strong trends in the ratio as a function of alloy content were noted, with the average ratios of 1.9 for W and 3.6 for Al. The partitioning ratio of Ni decreased from 1.2 to 1.05 as Co level was decreased from 10 to 0 percent. Table III summarizes the chemical analysis of the phases.

In addition to γ and γ', Alloy B exhibited precipitation of

approximately 0.8 w/o of tungsten-rich particles. These particles were identified as α-W by X-ray diffraction of extracted residues. The composition analyzed from the residues is also listed in Table III. The results of the γ' extractions of Alloy B should be corrected to account for the presence of α-W in the extracted residue. Accordingly, the weight percent of γ' appearing in Figure 9 is the corrected value. The correction for the composition of γ' did not significantly change the results.

The lattice mismatch between the γ and γ' phases was also investigated. The lattice parameters of the extracted γ' phases are plotted versus composition in Figure 14. These results are representative of the unconstrained γ' lattice parameter. Figure 14 illustrates that $a_{\gamma'}$ was not affected by Co level, but was dependent on the Ta and W contents in the alloys. The baseline 3Ta-10W alloys had $a_{\gamma'}$ = 3.5840 A, whereas the 0Ta-9W alloys had $a_{\gamma'}$ = 3.5760 A and the 0Ta-12W alloys had $a_{\gamma'}$ = 3.5785 A.

The constrained lattice parameters of the γ and γ' phase were measured by a diffractometer scan of the [420] peaks from an oriented single crystal. These X-ray peaks are illustrated in Figure 15 and the lattice parameters are listed in Table IV. With the exception of Alloy B, the difference between the constrained and unconstrained lattice parameters was smaller than the experimental scatter. However, the decrease in lattice parameters after aging for 100 hours at 1000^{o}C was significant. This decrease in lattice parameters had some influence on the lattice mismatch δ .

Before aging, only Alloy B exhibited a value of δ large enough to measure. After the 100 hours age, the magnitude of δ for Alloy B increased from about -0.002 to -0.0035, and for Alloy C, the magnitude increased from approximately zero to -0.002.

The good resolution of the Cu $K\alpha_1/K\alpha_2$ doublet in Figure 15 gives an indication that the single crystal was properly oriented, and that factors which cause peak broadening are not excessive. The two most likely causes for peak broadening in these experiments are dendritic segregation and internal stresses, including coherency stresses. Dendritic segregation would influence the peaks of both bulk and extracted samples, so the improvement in resolution of the doublet in the extracted γ' sample, Figure 16, indicates that dendritic segregation is not a major factor in the peak broadening.

The γ and γ' lattice parameters of Alloy B were also measured as a function of temperature, as exhibited in Figure 17. Least-squares fitting of the lattice parameter data to a third degree polynomial was performed with the temperature values in centered form (144). Rearranging the coefficients to express the data in terms of the temperature in degrees centigrade produces Equation [10].

$$a(T) = A + BT + CT^2 + DT^3 \qquad [10]$$

For the γ' phase of Alloy B, A = 3.5827, B = 4.8095×10^{-5}, C =

-6.0862×10^{-9} and $D = 1.1847 \times 10^{-11}$. For the γ phase of Alloy B, $A = 3.59564$, $B = 4.8301 \times 10^{-5}$, $C = -1.1997 \times 10^{-8}$, and $D = 2.65267 \times 10^{-11}$. The lattice mismatch δ is plotted versus temperature in Figure 18. Because oxidation of the specimen limited the measurements to less than 850°C, Equation [10] was used to extrapolate to the temperatures used for mechanical testing, 925 and 1000°C. For Alloy B, with $\delta = -0.0035$ at room temperature, $\delta = -0.0054$ at 925°C and $\delta = -0.0060$ at 1000°C.

The microstructure of Alloy B was also examined with a transmission electron microscope (TEM). The TEM micrograph in Figure 19 confirms the cubic γ' morphology which was also observed in the SEM micrographs presented in Figures 6-8. Figure 19 also illustrates that the γ' particles are fully coherent with the matrix, as evidenced by the absence of misfit dislocations at the γ-γ' interface. Also evident in Figure 19 are δ-fringes parallel to γ-γ' interfaces, which result from the lattice mismatch (145).

Microstructure After Long Aging Treatments

The thermal stability of the alloys was investigated by isothermal aging at elevated temperatures. The effect of aging on the lattice parameters was discussed in the previous section. Other changes in microstructure were also examined, including γ' coarsening, loss of coherency, and precipitation of third phases.

The γ' particles coarsened appreciably during aging at

1000°C. Microstructures of Alloy A after aging for times approaching 1000 hours are presented in Figures 20a-d. The coarsening particles of all alloys followed the typical $t^{1/3}$ time dependence. Measurements of particle size were fit to Equation [6] to determine the rate constant for coarsening. Following Ardell (94-96), for cubic particles the average radius $\bar{r}$ is replaced by $\bar{a}/2$, where $\bar{a}$ is the average length of a cube edge. The rate constant k is plotted versus composition in Figure 21, which illustrates that removal of Co from these alloys approximately doubles the coarsening rate. The coarsening rates for Alloys B and C are also plotted in Figure 21, although these data cannot be directly compared to the other rates. The γ' particles of these two alloys assumed irregular or plate-like morphologies during the aging treatment. This change in shape appears to be related to a loss of coherency, as evidenced by the dislocation networks imaged in Figure 22. The coarsening rates of these two alloys are affected by the choice of the particle dimension to be measured. In addition, the presence of misfit dislocations alters the coarsening rate and thus comparison with alloys that possessed γ' which remained coherent may not be justified.

In spite of the above mentioned problems, the coarsening rate measured for Alloy B at 1000°C is consistent with the coarsening rates measured at 925 and 982°C, as displayed in Figure 23. At the lower temperatues, the γ' particles retained their cubic shape for the exposure times used in this experiment. The slope of this

plot of log k versus 1/T produces the activation energy for coarsening equal to 370 ± 72 Kjoule/mole. The true activation energy for coarsening should be calculated from a plot of log (kT/Ce) versus 1/T. The extra factor T/Ce was not included because Ce is not known for this alloy, although it is not believed to change significantly in the temperature range studied here. Examination of the coarsening data in references (96,98) revealed that the activation energy is not significantly altered by the inclusion of the T/Ce term.

The presence of W-rich precipitates is illustrated in Figures 22 and 24. There were both acicular and blocky particles evident in Alloy B, and in-situ EDAX analysis in the SEM revealed that both types of particles were rich in W. X-ray diffraction of extracted residues showed that these precipitates were mainly α-W with trace amounts of μ phase. Aging Alloy B for 976 hours at 1000°C increased the amount of W-rich phases from 0.8 to 3.7 w/o. Aging Alloy C increased the amount of W-rich phases from zero to 0.5 w/o. Addition of Co to form Alloys D to H or reduction of the Ta plus W total to form Alloy A eliminated the formation of these phases.

Microstructure After Creep-Rupture Testing

After creep-rupture testing at 925 and 1000°C, the γ' particles of these alloys have coarsened from their initial cubic or spherical morphology to lamellae perpendicular to the applied

stress. Scanning electron micrographs of each alloy are presented in Figures 25a-g. These photographs were also used for quantitative metallographic determination fo γ' volume fraction, presented in Figure 9. The lamellar structure is more uniform and more well defined than the distribution of cubic γ' particles, and thus is more amenable to the use of the line intercept technique. In addition, the measurements on creep-rupture tested samples are more representative of the γ' volume fraction at the testing temperature. Most of the γ' that precipitates during cooling from the creep testing temperature would be in the form of fine spherical precipitates, and thus could be easily distinguished from the lamellar γ'. This fine cooling γ' would be included in the amount of γ' measured by the phase extraction technique, which therefore is a measurement of the total γ' content at room temperature. Alloy B, which was creep tested at 925, 960, and 1000^{o}C, provided data for the temperature dependence of the γ' volume fraction in this range. The γ' volume fraction of Alloy B at the various testing temperatures, along with the room temperature phase extraction measurement and the DTA solvus measurement, are plotted versus temperature in Figure 26; similar data for Udimet 700 (98) and Rene'95 (146) are also shown on the figure.

The γ' coarsening behavior during creep was examined in detail for Alloy B. The development of the γ' lamellae was investigated by examination of the microstructures of samples interrupted after various creep exposures. The microstructural changes were studied

at two temperatures, and under two stresses at each temperature. At 1000°C, the applied stresses of 207 and 148 MPa were chosen, and the stresses at 925°C were 310 and 207 MPa. These ranges of stress correspond to a difference of approximately one order of magnitude in strain rate and rupture life at each temperature.

Typical creep curves for specimens tested at 1000°C and stresses of 207 and 148 MPa are presented in Figure 27. Microstructures of samples tested at 207 MPa are shown in Figure 28a-e, and should be compared to the initial microstucture, presented in Figure 8b. Figure 28a illustrates that the γ' particles have changed appreciably after only 5 hours. Changes in the γ matrix are also present, as regions of γ perpendicular to the applied stress are thicker than regions parallel to the applied stress. After 24.55 hours, Figure 28b, the γ' platelet structure is fully developed, and all regions of γ phase parallel to the stress axis have been eliminated. The microstructure in three dimensions now consists of two sets of continuous, interpenetrating lamellae of γ and γ'. This structure remains essentially unchanged during steady state creep, as illustrated in Figure 28c, which shows the microstructure after 46.6 hours. Figure 28d, taken from a sample interrupted after the onset of tertiary creep at 75.5 hours, reveals that some thickening of the γ' plates has occurred. After failure at 110.4 hours, the γ' plates were considerably thicker and more irregular, as shown in Figure 28e. Micrographs of failed specimens such as Figure 28e were located away from the necked

region. In general the structure was somewhat coarser in the necked region near the fracture surface. The average dimensions of the γ' phase, as determined by the line intercept method, are plotted against time in Figure 29. This plot illustrates that the length of the γ' plates increased linearly until a plateau was reached, which corresponded approximately to the point where the γ' became a continuous phase. In contrast, the thickness of the γ' phase remained equal to the initial particle size of 0.25 μm throughout most of the test, until significant thickening of the plates occurred during tertiary creep.

Similar γ' coarsening was observed at 1000°C and 148 MPa. This stress corresponds to a rupture life of approximately 790 hours. Figure 30 illustrates the microstructural changes under these conditions. After 20 hours, the γ' platelet structure was already well developed, as illustrated in Figure 30a. This time was still within the primary creep stage. The microstructure shown in Figure 30b is typical of the steady state structure, and was similar to the structures observed in samples tested at the higher stress shown in Figure 28b and c. As tertiary creep commenced, the γ' platelets exhibited an increase in thickness, as illustrated in Figure 30c, which is from a sample interrupted at 434.5 hours. After failure at 790 hours, the γ' lamellae were considerably thicker and more irregular, as seen in Figure 30d. The plot of γ' plate dimensions, presented in Figure 31, shows the same features as the plot of the higher stress data. Again, the

γ' particles rapidly lengthened during the initial portions of the test, and reached a maximum value after approximately 20 hours. This length was maintained for the remainder of the creep test. The average thickness of the γ' phase remained equal to the initial particle size until the tertiary creep stage, when appreciable thickening was evident.

Although many features of the oriented γ' coarsening at 925°C were similar to those of the coarsening at 1000°C, the kinetics of the coarsening was much slower at the lower temperature. Typical creep curves for samples tested at 925° and 207 and 310 MPa are presented in Figure 32. Microstructural characterization of samples tested at 310 MPa are shown in Figures 33 and 34. Again, the γ' coalesced normal to the applied stress, but at this temperature the γ' platelet structure was not fully developed until after the onset of tertiary creep at 48 hours. This plate formation occurred without appreciable thickening of the plates, but increases in thickness were evident after failure at 129.6 hours, as evident in Figure 33c. The development of the γ' platelet structure at 207 MPa is illustrated in Figures 35 and 36, which again exhibit similar trends. Comparison of samples interrupted after 45 hours under a stress of 207 MPa at 925°C, Figure 35a, and 1000°C, Figure 28c, illustrates the large decrease in coarsening rate at the lower temperature. Comparison of two samples tested at 925°C, but at different stress levels, Figures

33 and 35, demonstrates the decrease in coarsening rate as the applied stress is decreased.

In addition to the interrupted creep tests, other observations also contributed to the description of the directional coarsening process. The γ' lamellae were completely formed and had even thickened in a specimen with a rupture life of only 17 hours, indicating the very fast kinetics of the directional coarsening at 1000^{o}C. The limits of this process are indicated by the absence of coarsening after a tensile test, which lasted approximately 15 minutes. Finally, only a small applied stress was necessary to form the γ'plates, as the plates were present in the threaded sections of failed rupture specimens.

The kinetics of oriented coarsening in the other alloys was also studied. Micrographs of samples tested at 1000^{o}C and 148 MPa are shown in Figure 37a-c. These micrographs demonstrate that the γ' coarsening is a function of composition as well as temperature and stress. The γ' plate formation in Alloy C is similar to that in Alloy B, as illustrated in Figure 37a. However, this coarsening is significantly slower in Alloys E and F, as exhibited in Figures 37b and 37c, respectively.

The γ and γ' lamellar structures can be seen in the previous figures to be very uniform over large areas. However, some discontinuities in the platelet structure can be found in some of the alloys. Alloy B, for example, exhibited a network of subgrain boundaries, as illustrated in Figure 38. Comparison of this

structure, which corresponds to a test interrupted after 5 hours of creep at 1000°C and 207 MPa, with the structure prior to testing, Figure 4, reveals that the subgrain network became finer and more defined during primary creep. These boundaries interrupt the regular γ-γ' lamellar structure, as demonstrated in Figure 39a. The W-rich precipitates in Alloy B also caused discontinuities in the structure, as seen in Figure 39b. Alloy C contained lesser amounts of both subgrain boundaries and W-rich precipitates and thus exhibited a more regular γ' structure than Alloy B. These discontinuities were absent in the other alloys.

The influence of initial γ' particle size was also investigated. A small group of samples were given an oil quench from the solution temperature, rather than the standard forced air quench. In order to preserve the fine γ' size as much as possible, the simulated coating cycle and final aging treatment were not performed, and the stress of 186 MPa was applied at room temperature prior to heating to the testing temperature of 1000°C. The microstructures associated with this treatment are presented in Figure 40. The lamellar thickness in the oil quenched sample interrupted in steady state creep was decreased to 0.18 μm, from the value of 0.25 μm for the conventionally treated samples, as demonstrated by a comparison of Figure 40a and Figures 28b and c. After failure, the γ' lamellae have thickened, Figure 40b, but the plates are finer than the standard microstructures illustrated in Figures 28e and 30d.

The morphological changes of the γ' phase were also influenced by the sign of the applied stress. As demonstrated in the previous figures, the γ' forms plates perpendicular to an applied tensile stress. Under an applied compressive stress, two sets of plates parallel to the applied stress are formed, as shown in Figure 41. The same microstructural features were exhibited by compression samples tested by both the constant crosshead speed and the constant load methods.

Appreciable necking was evident in failed rupture specimens. In several cases, two separate necked regions, of which only one was associated with final fracture, were observed in a single specimen. Although secondary cracks were observed throughout the entire gage section, they were much more numerous in the necked region near the fracture surface. The majority of cracks were associated with micropores, as exhibited in Figure 42b. These cracks did not propagate appreciably until late in the tertiary stage, as demonstrated by Figure 42a, which shows the absence of cracks at pores even after the onset of tertiary creep. This cracking at porosity was also evident in the fracture surfaces, as presented in Figure 43. On the fracture surface, these cracks appeared as rectangular, planar features associated with the pores. No cracks associated with W-rich precipitates or subgrain boundaries were observed in the alloys that contained these features.

Figure 44 is a transverse section from a specimen of Alloy B

creep tested at 1000°C and 148 MPa for 45.8 hours, which is close to the onset of steady state creep. This micrograph illustrates the hexagonal array of misfit dislocations located at the γ-γ' interface. With the operative g-vector of 200, only two of the three sets of dislocations which make up the network are imaged in Figure 44. A longitudinal section of the same specimen is shown in Figure 45. This view clearly shows the γ-γ' lamellar structure. Also evident in Figure 45 are examples of dislocations shearing the γ' phase, whereas dislocations were not observed in the γ phase. The misfit dislocations are also present at the location marked "a" in Figure 45.

Figure 46 is a transverse section from a specimen of Alloy E creep tested at 1000°C and 148 MPa for 60.3 hours. The misfit dislocation spacings were considerably greater in Alloy E, reflecting the lower γ-γ' mismatch of this alloy compared to that of Alloy B, Figure 44. Both Figures 44 and 46 were parts of stereo pairs, which can be used to examine the three dimensional nature of the thin foil observations. The stereo images revealed that the planar dislocation arrays were approximately parallel to the plane of the foil. Consequently, the dislocation spacings could be measured and used to estimate the lattice mismatch of these alloys with the aid of Equation [9]. This method produces $\delta = 0.008$ for Alloys B and $\delta = 0.003$ for Alloy E, in reasonable agreement with the values of δ extrapolated to 1000°C.

Mechanical Properties

Tensile Proprties

Tensile tests at 1000°C and a strain rate of 2.2×10^{-4} sec^{-1} were performed on all alloys. Typical stress-strain curves are presented in Figure 47. Although both true and engineering stress-strain curves are illustrated, the true stress curve is not valid after the onset of necking. Although necking was always observed, the strain at the onset of necking could not be determined. The shape of the stress-strain curves presented in Figure 47 indicate a possible yield point and work softening behavior, althouqh this shape could also be explained by a early onset of necking.

The 0.2 percent offset yield stress is plotted versus Co content in Figure 48. In the baseline 3Ta-10W alloys, reduction in Co level from 10 to 0 percent increased the yield stress from 448 MPa to 615 MPa. Removal of 3 percent Ta and 1 percent W reduced the yield stress to 377 MPa, independent of Co content. Substitution of 2 percent W for the Ta resulted in a yield stress of 500 MPa for both Co levels. The ultimate tensile strenqths of the crystals exhibited similar results, as evident in Figure 49. For the 3Ta-10W series of alloys, the ultimate tensile stress increased from 508 to 650 MPa as Co level decreased from 10 to 0 percent, whereas the 0Ta-9W alloys possessed an ultimate strength of 430 MPa which was independent of Co content. The 0Ta-12W

alloys had ultimate strengths of 507 and 586 MPa for the 10 percent Co and 0 percent Co concentrations, respectively.

The tensile ductilities of the alloys are shown in Figure 51. Both percentage reduction in area and percentage elongation were higher for the lower strength alloys. For example, the 0Ta-9W alloys possessed the lowest yield and tensile strengths, but had the highest tensile ductilities, approximately 30 percent elongation. The lowest elongation value of about 20 percent was measured for the highest strength Alloy B.

Creep-Rupture Properties

Extensive creep-rupture testing was performed at 1000°C over a range of stresses. At least four stress levels were used for testing of each alloy. Typically, these stress levels provided a range of about 1.5 orders of magnitude in strain rates and rupture lives, although some alloys were tested over a range of 3 orders of magnitude. In addition, a limited amount of testing was performed at 925 and 960°C.

Typical creep curves for Alloy B at 1000°C are illustrated in Figure 27. The creep curves for the other alloys were similar except for the primary creep stage. Alloy B exhibited a "normal" primary creep stage whereby the creep rate gradually decreased to the steady state value. All the other alloys exhibited an incubation period of very low creep rate before a sigmoidal-shaped primary stage, as exemplified in Figure 51. The duration of the

incubation period was typically 2 hours. No trends in the duration of the incubation period as a function of applied stress or alloy composition were noted. The second stage creep regions of all alloys were characterized by a constant creep rate over an extended period, followed by a gradual increase in creep rate as the tertiary creep stage was entered.

The steady state creep rates under various applied stresses are plotted versus Co level in Figures 52-54. For the 3Ta-10W alloys, the steady state creep rate was reduced by approximately a factor of 5 as Co content was reduced from 10 to 0 percent. This trend was consistent for all stress levels. For the 0Ta-12W alloys, similar trends were observed whereby reduction of Co level from 10 to 0 percent caused a reduction in creep rate by about a factor of 5 at high stresses and a factor of 8 at low stresses. The influence of Co in the creep rates of the 0Ta-9W alloys was not very strong. The 10 percent Co Alloy F exhibited consistently higher creep rates, and the 5 percent Co Alloy D consistently had the lowest creep rates, but these differences were all within a factor of two.

The rupture lives of the alloys followed trends opposite to the trends in creep rates, i. e., alloys with high steady state creep rates had short rupture lives. For the baseline refractory metal alloys, removal of Co caused increases in life by about a factor of 1.8 at 148 MPa and about 1.5 at 207 MPa, as shown in Figure 55. Removal of Co from the 0Ta-12W alloys resulted in in-

creases in life by a factor of 2.4 at 148 MPa and a factor of 2 at 207 MPa, as indicated in Figure 56. The influence of Co was much smaller for the 0Ta-9W alloys. For example, in Figure 57, it is evident that at 148 MPa, the 5 percent Co Alloy D had lives 1.2 times greater than the lives of the 10 percent Co Alloy F and 1.04 times greater than the lives of the 0 percent Co Alloy A.

A summary plot presenting the rupture lives of all alloys at 148 MPa is shown in Figure 58. Note that the lives are plotted on a linear scale in this figure, rather than the log scale in Figures 55-57. The baseline alloys exhibited lives which increased from 435 to 790 hours as Co content decreased from 10 to 0 percent. Substitution of 2 percent W for 3 percent Ta increased the rupture life at both Co levels, although the effect was stronger at 0 percent Co. The rupture life increased from 790 to 1322 hours when the W substitution was performed on the 0 percent Co alloy, and life was increased from 435 to 544 hours for the 10 percent Co alloy. Also evident in Figure 58 is that the 0Ta-9W alloys were by far the weakest in creep resistance at all Co levels.

The trends shown in this plot do not completely describe the composition dependence of the creep strength. Although the 0Ta-9W alloys always possessed shorter lives and higher creep rates than the other alloys, independent of stress level, the relative ranking of the other alloys was a function of the applied stress. For example, although both Alloys B and C had rupture lives of 110

hours at 207 MPa, Alloy C lasted 500 hours longer than Alloy B at 148 MPa, and this difference was increased further as the stress was decreased.

The creep ductilities of the alloys followed trends similar to the trends in the tensile ductilities. Typically, alloys with high creep resistance exhibited lower creep ductility. No trends in ductility as a function of stress level were apparent. Thus, the average value of the percentage elongations of all tests for a single alloy were plotted versus Co concentration in Figure 59. Alloy C, with the highest creep resistance, had the lowest ductility of approximately 13 percent elongation. The OTa-9W alloys exhibited the lowest creep strength and the highest creep ductilities, possessing elongation values near 35 percent.

The data of all alloys were plotted as a function of applied stress. The following equations were fitted by standard regression techniques, where A_1-A_5 are constants and k, l, m, n, and p are the stress exponents:

$$\dot{\varepsilon}_s = A_1 \sigma_a^n \qquad [11]$$

$$t_f = A_2 \sigma_a^{-p} \qquad [12]$$

$$t_t = A_3 \sigma_a^{-l} \qquad [13]$$

$$t_s = A_4 \sigma_a^{-k} \qquad [14]$$

$$\dot{\varepsilon}_s = A_5 t_f^{-m} \qquad [15]$$

Equation [11], which relates the steady state creep rate to the applied stress, is a simplification of Equation [1] often utilized

when data from only one temperature is evaluated. Equations [12], [13], and [14] relate the time to failure, the time to the onset of tertiary creep, and the time to the onset of secondary creep to the applied stress. Equation [15], often referred to as the Monkman-Grant relationship (147), relates the steady state creep rate to the rupture life. Algebraic manipulations can show that m = n/p.

Double logarithmic plots of $\dot{\varepsilon}_s$, t_f, and t_t versus applied stress are presented in Figures 60-75. The data consistently exhibit linear behavior, which supports the use of the power law relations in Equations [11]-[15]. Close examination of Figures 60-75 reveals several features. The slopes of these plots, which are equal to the stress exponents in Equations [11]-[13], exhibit several trends. The creep rate exponent n is consistently greater than the rupture life exponent p. The exponent l, which relates the onset of tertiary creep to the applied stress, consistently falls between n and p. In addition, the values of n and p are relatively constant as a function of alloy composition, as further demonstrated by plots of n and p versus Co content, Figures 76 and 77. Values of n, p, l, and m are also presented in Table V.

Although the scatter in the primary creep times was higher than the scatter in the other measurements, the trends as a function of applied stress is clearly shown in Figure 78. The variations in the slope of these alloys as alloy content varied were

not statistically significant, thus resulting in an average slope of approximately 4. One general trend evident in Figure 78 is that the OTa-9W alloys exhibited lower times to the onset of secondary creep, in accordance with their lower rupture lives. The strain at the onset of secondary creed was independent of stress, but varied with alloying. Alloys B and C exhibited values of 0.006, and all other alloys possessed values of 0.003 for the strain at the onset of secondary creep

Figures 79 and 80 are summary plots of the steady state creep rate and rupture life data of all alloys as a function of applied stress. Figure 79, which presents the steady state creep rate data, illustrates that the stress exponent is approximately the same for most of the alloys, with the exception of the OTa-12W Alloys C and H, with slightly higher slopes. Also evident in Figure 79 is the low creep strength of the OTa-9W Alloys A, D, and F, which exhibit creep rates at a given stress more than an order of magnitude higher than the stronger alloys. The rupture life data of Figure 80 presents similar conclusions. The stress exponents of Alloys C and H appear to be higher than the exponents of the other alloys, and the OTa-9W series are the least creep resistant alloys. Both Figures 79 and 80 reveal that Alloys B and C are the most creep resistant alloys over a wide range in applied stress. Because of the higher stress exponents of Alloy C, its advantage over Alloy B is increased as the applied stress is decreased. At a stress of 207 MPa, the lives and creep rates of the

two alloys are comparable, but at a stress of 125 MPa, the creep rate of Alloy C is lower than that of Alloy B by a factor of 5, and its rupture life is greater by a factor of 3.

The similar trends between creep rate and composition and between rupture life and composition imply a close correlation between creep rate and rupture life. This correlation is supported by the excellent fit of the data by the Monkman-Grant relationship, Equation [15]. The values of the exponent m, presented in Table V, were approximately constant for all alloys. The values of m were close to but significantly greater than one, a value frequently observed in other materials.

There were also correlations between the time to failure, t_f, and the time to the onset of tertiary creep, t_t. The ratio of these two quantities, t_f/t_t, varied linearly with the applied stress, as illustrated for Alloy B in Figure 81. Although no deviations from linearity were observed, the curves in Figure 81 were drawn such that they approached the asymptotic value of one. This is due to the definition of t_f and t_t.

The plots of the t_f/t_t ratio versus stress for the other alloys are displayed in Figure 82. Figure 82 illustrates that all the alloys behave in similar fashion, exhibiting similar magnitudes of the ratio, and similar dependence on the applied stress. A general trend, but with some exceptions, evident in Figure 82, is that the more creep resistant alloys had lower values of the ratio. In other words, the more creep resistant alloys spent a

greater portion of their rupture lives in the secondary creep stage. The strain at the onset of tertiary creep was approximately constant for all alloys at all stresses, with an average value of 0.015.

Alloy B was the most extensively studied alloy, as illustrated in Figures 61 and 69. One feature indicated by these data is that the casting to casting variability is negligible compared to the scatter among bars of the same casting. Also plotted in Figure 61 are two data points for samples tested in compression. The primary purpose of the compressive tests was the observation of the morphological changes of the γ' phase under a compressive stress. The compressive data exhibit reasonable agreement with the tensile data, even though the compressive tests were performed at constant crosshead speed and with a different specimen geometry, in contrast to the constant load tensile creep tests.

In addition, the creep behavior of Alloy B was studied at 925^{o}C, with the creep-rupture data at this temperature presented in Figures 83 and 84. At this temperature, Alloy B exhibited a yield stress of 840 MPa and an ultimate tensile stress of 875 MPa. The typical creep curves at 925^{o}C are displayed in Figure 32. Alloy B, which exhibited a normal primary creep curve at 1000^{o}C, exhibited a sigmoidal primary creep stage at 925^{o}C. In addition, the second creep stage, which was characterized by a constant creep rate over an extended time period at 1000^{o}C, was not as well defined at 925^{o}C. At 925^{o}C, the constant strain rate

region of the creep curve was a much smaller portion of the total rupture life, as illustrated by the creep curves in Figure 32 and the higher t_f/t_t ratio for the 925°C data in Figure 81.

Figure 85 displays the rupture lives of several alloys at 925°C and 207 MPa. The influence of composition on the rupture lives of these alloys at 925°C is very weak, as all the alloys with high Ta plus W totals exhibited lives within 20 percent of each other. The slight trend of decreasing life as Co content is reduced was the reverse of the trend exhibited by these alloys at 1000°C, but more extensive testing at 925°C would be required to satisfactorily characterize the behavior at this temperature.

When creep data at more than one temperature is available, the apparent activation energy for creep can be evaluated. Figure 86 illustrates the plots of log ($\dot{\varepsilon}_s$) and log ($1/t_f$) versus 1/T, which, according to Equation [1], allows Q to be determined from the slopes of these lines. These data indicate that the activation energy determined with the creep rate data is essentially equal to that determined with the rupture life data. The activation energies of 412 ± 126 and 381 ± 50 Kjoule/mole. were measured with the $\dot{\varepsilon}_s$ and t_f data, respectively. Figure 86 also shows that the measurement of Q was unaffected by the use of separate specimens at each temperature, or by cycling the temperature on a single specimen. One drawback to the above method for the determination of Q is the large confidence intervals around Q, caused by the relatively few data points used.

By performing multiple regression on all data taken at all stresses and temperatures, a Q value with tighter confidence limits may be calculated. This method can only be used if Q is independent of stress, or equivalently, if n and p are not a function of temperature. From Table V, it can be seen that the n and p values for Alloy B at 1000 and 925°C are slightly different, but the differences are not statistically significant. Therefore multiple regression was performed to fit all data of Alloy B to Equation [1]. The Q values determined by this method are essentially the same as those determined by the simple plot of Figure 86, producing values of Q = 415 ± 74 and 412 ± 30 Kjoule/mole for the $\dot{\varepsilon}_s$ and t_f data, respectively.

The activation energies were also determined with the corrections for the temperature dependence of the elastic modulus. The dynamic elastic modulus <001> oriented crystals of Alloy B decreased approximately linearly from 87.12 to 82.00 GPa as the temperature increased from 925 to 1000°C (148). Using the modulus correction in Equation [2], the activation energies of 336 ± 69 Kjoule/mole for the $\dot{\varepsilon}_s$ data and 353 ± 28 Kjoule/mole for the t_f data were determined. With the modulus correction employed in Equation [3], the activation energies of 356 ± 69 and 332 ± 28 Kjoule/mole were determined with the $\dot{\varepsilon}_s$ and t_f data, respectively. Thus, it can be seen that the choice of modulus correction did not significantly influence the value of the activation energies determined with both creep rate and rupture life. The

corrected Q values of Alloy B are in reasonable agreement with the activation energy for Ostwald ripening of γ' in Alloy B, measured at 370 ± 72 Kjoule/mole.

Finally, a few creep rupture tests were performed in order to provide information on the influence of initial microstructure on the creep properties. To obtain a fine γ' particle size, some samples of Alloy B were oil quenched from the solution treatment temperature. A specimen with this microstructure exhibited a rupture life of 235.7 hours at 1000°C and 186 MPa, compared to an average life of 212.7 hours for samples given the standard heat treatment. This variation in life was within experimental scatter. Thus, refinement of the initial γ' size did not significantly improve the rupture life of Alloy B at 1000°C. Another test was performed to examine the influence of a fully developed γ' lamellar structure present prior to testing at 925°C. The microstructural observations of samples tested at 925°C, Figures 33 and 35, revealed that oriented γ' coarsening was significantly slower than the coarsening at 1000°C. Therefore, a sample was pre-crept at 1000°C and 207 MPa for 20 hours to form the γ' platelets, followed by creep testing at 925°C and 276 MPa. The pre-crept sample lasted 202 hours under these conditions, which was slightly less than the rupture life of 266.5 hours for samples given the standard heat treatment.

DISCUSSION

Microstructure

The primary microstructural feature in all of the single crystal alloys is the copious precipitation of the γ' phase. The influence of composition on the solvus, particle size, particle shape, volume fraction, lattice parameter, and coarsening rates of the γ' phase will be emphasized in the discussion below.

The influence of Co, Ta, and W contents on the transformation temperatures of these alloys is important for the determination of proper solution treatment temperatures. Optimum mechanical properties are obtained when the coarse γ' present in as-cast microstructures is completely dissolved and re-precipitated as a fine dispersion. The large difference between the solidus and the γ' solvus enabled all alloys to be properly solution treated. The increase in γ' solvus as Co content was decreased from 10 to 0 percent is consistent with previous results (63,133). The decrease in solvus which resulted from the removal of Ta was expected because Ta partitions strongly to the γ' phase. Substitution of W for Ta produced an intermediate reduction of the solvus, consistent with the tendency of W to partition less strongly to γ'. The solvus temperatures of the alloys were also correlated with the volume fraction of γ'. High levels of elements which partition strongly to γ' promote higher volume fractions of γ' and increase the stability of γ', which results in increased γ' solvus

temperatures. Tantalum is a strong γ' former and therefore the 3Ta-10W alloys exhibited the highest solvus temperatures and the highest percentage of γ'. Tungsten partitions less strongly to γ', and the 0Ta-12W alloys had lower γ' solvus temperatures and γ' fractions. The 0Ta-9W alloys, with the lowest Ta plus W totals, also had the lowest solvus temperatures and γ' fractions. However, there were some exceptions to the general correlation between solvus and γ' fraction, as illustrated by the influence of Co level, which had a strong effect on the γ' solvus but did not significantly affect the percentage of γ'.

The weak influence of Co on the γ' volume fraction is similar to previous work in other alloys (135,136), where only small decreases in γ' fraction as Co content was decreased were observed. The work on polycrystalline MAR-M247 (133) appears to be the only study to report significant changes in γ' fraction as a function of Co level. Although there are no apparent reasons for this effect, the lack of confirmation of the results gives reason to doubt the phase extraction data in (133).

As presented in Figures 9 and 10, the two methods used for measurement of γ' fraction produced similar trends, but were significantly different in magnitude. The weight fraction measurements obtained from phase extraction should be converted to volume fraction for direct comparison to the quantitative metallographic results. This correction does not change the phase extraction results significantly, based on the calculated densities of the γ

and γ' phases. The density calculations were based on published regression equations (149). The equality of the densities is also in agreement with other workers (98). These results imply that the observed differences between the γ' fraction determined by the two methods cannot be rationalized by differences in the densities of the γ and γ'. As discussed previously, the γ' fraction measured by quantitative metallography on failed creep-rupture specimens is more representative of the γ' fraction at the testing temperature, whereas the phase extraction results should be representative of the γ' fraction at room temperature. Accordingly, the phase extraction results and the quantitative metallographic results for Alloy B were plotted versus temperature in Figure 26. The temperature dependence of the γ' fraction is reasonable in comparison to previous work (98,146). Consequently, it is concluded that the observed differences in γ' fraction measured by the two methods is the result of the difference in γ' fraction at room temperature and at the creep testing temperature.

In the fully heat treated condition, the γ' particles are present as a fine distribution of discrete particles. Although the size of the particles did not vary significantly as composition was varied, the shape of the particles was a function of the alloy content. Some of the alloys, such as Alloys A, D, F, and G, possessed spherical particles, typical for alloys with low γ-γ' mismatch and small particle sizes (150). Other alloys, such as Alloys B, C, and H, exhibited cuboidal γ' morphologies, consistent

with higher mismatch values. The γ' in the alloys with spherical particles underwent a transition to a cuboidal morphology upon aging, as seen for Alloy A in a comparison of Figures 8a and 20a. This commonly observed effect (96,104) has been explained as a consequence of the minimum in surface energy on [100] interfaces in γ-γ' systems. At sufficiently large particle sizes, this effect more than compensates for the increase in surface area in changing from spherical to cuboidal particles.

Another notable result is the increased amount of porosity which is observed after the solution treatment. This porosity did not appear to be caused by solidification shrinkage, because of the spherical morphology and also because it was not observed in the as-cast condition. The possibility of the pores being associated with incipient melting was also considered, but did not seem likely because of the absence of any evidence of melting near the pores.

One plausible explanation is that the pores form as a result of a Kirkendall effect (151). This effect could arise from the segregation of W in the as-cast microstructure. The dendritic cores are enriched in W and depleted of Ni, and the homogenization that occurs during the solution treatment would cause W to diffuse to interdendritic regions, whereas Ni would diffuse in the opposite direction. Because W diffuses much more slowly than Ni (85), it is conceivable that Kirkendal porosity would result in the interdendritic porosity observed in this study.

The chemical analysis of the γ and γ' phases produced some interesting results. As expected, the concentration of Co decreased and that of Ni increased in the γ' phase as Ni was substituted for Co in the bulk alloys. Similarly, the Ta containing alloys exhibited high Ta concentrations in γ'. Apart from these changes, any trends in the concentrations of the other elements in γ' were smaller than the experimental scatter. These data do indicate that the γ' phase contains significant amounts of W, Ti, and Ta in solid solution. These concentrations were not unexpected, as Ti and Ta are known to be strong γ' formers, and high W levels in the γ' of similar alloys such as MAR-M200 (4,31), MAR-M247 (133), and some experimental alloys (152).

The composition of the γ phase varied slightly as a function of the bulk alloy composition. In addition to the expected changes in Co and Ni contents as the total Co level was varied, the Cr, W, and Ni concentrations varied slightly with both Co and refractory metal levels in the bulk alloy. Again, these changes were within the ranges reported for other superalloys (4,152). The above changes in γ and γ' compositions are reflected in the partitioning ratios of the individual elements. In agreement with previous work (4,152), Cr, Co, and Mo partition preferentially to the γ phase, whereas Al, W, Ti, and Ta partition to γ'. The partitioning of elements was not significantly influenced by the various alloying modifications.

It is apparent that both the γ matrix and the γ' precipitate

are highly alloyed. The γ phase has significant amounts of Cr, Co, Al, W, and Mo, and γ' contains W, Ti, Ta, Co, Cr, and Mo. In fact, the concentrations of elements in the γ and γ' have approached and even reached the solid solubility limit, as evidenced by the small amounts of W-rich precipitates in Alloys B and C. These elements, especially the refractory metals W and Ta, are expected to have significant contributions to solid solution strengthening mechanisms. In addition, as the solid solubility limits for these elements are approached, the influence of short range order may contribute to the strength of these alloys (7,8,153).

As mentioned above, precipitation of the W-rich phases α and μ were observed in Alloys B and C. The amount of these phases is dependent on the total Ta plus W level, and the Co level in the alloy. Alloy B, with 13 percent of Ta plus W, exhibited the largest amounts of W rich precipitates. Alloy C, with 12 percent of Ta plus W, precipitated only a small amount. Finally, Alloy A, with only 9 percent of Ta plus W, did not exhibit any third phase precipitation. The addition of 5 percent Co to Alloy B, which formed Alloy E, also eliminated the α and μ precipitation. This is in agreement with previous results that have shown increases in the solubility for W in the γ-γ' matrix as Co was increased (63,133). Although the influence of Co on the solubility of W is clearly shown in this investigation by the absence of W-rich phases in Alloy E, the increased W concentrations were not ob-

served in the chemical analysis of the γ and γ' phases. Evidently, the magnitude of the expected changes were below the sensitivity limits of the chemical analysis procedures. Aging Alloys B and C at 1000°C resulted in further precipitation of these W-rich phases. The slow precipitation kinetics of these phases are similar to the kinetics of other phases such as sigma (3), and are probably caused by the slow diffusion rates of the refractory elements which form these phases.

The lattice parameter measurements also provided important information. The γ' lattice parameters were independent of Co content, which is consistent with the analyzed composition of γ'. As Co content was increased, only the Co and Ni concentrations in γ' changed. Since Co and Ni have only very small differences in atomic size, the lattice parameter of γ' would not be expected to vary significantly (154). The alloys with high W or Ta levels exhibited higher lattice parameters, as expected from the large atomic radii of these elements. The difference between the constrained and unconstrained γ' lattice parameters was negligible for all alloys except Alloy B. Alloy B, with the highest lattice misfit, would be expected to exhibit the largest constraint on the lattice parameter, which in turn would result in the largest difference between the extracted and *in situ* measurements. The decrease in lattice parameters which resulted from the 100 hour age at 1000°C indicates that the composition of γ and γ' were changing during the aging treatment. Some of these changes in

composition could have resulted from a reduction of residual dendritic segregation, although this effect would be very small at such a low temperature. Another possible source for the changing composition is that the compositions are gradually approaching their equilibrium value. As shown by the Gibbs-Thomson equation, the equilibrium values of the concentrations of the γ and γ' are reached only after the γ' particles have grown infinitely large (96,103,151).

The lattice misfit between the γ and γ' phases is expected to have significant influences on the properties of these alloys. As displayed in Table IV, only the alloys with 0 percent Co and high Ta plus W levels had misfit values large enough to be measured by X-ray diffraction. The addition of 5 percent Co was sufficient to decrease the misfit to below the detection limit. Because the γ' lattice parameter was independent of Co content, the effects of Co on mismatch were accomplished by changes in the γ lattice parameter. A decrease in the magnitude of the lattice mismatch as Co level increased was also noted in other work (104), although these alloys possessed positive misfit values. Although Co is not expected to alter the lattice parameter of Ni very significantly (154), its effects on the concentration of other elements in the γ phase can account for the changes in lattice parameter of γ. The 100 hour age at 1000^{o}C also increased the magnitude of the lattice mismatch for Alloys B and C. This effect can be explained by the loss of coherency exhibited in these alloys. The presence of

misfit dislocations would consume the elastic coherency strains, thereby relieving the constraint on the lattice parameters, and thus increasing the measured mismatch.

The γ and γ' lattice parameters of Alloy B were also measured as a function of temperature. Because thermal vibrations would cause peak broadening and therefore decrease the resolution of the mismatch measurement technique, no attempts were made to measure the elevated temperature lattice parameters of the other alloys with smaller mismatch. The thermal expansion of the lattice parameters is similar to previously published results (20,155). Since there is no generally accepted relation for the description of thermal expansion data (155), a third degree polynomial was chosen. The polynomial expressions were sufficiently accurate to provide reasonable extrapolations to 1000^{o}C. The misfit values of Alloy B also exhibit a temperature dependence similar to that in published data (20). Thus, it is demonstrated that two important microstructural features, γ' volume fraction and γ-γ' lattice mismatch, can change considerably from room temperature to the mechanical testing temperatures. The results of the present study are in agreement with those of other workers who have stressed the importance of this point (20,128).

With the assumption that the misfit of the other alloys follows a similar temperature dependence to Alloy B, it is predicted that the Alloys A, D, E, F, G, and H, with unmeasurable misfit at room temperature, would possess $\delta \sim -0.003$ at 1000^{o}C. Alloy C,

with a $\delta = -0.0002$ at room temperature, would exhibit $\delta \sim -0.005$ at 1000°C. The extrapolated misfit values for Alloys B and E were in very good agreement with the values measured from the dislocation spacings in Figures 44 and 46. This would support the contention that the hexagonal dislocation network observed in a thin foil at room temperature is representative of the actual exposure temperature.

Exposure at 1000°C for extended periods of time resulted in changes in γ and γ' chemistries, γ' coarsening, precipitation of W-rich phases, and loss of coherency. For the alloys with γ' particles that remained coherent, reduction in Co level increased the γ' coarsening rate. This effect is consistent with previous findings (104). The reasons for this effect are unclear, as it appears that Co additions influence several features that may decrease γ' coarsening rates, including effects on diffusion and mismatch. One unexpected result was the lack of any effect of refractory metal levels on γ' coarsening rates. It was expected that alloys with higher levels of the slower diffusing Ta and W would have lower γ' coarsening rates, but evidently the magnitude of the compositional changes was not sufficient to cause the expected reductions in coarsening rates.

As discussed previously, the 0 percent Co Alloys B and C were exceptions to the above trends and exhibited anomalously low coarsening rates. These low rates appear to be the result of the loss of coherency which occurred in these two alloys. Because of

their high lattice mismatches, Alloys B and C exhibited a loss in coherency at smaller particle sizes and shorter times than the other alloys. Although Rastogi and Ardell (110) reported increased coarsening rates when coherency was lost, other data appears to support the opposite conclusion, whereby a stabilization against particle growth at long aging times was reported (112,113). This stabilization was associated with the loss of coherency in a Cu-Co alloy (113). Although no conclusive reasons for the stabilization were given by Footner and Richards (112), they did observe an irregular γ' morphology associated with this phenomenon. A change from a cuboidal to irregular γ' morphology as an indication of loss of coherency is consistent with this investigation and the observations in (106). Thus, it is reasonable to associate the stabilization of γ' size observed by Footner and Richards with a loss of coherency, in agreement with the interpretation of Porter et al. (156). It also follows that the low γ' coarsening rates observed in this study can also be attributed to the loss of coherency. It is clear that the transition from a coherent to a semi-coherent interface is associated with a reduction in the total interfacial energy, because such a transition can only occur if it is energetically favorable. This reduction in surface energy may be sufficient to decrease the driving force for coarsening, which would result in lower γ' coarsening rates. Also, the stable dislocation network may decrease the mobility of the γ-γ' interface, which would further decrease the coarsening

rate (157). The observation that higher γ-γ' mismatch values exhibit lower γ' coarsening rates is contrary to the ideas of some workers (5,48), but in agreement with the results of others (24, 87, 99, 100). However, it is recognized that except as noted above, the loss of coherency was not observed in these other studies.

The activation energy for Ostwald ripening for Alloy B was determined to be approximately 370 Kjoule/mole. This value is higher than the values typically found for coarsening in binary nickel alloys (95, 96, 110) and the superalloys Udimet 700 (98) and IN 738 (114), which exhibited values near 270 Kjoule/mole. A value of 270 kjoule/mole is in close agreement with the activation energy for diffusion, as predicted by the LSW theory. Although 370 Kjoule/mole appears high compared to previous work, the increase can be explained at least partially by the high W levels in Alloy B. The activation energies for diffusion in binary Ni-W alloys have been measured in the range of 300 to 335 Kjoule/mole (85), which approach the value for γ' coarsening in Alloy B. In addition, higher activation energies, as high as 365 Kjoule/mole, have been measured for alloys with increased compositional complexity (85). Based on the above data, it is not unreasonable to conclude that the γ' coarsening in Alloy B is diffusion controlled.

All alloys exhibited pronounced directional γ' coarsening during creep-rupture testing at 1000^{o}C. The directional coarsening observed in this study will be compared to theoretical pre-

dictions and similar observations of γ' morphology in other alloys. The derivations of Pineau (124), based on isotropic elasticity, appear to be generally accepted as the most satisfactory treatment of this problem (121, 128). This theory predicts that a given particle morphology is dependent on the sign of the lattice mismatch and the sign of the applied stress, among other factors. Accordingly, an alloy with positive misma' ' is predicted to exhibit plate-shaped particles perpendicular to an applied tensile stress and rod-shaped particles parallel to an applied compressive stress.

In this investigation, the γ' of Alloy B formed plates perpendicular to a tensile stress, and two sets of plates parallel to a compressive stress. The shift in orientation of the plates as the sign of the applied stress was changed is in agreement with Pineau's treatment. In addition, the observations that all the alloys formed the platelet structure normal to an applied tensile stress supports the conclusion that all the alloys had the same sign of misfit at the testing temperature. However, the observation of γ' plates normal to the tensile stress would be consistent with Pineau's predictions for an alloy with positive lattice mismatch, rather than the negative mismatch measured for the present alloys.

It is useful to compare the observations on Alloy B with the morphological changes of other alloys with negative mismatch. The γ' shape changes observed in this study are in agreement with the

observations of Pearson (128) and MacKay (158), but in conflict with those of Carry and Strudel (117, 122).The response of Alloy B under a compressive stress is similar to the response of the alloy studied by Carry and Strudel under tension. Thus, the predictions of Pineau are consistent only with the alloy of Carry and Strudel, although Alloy B and the alloys of MacKay and Pearson also have negative mismatch. In addition, of the studies on alloys with positive lattice mismatch, two studies (120, 121) have observed results in accordance with Pineau's predictions, and one study (123) was in disagreement. One source for these discrepancies is the possibilities of errors in the measurement of mismatch, including the possible changes in mismatch as temperature is increased from room temperature to the testing temperature.

However, Pineau's treatment considered only the three particle morphologies of spheres, plates perpendicular to the applied stress, and rods parallel to the applied stress. Extension of the treatment to include plates parallel to the applied stress, as observed in the present study and by Carry and Strudel, is one modification that should be considered. It also appears necessary to incorporate the effects of elastic anisotropy and elastic interactions between particles, as suggested by Pineau (124). Finally, the influence of alloying on the elastic constants of γ and γ' may also have to be considered.

The directional γ' coarsening rate under a given applied stress and temperature was a function of the lattice mismatch.

Alloys B and C, with the largest magnitude of mismatch, exhibited the most rapid γ' plate formation, whereas Alloys E and F, with smaller misfit values, exhibited significantly slower coarsening. This can be explained by the concept that an increase in the magnitude of the mismatch causes an increased driving force and thus more rapid coarsening.

The γ' coarsening in Alloy B during creep was remarkably similar to the observations of Pearson et al. (128) and MacKay (158). This was not entirely expected, because the room temperature misfit was less than half of the misfit in the alloy studied by these workers (128, 158). However, as temperature increased, the misfit of Alloy B increased in magnitude to values closer to the values of Pearson's alloy. In addition, recent high temperature X-ray diffraction experiments have shown that the misfit in Pearson's alloy does not change as significantly as the misfit in Alloy B (158). These results reveal that although the mismatch values of the two alloys are significantly different at room temperature, the differences in thermal expansion cause the mismatches of the two alloys to be nearly equal at the creep testing temperature. This is further evidence that the two alloys show similar γ' coarsening as a result of their similar mismatch values at the testing temperature. Alloy B can be considered a more conventional superalloy than the alloy studied by Pearson and MacKay, especially in the sense that Alloy B contains appreciable amounts of Cr. Consequently, it appears that the occurrence of rapid

changes in γ' morphology under creep conditions, first reported by Pearson (127), is more general than previously thought.

The rapid γ' coarsening of Alloy B was studied as a function of the applied stress, temperature, and exposure time. A summary of the primary results will be presented, followed by a discussion of these results. At 1000°C, the initially cuboidal γ' particles rapidly coalesced to form the lamellar structure in the absence of any lamellar thickening. At this temperature, the fully developed structure was formed after approximately 20 hours at both high and low stresses. This time corresponded to the onset of secondary creep at 207 MPa, but was in the middle of the primary stage at 148 MPa. The lamellar structure remained constant throughout most of the secondary creep stage, followed by a gradual thickening of the platelets during teritary creep. At 925°C, the γ' coarsening kinetics were significantly reduced such that the more rapid coarsening at the higher stress was clearly observed. At this temperature, the fully developed lamellar structure did not form until the secondary creep stage at 207 MPa and after the onset of tertiary creep at 310 MPa. It is difficult to determine the individual contributions of the external variables influencing the directional γ' coarsening, as it appears that temperature, stress, exposure time, and creep strain are all involved in the process.

Unstressed aging of most of the alloys did not result in any γ' plate formation. However, the γ' in the alloys with higher

mismatch, Alloys B and C, did exhibit a tendency for coalescence into plate-like morphologies oriented along cube directions. The application of a tensile or compressive stress not only greatly enhances the tendency to coalesce but also provides a bias for coarsening along a single <100> direction. Only small stresses are necessary to produce directional coarsening, as the lamellar structure was observed in the threaded sections of creep specimens. Finally, the influence of applied stress is also demonstrated by the decreased coarsening rate which resulted from a decrease in stress from 310 to 207 MPa at 925^{o}C.

The influence of temperature is also evident from these results. An order of magnitude increase in coarsening rate resulted from an increase in temperature from 925 to 1000^{o}C at 207 MPa. The kinetics of coarsening at 1000^{o}C are sufficiently high to obscure any effects of the applied stress changes between 148 and 207 MPa. If the temperature dependence of directional coarsening can be treated as an Arrhenius relation, an activation energy of approximately 400 Kjoule/mole was determined for Alloy B at 207 MPa. This value is comparable to the values determined for Ostwald ripening and creep for Alloy B in the same temperature range.

It appears that a significant amount of inelastic strain is associated with the formation of γ' platelets. At 1000^{o}C, Alloy B exhibited a normal primary creep curve and also exhibited rapid γ' coarsening. However, at 925^{o}C, the γ' coarsening was much

slower and a sigmoidal primary creep region was evident. This relation is also consistent with the primary creep curves of the other alloys at 1000°C. These alloys exhibited slower γ' coarsening and incubation periods followed by sigmoidal primary creep stages.

Incubation periods and sigmoidal primary creep curves are usually associated with low initial dislocation densities and high dislocation drag stresses (159). The present alloys contain large amounts of alloying elements that serve to increase the drag stress by providing solid solution hardening and long range order. In addition, a low dislocation density in single crystal superalloys is very common, such that incubation periods have been observed previously (62,117). Consequently, it appears that the majority of these alloys posses the requirements for exhibiting sigmoidal primary creep curves, and it is not surprising that they exhibit this type of creep behavior. In the case of Alloy B at 1000°C, the lack of an incubation period and sigmoidal creep curve must be the result of some feature providing dislocation sources. The high subgrain boundary density in Alloy B may be the feature which provides the extra dislocation sources. However, another feature that can explain the high initial creep rates is the rapid γ' coarsening exhibited by Alloy B. There are several mechanisms by which creep strain can be produced by the formation of the lamellae. First, the γ' shape change is driven by a reduction in the total elastic energy, which results in elongation of

the specimen (119,120). Second, the diffusive flow of atoms that accompishes the shape change may also produce some plastic strain.

A final explanation for the association of γ' plate formation with primary creep strain is provided by the role of misfit dislocations in these alloys. Weatherly and Nicholson (107,108) have analyzed the mechanisms for the transition from a coherent to a semi-coherent interface. A particle may acquire misfit dislocations from a source in the matrix, or it may nucleate dislocations by a punching mechanism. The punching mechanism is envisioned to occur by the nucleation of two dislocation loops of opposite sign, with one loop remaining at the interface, and the other loop ejected or "punched out" into the matrix. For an alloy with negative mismatch, the interstitial loop would remain as the misfit dislocation and the vacancy loop would be ejected into the matrix. The present hypothesis is that as the γ' particles coarsen into plates, it becomes energetically favorable for them to become semi-coherent. The particles then acquire the misfit dislocations by the punching mechanism described above. This punching mechanism produces a significant number of dislocation loops that are ejected into the matrix, where they contribute to the plastic strain observed during primary creep.

In order for this proposed mechanism to be operative, two conditions must be satisfied. First, the punching mechanism must be operative, and second, the dislocations which are punched must have Burgers vectors appropriate for producing plastic strain.

The first condition can be addressed by examination of the criteria for the punching mechanism to operate. Weatherly and Nicholson have investigated these criteria, and for a spherical particle whose transformation strain is pure dilitation, the transformation strain e^T must exceed 0.04 in order for the stress to exceed the theoretical shear stress in the matrix and for punching to occur. For Alloy B at 1000°C, $e^T \approx (3)(0.006) \approx 0.02$, which is lower than the critical strain for the punching mechanism. However, the analysis of Weatherly and Nicholson was based on the situation of a single particle in an infinite matrix. This assumption is probably acceptable for alloys with small precipitate volume fractions, but is clearly violated for the present alloys with γ' volume fractions near 60 percent. The concentrations of stress which arise from elastic interactions between particles could raise the stresses to above the critical value for punching to occur. Accordingly, it appears reasonable to suggest that the punching mechanism is operative in Alloy B at 1000°C. The other alloys, however, have lower mismatches that would make the punching mechanism more unlikely. However, with the exception of Alloy C, all of these alloys exhibited significantly lower coarsening rates and lower primary creep rates and strains. Therefore it is likely that the γ' particles of these alloys acquire their misfit dislocations at a slower rate by the capture of dislocations from matrix sources. Since the capture mechanism of acquiring misfit dislocations would not pro-

vide sources for plastic strain, incubation periods and sigmoidal primary creep curves would result. Alloy C, with an intermediate value of misfit, appears to act in fashion intermediate to the two extremes.

The next point to consider is that of whether or not the misfit dislocations are appropriate for producing strain. The contention the dislocations are capable of producing strain is supported by previous work. The punching mechanism of Weatherly and Nicholson is based on the coherency stress exceeding the theoretical shear stress in the matrix, which implies that the punched dislocations would lie on slip planes. In addition, both Weatherly and Nicholson and Lasalmonie and Strudel (106) have demonstrated that the Burgers vectors of the misfit dislocations are of a/2<110> type, which are the normal slip vectors for fcc crystals.

The formation of the γ' lamellae was accomplished in the absence of any lamellar thickening. Evidently, the lateral merging of the γ' particles is a rapid and effective means of reducing the elastic and surface energies. Once the lamellar structure is formed, however, the surface energy may be further reduced by coarsening of the plates in the thickness direction. The fully formed lamellae thicken only very slowly during the creep test. The transition from the initial fine particles to the final lamellae results in a large reduction in interfacial area per unit volume, thus reducing the driving force for coarsening. In addition,

lamellar microstructures are stabilized against coarsening because the radious of curvature of a planar interface is essentially infinite, so that the chemical potential is everywhere constant (160). This implies that significant coarsening con occur only at faults in the lamellar structure. Another possible stabilizing effect could arise from the presence of the hexagonal network of interfacial dislocations, that may reduce the mobility of the γ-γ' interface (157). An indication of the stabilizing effect of the misfit dislocations on γ' coarsening was also seen in the Ostwald ripening experiments, whereby Alloys B and C were the only alloys with γ' that lost coherency during coarsening, and exhibited anomalously low coarsening rates.

The thickening process is strongly dependent on the applied stress and the creep strain. After the formation of the plates, further aging in the absence of an applied stress did not cause any thickening (117). This is consistent with the observations in this study, where decreases in the applied stress resulted in a delay in plate thickening. For example, at 1000^{o}C, the γ' plates after 435 hours at 148 MPa are still thinner than the plates after failure at 110 hours at 207 MPa. The increase in thickness for the sample which failed at 110 hours is attributed to the large amounts of plastic strain accumulated during tertiary creep. This idea of an association between plate thickness and creep strain is based on the similarity in the forms of the thickness versus time curve and the creep curves for the single crys-

tals. Both the plate thickness and the creep strain do not change very much during secondary creep, and both gradually increase as tertiary creep commences. Further support for this concept is seen in the increased plate thickness in the necked region of failed samples, in comparison to the γ' in regions away from the fracture surface. The idea that the lamellae can only coarsen at faults in the structure provides a physical mechanism for the enhancement of plate thickening by creep strain. The mechanism of creep in the present alloys involves shearing of the γ and γ' lamellae. This shearing would produce ledges at the interface, which could then enhance the thickening of the lamellae. This strain-assisted lamellar coarsening is postulated to be the cause of the onset of tertiary creep, as will be discussed in more detail below.

In summary, the formation of the γ' lamellar structure at $1000^{o}C$ was related to the creep curves of these alloys. For alloys with high γ' lattice mismatch, the formation of γ' lamellae was very rapid and was accompanied by the nucleation of misfit dislocations, which in turn provide high primary creep rates and strains. For alloys with low mismatch, γ' coarsening was slower, misfit dislocations were probably captured from sources in the matrix and resulted in low initial creep rates. The lamellar structure remained essentially constant throughout the secondary stage, until significant plate thickening occured during the tertiary creep stage. When the temperature was lowered to $925^{o}C$,

the kinetics of directional coarsening was reduced such that the lamellar structure did not become fully developed until late in the test.

Mechanical Properties

The tensile properties of the single crystal alloys exhibited some interesting results. At 1000°C, the single crystal possessed stress strain curves indicative of yield points and work softening. The presence of a yield point appears to be related to the incubation period and sigmoidal primary creep curves also observed for these materails. The existence of a yield point would be consistent with an initially low dislocation density and high initial drag stress. Yield point phenomena, including serrated yielding, and work softening behavior have been observed in other superalloy single crystals (60, 117) and in single phase γ' (30, 161). The softening has been attributed to dynamic recovery effects (117, 161).

The strength of superalloys results from a number of strengthening mechanisms such as solid solution hardening, order hardening, and coherency hardening. Alloying changes would be expected to influence all of the above mechanisms. The dependence of yield and ultimate tensile strength on composition was primarily related to the Ta plus W totals. Removal of 3 percent Ta and 1 percent W from the baseline reduced the yield and ultimate strengths by as much as 200 MPa. Substitution of 2 percent W for

the standard 3 percent Ta did not significantly affect the strenth at the 10 percent Co level, but did cause a reduction in strength at the 0 percent Co level. The strong influence of Ta and W levels on strength can be explained by the contribution of these elements to solid solution and precipitation strengthening. Because high levels of these elements increased both the solid solution hardening of γ and γ', and the volume fraction of γ', it is not possible to clarify the relative contributions of these two mechanisms. The strong influence of Co content on the strength of the baseline 3Ta-10W alloys can be explained by the increased γ-γ' lattice mismatch as Co level was reduced. The increased misfist would increase the contribution of coherency strain hardening to the strength of these alloys.

One final feature of the tensile data is the dependence of ductility on composition. The trend of higher ductility for lower strength alloys is commonly observed in many alloy systems, because hardeners increase the strength of a material by increasing the resistance to dislocation flow. These same trends were also present in the creep data, whereby the most creep resistant alloys exhibited the lowest creep ductilities.

The major emphasis of this study was placed on the creep and rupture properties of the single crystals. The phenomenological description of the creep behavior, the effects of composition on the properties, and a model that explains the main results of the study are discussed below.

The linear behavior exhibited by the double logarithmic plots of $\dot{\varepsilon}_s$, t_f, t_t, and t_s versus σ support the use of the power law expressions in Equations [11] to [15]. In some cases, an exponential law provided an equivalent fit to the experimental data. However, for the alloys with data ranging over three orders of magnitude, the semilogarithmic plot, which is appropriate for the exponential relationship, produced significant curvature. For this reason, the exponential relationship was considered unsuitable for description of the creep data.

The values of the stress exponents for these alloys were approximately equal to eight, which is very close to the value reported for columnar grained MAR-M200 in this temperature range (83). Stress exponents greater than five are typical for two phase alloys, and have sometimes been rationalized by the introduction of a back stress, such as that in Equation [7]. If the back stress is independent of the applied stress, it can be determined from a plot of $\dot{\varepsilon}_s^{1/n^*}$ versus σ_a. Here n* is the effective stress exponent, usually set at a value near four, which is appropriate for a single phase alloy. Plots of this type with the present data exhibited significant curvature, and thus were considered inappropriate. If a back stress model was to be applied to the present data, an applied stress-dependent back stress would be necessary.

Sherby and co-workers (162, 163) have proposed a model that has a number of characteristics analagous to the present investi-

gation. They considered that if the subgrain size is constant, i.e. independent of applied stress, then the stress exponent would be equal to eight. This model was supported by "constant structure" tests on pure metals, whereby the stress exponent for a given subgrain size was determined from stress reduction tests. The model also described the data for several ODS alloys where oxide particles acted to stabilize the subgrain size.

In the present alloys, the γ and γ' lamellae appear to be analagous to the subgrains formed in pure metals, and the γ and γ' interfaces appear to be analagous to subgrain boundaries. The γ-γ' interfaces contained a network of misfit dislocations and can be considered as obstacles to dislocation flow, as will be discussed in more detail below. In addition, the lamellar thickness, or "subgrain size," was a function of initial γ' size only and was not dependent on applied stress. Consequently, it appears that the present alloys behave in accordance with the model of Sherby and co-workers. The γ-γ' lamellae act as stable subgrains with a size independent of the applied stress, and thus should exhibit a stress exponent $n=8$. The n values of the present alloys were all approximately equal to eight, but some significant differences between alloys did exist. For example, the 0Ta-12W Alloys C and H exhibited $n\sim9$. Although this is not greatly different from 8, it can cause significant differences in strength, as shown by the differences in rupture lives and creep rates between Alloys B and C at low stresses.

Another significant aspect of these data is that the power law behavior held over the entire stress range studied. In many other studies of superalloys, a change in the stress dependence, in the form a break in the log-log plot, were reported (24, 80, 81, 115). This change in stress dependence is usually interpreted as an indication of a change in deformation mechanism: above the break, dislocations may either shear through or loop around the γ' particles, and below the break, dislocations bypass the γ' particles by a climb mechanism. However, all of these studies were performed on polycrystalline alloys, and the existence of the break may be due to the presence of grain boundaries. This would explain the lack of such behavior for the single crystals in this study. Further, it is also recognized that the rapid γ' coarsening during creep of the present alloys may produce a γ' morphology that prevents particle bypassing mechanisms, thus providing an alternate explanation for the absence of the change in stress dependence for the present alloys.

The time to the onset of tertiary creep, t_t, and the time to failure, t_f exhibited similar stress dependencies. However, at lower stresses, the t_t values approached the values for t_f. This is also seen by the linear behavior exhibited in the plots of the ratio t_f/t_t versus stress. Algebraic manipulations can show that if the t_f/t_t ratio increases linearly with stress, then $l=p+1$. Inspection of the values for the exponents l and p in Table V confirms this relationship for the present single crystal

alloys. These data show that the percentage of life spent in secondary creep increases as the stress is decreased. This trend is in contrast to previous studies on polycrystals, where the t_f/t_t ratio remained constant (80, 115) or increased (130) with decreasing applied stress. Again, the major differences between the present alloys and the previous materials appears to be the lack of grain boundaries and the rapid γ' coarsening in the present alloys.

The relationship between steady-state creep rate and rupture life was excellently described with the Monkman-Grant equation. This strong correlation implies that the deformation process in secondary creep contributes directly to the failure process. The value for m has been reported to equal one for some superalloys (115, 130). No explanation can be given for the small deviation from the value of one observed in the present investigation.

Examination of Figures 60-75 reveals that some experimental scatter is present in the creep-rupture data. Although this scatter is not excessive, discussion of some of the probable sources is worthwhile. One source could be the small variations in particle size from specimen to specimen. These variations could result from differences in quenching rate from the solution treatment temperature, which could be a function of the position of the bars in the specimen tray. Variations in crystal orientation could also cause some of the scatter in creep properties. Although creep anisotropy in nickel-base superalloys was very

prominent at 750°C, the activation of multiple slip systems at higher temperatures reduced the anisotropy at 1000°C (62, 164). In this study, no trends in creep properties as a function of crystal orientation could be separated, and therefore anisotropy was considered a second order effect.

The temperature dependence of the creep rate and rupture life was adequately described by the Arrhenius relationships in Equations [1]-[3]. These data produced a modulus-corrected activation energy for creep equal to approximately 350 kjoule/mole. This value is remarkably close to the values for both Ostwald ripening and directional coarsening during creep. Since the activation energy for Ostwald ripening is considered to be equal to that for self diffusion (94-96), it is tempting to say that creep in these alloys is diffusion controlled, in agreement with studies on single phase alloys (42). However, this agreement in activation may be fortuitous. First, the measured activation energy for γ' coarsening in Alloy B was somewhat higher than usually measured, as previously discussed. Second, the activation energy for creep should be affected by changes in structure with temperature, in addition to the changes is elastic modulus. Two features that are expected to be influential on the creep processes in these alloys are γ' volume fraction and γ-γ' lattice mismatch, both of which have been shown to vary with temperature.

Variations in alloy composition also produced some interesting variations in creep rupture properties. The reductions in creep

resistance as Ni was substituted for Ta was expected, and can be explained by the reductions in γ' volume fraction and solid solution hardening as Ta level was decreased. These are the same arguments used to explain the decreases in tensile strength caused by the same alloying changes. The term "solid solution hardening" is used to include all of the effects of the solute atoms, including modulus, stacking fault energy, APB energy, and diffusion.

The increases in creep life for the 0Ta-12W alloys as compared to the baseline 3Ta-10W alloys was not expected. At both 0 and 10 percent Co, the W substitution caused a reduction in rupture life and an increase in creep rate in the short term creep-rupture tests. However, as the tests became longer, the higher stress dependence of Alloys C and H resulted in a crossover such that the 0Ta-12W alloys exhibited progressively longer lives and lower creep rates than the 3Ta-10W alloys. The decrease in γ' volume fraction which resulted from the substitution of W for Ta may explain the short term tests but cannot account for the long term results. Similarly, the decreases in creep resistance as Co level increased in the baselines 3Ta-10W alloys and the 0Ta-12W alloys are difficult to resolve. The increases in tensile strength as Co level decreased from 10 to 0 was rationalized by the increased contribution of coherency strain hardening caused by the increased in lattice mismatch. However, this argument may not apply to longer term testing, whereby the effects of microstructural insta-

bilities may become more important. Many authors have suggested that higher mismatch values may decrease life by enhancing γ' coarsening and thus overaging. The effects of these compositional variations of creep properties can best be explained after a discussion of the creep mechanisms involved in these alloys.

Creep Model

Based on the phenomenological creep-rupture behavior, and on the microstructural observations of failed and interrupted specimens, a model is presented below which will attempt to explain many of the experimental results. The observations of the pronounced directional γ' coarsening during creep provide useful insights on the creep behavior of these alloys. Clearly, these materials can no longer be treated as particle strengthened alloys, since the structure more closely resembles composite systems. As previously discussed, this type of γ' coarsening was first observed by Pearson and co-workers, and the present model is based on ideas put forth in his two papers [127, 128].

A major element of the present mechanisms is that the formation of the γ' lamellae during creep produces a γ' morphology which effectively suppresses dislocation bypass mechanisms. Consequently, the more difficult γ' shearing mechanism is operative, resulting in improved creep resistance. This concept certainly appears reasonable for the present alloys, as the fully developed γ' structure consists of a continuous network of essentially in-

finitely wide lamellae. The lamellae terminated only at the edges of the specimen, and at subgrain boundaries in the alloys that possessed these boundaries. The path of dislocations slipping on {111} planes can then be divided into four different steps: shear in the γ lamellae; shear through the γ-γ' interface; shear through the γ' lamellae; and shear through the γ'-γ interface. When the processes are acting in series, as in the present case, the slowest step is the rate controlling step.

Examination of the above four steps gives an indication of which of these may be the rate controlling step. Slip in the γ phase would be limited by the solid solution elements in the γ phase. High levels of W, Cr and other elements would decrease diffusion and increase the drag stress on mobile dislocations. Slip in γ' is expected to be significantly more difficult than slip in γ, mainly as a result of a change in slip character in the long range ordered structure. As previously discussed, the shear of the $L1_2$ superlattice requires a pair of a/2 <110> dislocations. Another possible effect of the ordered structure is decreased diffusion rates (128, 159), although this effect may not be very large (165). The γ-γ' interface can also be considered as the rate limiting step. First, traversing from γ to γ' requires a change from single to paired dislocations; second, the γ-γ' interface is characterized by a stable hexagonal array of misfit dislocations that can act as obstacles to further dislocation motion. Thus, after slip through either the γ or γ' phase, the disloca-

C-2

tions would be held up at the interface. Recovery events would then be necessary to nucleate dislocation motion through the next lamella.

The present results provided evidence for clarifying some aspects for choice of the rate controlling step. Transmission electron microscopy reveals that a few dislocations were present in the γ' lamellae and none in the γ phase. This indicates that slip in γ' is more sluggish than slip in γ, as expected. Additionally, the presence of dislocations in γ' is evidence that a shearing mechanism has occurred, rather than a bypassing mechanism.

The γ-γ' interface is also considered to be very important. Two phase γ-γ' alloys are more creep resistant that either single phase γ or γ' alloys (48), a result also reported for a β-β' system (166). This confirms the importance of the interface in these properties. Pearson has similarly proposed that both the γ-γ' interface and slip in γ' contribute to the creep rate.

The influence of γ' lamellar thickness on creep rate could provide a critical test for the importance of the γ-γ' interface. Finer γ' plates would provide more interfaces per unit length in the microstructure. If the interfaces are effective obstacles, the mean slip distance of the dislocations would decrease as the lamellar thickness is refined, which would result in a decreased creep rate. Since the γ' cubes merge laterally without any thickening, a finer initial γ' size would produce finer γ' lamellae. Therfore, samples were oil quenched from the solution temperature

to refine the initial γ' size as compared to the standard forced-air quench. The oil quench did not improve the creep rate or the rupture life, but this result is inconclusive for two reasons: first the γ' size was refined by only a small amount, from 0.25 to 0.18 μm; and second, the lamellar structure of the oil quenched samples was more irregular than the standard quench, which could be a weakening effect that would counteract any effects of plate refinement. Irregularities in the lamellar structure could provide paths for easier dislocation motion.

The thickening of the platelet structure that is evident after prolonged creep exposure suggests that the γ-γ' interface does have an influence on the creep processes. As the plates thicken, the mean slip distance would increase, causing an increase in creep rate as tertiary creep commences. As previously discussed, the thickening of the lamellae is enhanced by plastic strain. Accordingly, an autocatalytic process is envisioned whereby creep strain promotes thickening of the lamellae, which causes acceleration of the creep rate; this in turn causes further thickening in the γ' structure. This process continues until necking occurs and deformation becomes heterogeneous and unstable. The same processes are still occurring after the onset of necking, as evidenced by the increased lamellar thickness in the necked region of failed specimens.

Another possible cause of the onset of tertiary creep is the propagation and linkage of cracks which have initiated at micro-

pores. Although these cracks were prominent on the fracture surfaces and in longitudinal sections of failed specimens, they were not evident in a sample interrupted in the tertiary stage. Therefore, the initiation and growth of these cracks cannot be considered as the cause of the onset of tertiary creep, but instead appear to be the final fracture mode that occurs after the onset of tertiary creep and necking.

Note that this model predicts that high γ-γ' lattice mismatch is actually beneficial for creep resistance. The beneficial effects of high mismatch involve the increased barrier to dislocation motion from either elastic coherency strains or the finer spacing of misfit dislocations. The negative effect of high mismatch, which is a higher γ' coarsening rate, is minimized in the present case. Increased mismatch does cause very rapid directional γ' coarsening, but only in the initial portions of the creep test. The rapid directional coarsening observed in the present study did not cause the typical overaging response whereby dislocation bypassing mechanisms become easier as the particles grow. In contrast, the formation of the lamellae suppressed the bypassing mechanisms. These concepts are supported by the lack of any correlation between creep resistance and Ostwald ripening rate.

Once formed, the γ' lamellae coarsen only very slowly during the remainder of the creep life. Lower mismatch values can actually increase the plate thickening which occurs during the later stages of the creep test. As previously discussed, this thick-

ening appears to be enhanced by creep strain. Therefore, a lower mismatch would result in a smaller barrier to dislocation flow, and causes a higher steady state creep rate. This higher strain rate would therefore enhance the plate thickening rate, which in turn would result in an earlier onset of tertiary creep and failure. It is also possible that decreased mismatch may decrease creep strength by decreasing the directional coarsening rate. This would delay the benefits attained from the fully developed structure, i.e., suppression of bypassing mechanisms.

The influence of Co on the present alloys supports the postulate that high lattice mismatch is beneficial for creep properties. The effects of Co cannot be attributed to solid solution hardening by Co, because the Co additions actually decreased the creep resistance of the 0Ta-12W and 3Ta-10W alloys. In addition, Co is not expected to be a potent hardener of either γ (9, 10) or γ' (11). Cobalt additions increase the solubility for W in γ and γ'. This causes the W which is contained in the α and μ phases in the zero percent Co Alloy B to be in solid solution for the five percent Co Alloy E. Again, this effect would be expected to increase the strength of the 5 percent Co alloy if it would have any effect at all. Thus, it appears likely that the decreases in creep resistance with increasing Co level was not caused by decreases in strength of the individual phases. The strength of the γ-γ' interface, however, was strongly influenced by Co content. As Co level increased from 0 to 5 percent, the lattice mismatch δ

at 1000°C decreased in magnitude from approximately -0.006 to -0.003. This decrease in mismatch would increase the spacing of the hexagonal misfit dislocation array, as confirmed by the TEM images in Figures 45 and 47. The increase in lattice mismatch can therefore account for the increased creep resistance of these alloys as Co level was decreased.

The influence of W and Ta contents on the creep properties of the single crystal alloys was more puzzling. For example, Alloy C had a slightly lower γ' volume fraction, γ-γ' mismatch, and Ta plus W total than Alloy B, all of which would be expected to weaken Alloy C in comparison to Alloy B. In fact, these features may be the reasons for the results of the short term tests, whereby Alloy B was indeed stronger. However, some other microstructural feature must cause the observed cross-over in creep resistance at lower applied stresses. One could argue that Alloy C exhibited better creep resistance at low stresses because it possessed smaller amounts of W-rich phases than Alloy B. However, this could not explain the same trends in strength at 10 percent Co, where both Alloys H and G were free of any third phases. One possibility is that the W is more effective as a solid solution hardener than Ta. Unfortunately, only limited data are available or the influence of alloying on the various mechanisms by which a solute atom may improve creep resistance. Because the effect of the W substitution is more prominent at lower stresses and thus longer lives, it is plausible that W influences the diffusivity.

Diffusion can enter into the creep processes in the present model by controlling the recovery events at the γ-γ' interface, and also possibly by controlling the viscous slip in the two phases. Thus, a possible explanation for the cross-over in strength exhibited between the 0Ta-12W and 3Ta-10W alloys is provided. At high applied stresses, the slight decreases in volume fraction and mismatch causes the 0Ta-12W alloys to be less resistant to plastic flow. At progressively lower stresses, solid solution strengthening, and in particular low diffusivity, becomes more important; this results in the cross-over in creep strength. However, it is recognized that further study is necessary to establish the influence of refractory metals on the creep properties of superalloys.

The creep processes at the lower temperatures of 925°C did not appear to be totally analagous to the processes at 1000°C. Although the stress exponents at the two temperatures were similar, other features were dissimilar. The primary creep stage was sigmoidal at 925°C, in contrast to the normal primary stage 1000°C. In addition, the onset of tertiary stage was more gradual and occurred at a lower fraction of the rupture life at 925°C.

Many of the differences between the behaviors at the two temperatures can be traced to the slower γ' coarsening at 925°C. The sigmoidal primary creep curve has previously been attributed to the slower formation of the γ' lamellae. The achievement of the fully developmed lamellar structure, which sometimes was delayed

until after the onset of tertiary creep, implies that the γ' plate morphology was not as influential in the creep mechanisms at this temperature. Furthermore, a sample pre-crept at 1000°C to form the γ' lamellae prior to testing at 925°C did not show an improvement in properties. This result suggests that, at 925°C, the barrier to dislocation motion provided by the cubical γ' particles is equivalent to that provided by the γ' plates. This situation is possible if dislocation bypassing of the cubical γ' particles is suppressed at 925°C, thus resulting in the γ' shearing mechanism becoming operative for both particle morphologies. This suppression could be the result of the decreased climb mobility at the lower temperature. Consequently, the benefit of the γ' lamellar structure, which is the suppression of dislocation bypassing mechanisms, is not necessary at the lower temperature of 925°C, the γ' shearing mode is operative for both precipitate morphologies, and the resulting creep properties are comparable.

Finally, the influence of composition was different at the two temperatures. The effects of Co level, which were so prominent at 1000°C, were reduced and possibly even reversed at 925°C, and the substitution of W for Ta also did not affect the creep properties as significantly. These data also suggest that the creep mechanisms are different at the lower temperature. More extensive testing is required to clarify the creep processes at 925°C.

In summary, the creep behavior of the single crystal alloys is significantly influenced by the γ' morphology which develops

during creep. At high temperature, the γ' particles rapidly coalesced into lamellae perpendicular to the applied stress. This lamellar structure prevented dislocation bypassing of the γ' phase, thus forcing the dislocations to shear through the lamellae. Although slip in the γ' phase may contribute to the creep resistance of the alloys, it is likely that shear through the γ-γ' interface is the most difficult step. A hexagonal array of misfit dislocations was present at the interface, and acted as a barrier to dislocation motion. The array may also act to stabilize the γ' lamellae against coarsening in the thickness direction. Strain enhanced thickening of the γ' lamellae resulted in a gradual increase in creep rate as the tertiary creep stage commenced.

Decreases in Co level from 10 to 0 percent caused significant increases in creep resistance for the alloys with high refractory metal levels. These decreases in Co concentration did not significantly influence the strength of the individual γ and γ' phases, but did increase the γ-γ' mismatch. The increases in mismatch resulted in a finer misfit dislocation network, which is believed to provide a stronger obstacle to dislocation flow, and also to stabilize the γ' lamellae against thickening. Removal of Ta from the baseline alloys caused large reductions in creep resistance, which can be explained by low values of γ' volume fraction, γ-γ' mismatch, and solid solution hardening of γ and γ'. Substitution of W for Ta resulted in improved creep lives at low stresses, believed to be caused by the increased effectiveness of W as a solid

solution hardener. As a result of the decreased rate of directional coarsening, the γ-γ' lamellar structure did not appear to be very influential at 925°C. This was also evident from the decreased influence of composition on creep properties at this temperature.

CONCLUSIONS

1. Removal of Ta and W from the baseline 3Ta-10W alloys to form the 0Ta-9W alloys caused a large reduction in γ' solvus temperature and γ' volume fraction. Substitution of W for Ta to form the 0Ta-12W alloys resulted in intermediate reductions in solvus temperature and volume fraction. The amount of γ' was independent of Co level, but the γ' solvus temperature increased significantly as Co content was reduced from 10 to 0 percent.
2. The partitioning of elements between the γ and γ' phases did not vary appreciably as the alloy composition varied. Tantalum and Ti partitioned almost totally to γ'; Al and W partitioned preferentially to γ'; and Co, Cr, and Mo partitioned preferentially to γ.
3. The γ' lattice parameter was independent of Co content but increased as the total refractory metal level increased. At the 0 percent Co level, the 3Ta-10W alloy exhibited a room temperature lattice mismatch $\delta = -0.0035$, and the 0Ta-12W alloy exhibited $\delta = -0.002$. The 0Ta-9W alloys and all alloys with 5 and 10 percent Co possessed mismatch values below the detection limit.

4. Both the γ' volume fraction and γ-γ' lattice mismatch exhibited significant temperature dependencies. The amount of γ' at 1000°C was about 10 volume percent lower than the amount at room temperature. As temperature increased from 25 to 1000°C, the lattice mismatch of Alloy B changed from -0.0035 to -0.006, and that of Alloy E changed from a value unmeasurably small to -0.003.
5. Small quantities of W-rich α and μ phases were present in alloys with high Ta plus W totals and 0 percent Co. Reduction of total refractory metal level, or addition of 5 percent Co was sufficient to prevent the formation of α and μ.
6. For the alloys with γ' that remained coherent, the unstressed γ' coarsening rate increased as Co level was reduced from 10 to 0 percent. The two alloys with high lattice mismatch became semi-coherent during aging and exhibited anomalously low coarsening rates.
7. Oriented γ' coarsening was very prominent during creep. The γ' morphology was characterized by plates perpendicular to an applied tensile stress and by two sets of plates parallel to an applied compressive stress. Discrepancies exist between the predictions of isotropic elasticity theory and the experimental observations on a number of alloys.
8. The oriented coarsening occurred very rapidly during creep at 1000°C, especially for alloys with high lattice mismatch. For Alloy B, the formation of a continuous γ-γ' lamellar

structure was completed during the primary creep stage at this temperature. At 925°C, the γ' coarsening kinetics were reduced such that the lamellar structure was not fully developed until the secondary or tertiary stages.

9. Decreases in Co level from 10 to 0 percent caused significant increases in the 1000°C yield and ultimate tensile strengths of the 3Ta-10W alloys, but the effect of Co was much weaker for alloys with other refractory metal contents. Reduction of Ta and W content to form the 0Ta-9W alloys caused large reductions in tensile strength, and substitution of W for Ta caused intermediate decreases in strength. Alloys with higher strengths exhibited lower ductilities.
10. The changes in tensile strength with refractory metal level were related to the increases in γ' volume fraction and solid solution hardening which resulted from high Ta plus W totals. The influence of Co on the strength of the 3Ta-10W alloys was attributed to coherency strain hardening associated with the increased lattice mismatch as Co level decreased.
11. The steady state creep rate, time to failure, time to the onset of secondary creep, and the time to the onset of tertiary creep all exhibited power law dependencies on the applied stress. The stress exponent for the steady state creep rate was approximately 8 for all alloys, although some small but significant differences between alloys did exist. The modulus corrected activation energy for creep was comparable to the

activation energy for Ostwald ripening.

12. The rapid γ' coalescence during creep occurs in the absence of any plate thickening. Once formed, gradual thickening of the lamellae was evident after prolonged creep exposure. The lamellar morphology suppressed particle bypass mechanisms, thus forcing the dislocations to shear through the γ' phase and the γ-γ' interfaces. A hexagonal array of interfacial dislocations is believed to be an obstacle to dislocation motion. The plate thickening appeared to be strain enhanced, and to be the cause of the onset of tertiary creep.
13. Reduction of Ta and W to form the 0Ta-9W alloys caused large reductions in creep resistance. Substitution of W for Ta to form the 0Ta-12W alloys resulted in a decrease in creep resistance at high stresses, and an increase in creep strength at low stresses. Reduction of Co content from 10 to 0 percent caused large increases in creep resistance for alloys with high Ta plus W totals.
14. The decreases in creep life for the 0Ta-9W alloys were related to the decreases in γ' volume fraction, γ-γ' mismatch, and solid solution hardening. The crossover in creep resistance between the 3Ta-10W and 0Ta-12W alloys was not easily explained. The decreased life of the 0Ta-12W alloys at high stresses was attributed to the slight decreases in γ' volume fraction and γ-γ' mismatch, although it remains unclear as to why W appears to be a more effective solid solution hardener

than Ta at low stresses. The increases in life as Co content decreased were consistent with increased γ-γ' lattice mismatch. High values of lattice mismatch resulted in a finer dislocation network at the γ-γ' interface, thus providing a more effective barrier for dislocation motion.

15. The influence of composition on creep behavior at 925^{o}C was less prominent than the effects at 1000^{o}C. This difference was attributed to the reduced γ' coarsening kinetics and the weaker influence of the γ-γ' lamellar structure at the lower temperature.

REFERENCES

1. J. K. Tien, T. E. Howson, G. L. Chen, and X. S. Xie; J. Metals, October 1980, p. 12.

2. J. R. Stephens; NASA TM-82852, 1982.

3. C. T. Sims and W. C. Hagel; The Superalloys, John Wiley and Sons, Inc., New York, 1972.

4. O. H. Kriege and J. M. Baris; Trans ASM, 1962, Vol. 62, p. 195.

5. R. F. Decker; Steel Strengthening Mechanisms Symposium, Climax Molybdenum Company, 1969, p. 147.

6. High Temperature, High Strength Nickel-Base Alloys, 3rd Edition, The International Nickel Company, Inc., 1977.

7. N. S. Stoloff; in The Superalloys, ed. by C. T. Sims and W. C. Hagel, John Wiley and Sons, Inc., New York, 1972, p. 79.

8. R. Nordheim and N. J. Grant; J. Inst. Metals., 1954, Vol. 82, p. 410.

9. R. M. N. Pelloux and N. J. Grant; Trans. TMS-AIME, 1960, Vol. 218, p. 232.

10. T. H. Hazlett and E. R. Parker; Trans. ASM, 1954, Vol. 46, p. 701.

11. R. W. Guard and H. H. Westbrook; Trans. AIME, 1959, Vol. 215, p. 807.

12. P. A. Flinn; Trans. TMS-AIME, 1960, Vol. 218, p. 145.13.

13. P. H. Thornton, R. G. Davies, and T. L. Johnson; Metall. Trans., 1970, Vol. 1, p. 207.

14. J. A. Lopez and G. F. Hancock; Phys. Stat. Sol. (a), 1970, Vol. 2, p. 469.

15. R. J. Taunt and B. Ralph; Phil. Mag., 1977, Vol. 25, p. 485.

16. R. A. Mulford and D. P. Pope; Acta. Metall., 1973, Vol. 21, p. 1375.

17. E. Kuramoto, and D. P. Pope; Acta. Metall., 1978, Vol. 26, p. 207.

18. C. Lall, S. Chin, and D. P. Pope; Metall. Trans., 1979, Vol 10A, p. 1323.

19. A. Guimier and J. L. Strudel; Second Int. Conf. Strength Metals and Alloys, ASM, 1970, p. 1145.

20. D. A. Grose and G. S. Ansell; Metall. Trans., 1981, Vol. 12A, p. 1631.

21. B. H. Kear, A. F. Giamei, G. R. Leverant, and J. M. Oblak; Scripta Metall., 1969, Vol. 3, p. 455.

22. E. Orowan; Discussion in the Symposium on Internal Stresses in Metals and Alloys, Inst. Metals, London, 1948, p. 451.

23. P. Beardmore, R. G. Davies, and T. L. Johnston; Trans. TMS-AIME, 1969, Vol. 245, p. 1537.

24. B. Bergman; Scand. J. Metall., 1975, Vol. 4, p. 97.

25. L. K. Singhal and J. W. Martin; Acta. Metall., 1968, Vol. 16, p. 947.

26. R. F. Decker and J. R. Mihalisin; Trans. ASM, 1969, Vol. 62, p. 481.

27. V. A. Phillips; Phil. Mag., 1967, Vol. 16, p. 103.

28. V. Munjal and A. J. Ardell; Acta. Metall., 1975, Vol. 23, p. 513.

29. A. J. Ardell, V. Munjal, and D. J. Chellman; Metall. Trans., 1976, Vol. 7A, p. 1263.

30. S. M. Copley and B. H. Kear; Trans. TMS-AIME, 1967, Vol. 239, p. 977.

31. S. M. Copley and B. H. Kear; Trans. TMS-AIME, 1967, Vol. 239, p. 984.

32. V. Munjal and A. J. Ardell; Acta. Metall., 1976, Vol. 24, p. 827.

33. A. W. Thompson and J. A. Brooks; Acta. Metall., 1982, Vol. 30, p. 2197.

34. N. F. Mott and F. R. N. Nabarro; Proc. Phys. Soc., 1940, Vol. 52, p. 86.

35. J. D. Eshelby; Proc. Roy. Soc., 1957, Vol. A241, p. 376.

36. L. M. Brown and R. K. Ham; in Strengthening Methods in Crystals ed. by A. Kelly and R. B. Nicholson, John Wiley and Sons, Inc., New York, 1971, p. 12.

37. O. D. Sherby; Trans. TMS-AIME, 1958, Vol. 212, p. 708.

38. O. D. Sherby and A. K. Miller; J. Eng. Mat. Tech., 1979, Vol. 101, p. 387.

39. O. D. Sherby and J. Weertman; Acta. Metall., 1979, Vol. 27, p. 387.

40. A. K. Mukherjee, J. E. Bird, and J. E. Dorn; ASM Trans. Quart., 1969, Vol. 62, p. 155.

41. T. G. Langdon; 6th Int. Conf. Strength of Metals and Alloys, Ed. by R. C. Gifkins, Pergamon Press, Oxford, 1982, Vol. 3, p. 1105.

42. W. D. Nix and B. Ilschner; 5th Int. Conf. Strength of Metals and Alloys, Ed. by P. Haasen, V. Gerold and G. Kostor, Pergamon Press, Oxford, 1979, Vol. 3, p. 1503.

43. F. R. N. Nabarro; Report of a Conference on Strength of Solids, The Physical Society, London, p. 75.

44. C. Herring; J. Appl. Phys., 1950, Vol. 21, p. 437.

45. R. L. Coble; J. Appl. Phys., 1963, Vol. 34, p. 1679.

46. T. G. Langdon; Phil. Mag., 1970, Vol. 22, p. 689.

47. T. G. Langdon; Metals Forum, 1981, Vol. 4, p. 14.

48. R. G. Davies and T. L. Johnson; in Ordered Alloys: Structural Applications and Physical Metallurgy, ed. by B. H. Kear, C. T. Sims, N. S. Stoloff, and J. H. Westbrook, Claitor's Publishing Division, Baton Rouge, 1970, p. 447.

49. C. T. Sims; J. Metals, October 1966, p. 1119.

50. J. E. Doherty, B. H. Kear, and A. F. Giamei; J. Metals, Nov. 1971, p. 59.

51. J. K. Tien and R. P. Gamble; Metal Trans., 1971, Vol. 2, p. 1663.

52. T. B. Gibbons; Met. Science J., 1972, Vol. 6, p. 13.

53. R. F. Decker and J. W. Freeman; Trans. TMS-AIME, 1960, Vol. 218, p. 277.

54. P. S. Kotval, J. D. Venables, and R. W. Calder; Metall. Trans., 1972, Vol. 3, p. 453.

55. J. M. Dahl, W. F. Danesi, and G. R. Dunn; Metall. Trans., 1973, Vol. 4, p. 1087.

56. R. T. Holt and W. Wallace; Int. Metals Review, March 1976, p. 1.

57. B. J. Piearcey, B. H. Kear, and R. W. Smaskey; Trans. ASM, 1967, Vol. 60, p. 634.

58. F. L. VerSnyder, and R. W. Guard; Trans. ASM, 1960, Vol. 52, p. 485.

59. M. Gell, D. N. Duhl, A. F. Giamei; in Superalloys 1980, Proc. 4th Int. Symp. on Superalloys, Ed. by J. K. Tien, S. T. Wlodek, H. Morrow, M. Gell, and G. E. Maurer, ASM, Metals Park, 1980, p. 205.

60. B. H. Kear, and B. J. Piearcey; Trans. TMS-AIME, 1967, Vol. 239, p. 1209.

61. G. R. Leverant, B. H. Kear, and J. M. Oblak; Metall. Trans., 1973, Vol. 4, p. 355.

62. G. R. Leverant and B. H. Kear; Metall. Trans., 1970, Vol. 1, p. 491.

63. T. E. Strangman, G. S. Hoppin, C. M. Phipps, K. Harris, and R. E. Schwer; in Superalloys 1980, Proc. 4th Int. Sym. on Superalloys, Ed. by J. K. Tien, S. T. Wlodek, H. Morrow, M. Gell and G. E. Maurer, ASM, Metals Park, 1980, p. 215.

64. R. Lagneborg and B. Bergman; Met. Sci., 1976, Vol. 10, p. 20.

65. R. Lagneborg; Scripta Metall., 1973, Vol. 7, p. 605.

66. J. Weertman; J. Appl. Phys., 1955, Vol. 26, p. 1213.

67. J. Weertman; Trans. ASM, 1968, Vol. 61, p. 681.

68. F. A. Mohamed and T. G. Langdon; Acta. Metall., 1974, Vol. 22, p. 779.

69. B. A. Wilcox and A. H. Clauer; Trans. TMS-AIME, 1966, Vol. 236, p. 570.

70. O. Ajaja, T. E. Howson, S. Purushothaman, and J. K. Tien; Mat. Sci. Eng., 1980, Vol. 44, p. 165.

71. J. C. Gibeling and W. D. Nix; Mat. Sci. Eng., 1980, Vol. 45, p. 123.

72. J. C. Gibeling and W. D. Nix; Met Sci., 1977, Vol. 11, p. 453.

73. R. W. Lund and W. D. Nix; Acta. Metall., 1976, Vol. 24, p. 469.

74. J. H. Hausselt and W. D. Nix; Acta. Metall., 1977, Vol. 25, p. 595.

75. J. D. Parker and B. Wilshire; Met. Sci., 1978, Vol. 12, p. 453.

76. J. D. Parker and B. Wilshire; Phil. Mag., 1980, Vol. 41A, p. 665.

77. W. J. Evans and G. F. Harrison; Met. Sci., 1979, Vol. 13, p. 346.

78. G. J. Lloyd and R. J. McElroy; Acta. Metall., 1974, Vol. 22, p. 339.

79. S. Takeuchi and A. S. Argon; J. Mat. Sci., 1976, Vol. 11, p. 1542.

80. J. P. Dennison, P. D. Holmes, and B. Wilshire; Mat. Sci. Eng., 1978, Vol. 33, p. 35.

81. W. J. Evans and G. F. Harrison; Met. Sci., 1979, Vol. 13, p. 641.

82. R. D. Kane and L. J. Ebert; Metall. Trans., 1976, Vol. 7A, p. 133.

83. G. A. Webster and B. J. Piearcey; Met. Sci. J., 1967, Vol. 1, p. 97.

84. G. J. Lloyd and J. W. Martin; Mat. Sci. Eng., 1980, Vol. 46, p. 1.

85. J. Askill; Tracer Diffusion Data for Metals, Alloys, and Simple Oxides, Plenum Publishing Corp., New York, 1970.

86. F. Gabrielli and V. Lupinc; Proc. 6th Int. Conf. Strength of Metals and Alloys, Ed. by R. C. Grifkins, Pergamon Press, Oxford, 1982, Vol. 2, p. 607.

87. T. B. Gibbons and B. E. Hopkins; Met. Sci. J., 1971, Vol. 5, p. 233.

88. G. N. Maniar and J. E. Bridge; Metall. Trans., 1971, Vol. 2, p. 95.

89. R. Watanabe and T. Kuno; Trans. Iron Steel Inst. Jap., 1976, Vol. 16, p. 437.

90. C. G. Bieber and J. R. Mihalisin; Proc. 2nd Int. Conf. Strength Metals and Alloys, ASM, 1970, Vol. III, p. 1031.

91. J. J. Jackson, M. J. Donachie, R. J. Henricks, and M. Gell; Metall. Trans., 1977, Vol. 8A, p. 1615.

92. I. M. Lifshitz and V. V. Slyozov; J. Phys. Chem. Solids, 1961, Vol. 19, p. 35.

93. C. Wagner; Z. Elektrochem., 1961, Vol. 65, p. 581.

94. A. J. Ardell; Acta. Metall., 1968, Vol. 16, p. 511.

95. A. J. Ardell; Metall. Trans., 1970, Vol. 1, p. 525.

96. A. J. Ardell and R. B. Nicholson; J. Phys. Chem. Solids, 1966, Vol. 27, p. 1793.

97. A. F. Smith; Acta. Metall., 1967, Vol. 15, p. 1867.

98. E. H. VanDerMolen, J. M. Oblak, and O H. Kriege; Metall. Trans., 1971, Vol. 2, p. 1627.

99. V. Biss and D. L. Sponseller; Metall. Trans., 1973, Vol. 4, p. 1953.

100. B. A. Parker, and D. R. F. West; J. Aust. Inst. of Metals, 1-969, Vol. 14, p. 102.

101. A. J. Ardell; Acta. Metall., 1972, Vol. 20, p. 61.

102. D. J. Chellman and A. J. Ardell; Acta. Metall., 1974, Vol. 2-2, p. 577.

103. C. K. L. Davies, P. Nash, and R. N. Stevens; Acta. Metall., 1980, Vol. 28, p. 174.

104. C. K. L. Davies, P. Nash, and R. N. Stevens; J. Mat. Sci., 1-980, Vol. 15, p. 1521.

105. A. D. Brailsford and P. Wynblatt; Acta. Metall., 1979, Vol. 27, p. 489.

106. A. Lasalmonie and J. L. Strudel; Phil. Mag., 1975, Vol. 32, p. 937.

107. G. C. Weatherly and R. B. Nicholson; Phil. Mag., 1968, Vol. 17, p. 801.

108. G. C. Weatherly; Phil. Mag., 1968, Vol. 17, p. 791.

109. J. W. Matthews; in Dislocation in Solids ed. by F. R. N. Nabarro, North Holland Publishing Co., Amsterdam, 1979, Vol. 2, p. 461.

110. P. K. Rastogi and A. J. Ardell; Acta. Metall., 1971, Vol. 19, p. 321.

111. R. A. Ricks, A. J. Porter, and R. C. Ecob; Acta. Metall., 19-83, Vol. 31, p. 43.

112. P. K. Footner and B. P. Richards; J. Mat. Sci., 1982, Vol. 1-7, p. 2141.

113. J. W. Martin and F. J. Humphreys; Scripta Metall., 1974, Vol. 8, p. 679.

114. R. A. Stevens and P. E. J. Flewitt; Mat. Sci. Eng., 1979, Vol. 37, p. 237.

115. H. Burt, J. P. Dennison, C. Elliot, and B. Wilshire; Mat. Sci. Eng., 1982, Vol. 53, p. 245.

116. C. P. Sullivan, G. A. Webster, and B. J. Piearcey; J. Inst. Metals, 1968, Vol. 96, p. 274.

117. C. Carry and J. L. Strudel; Acta. Metall., 1978, Vol. 26, p. 859.

118. R. A. Stevens and P. E. J. Flewitt; Mat. Sci. Eng., 1981, Vol. 50, p. 271.

119. J. K. Tien and R. P. Gamble; Metall. Trans., 1972, Vol. 3A, p. 2137.

120. J. K. Tien and S. M. Copley; Metall. Trans., 1971, Vol. 2A, p. 543.

121. S. D. Antolovich, P. Domas, and J. L. Strudel; Metall. Trans., 1979, Vol. 10A, p. 1859.

122. C. Carry and J. L. Strudel; Proc. 4th Int. Conf. Strength of Metals and Alloys, 1976, Vol. 1, p. 329.

123. T. Miyazaki, K. Nakamura, and H. Mori; J. Mat. Sci., 1979, Vol. 14, p. 1827.

124. A. Pineau; Acta. Metall., 1976, Vol. 24, p. 559.

125. J. D. Eshelby; Proc. R. Soc. (A), 1957, Vol. 241, p. 376.

126. J. D. Eshelby; Prog. Solid. Mech., Ed. by I. N. Sneddon and R. Hill, 1961, Vol. 2, p. 87.

127. D. D. Pearson, F. D. Lemkey, and B. H. Kear; Superalloys 1980, Proc. 4th Int. Symp. Superalloys, ed. by J. K. Tien, S. T. Wlodek, H. Morrow, M. Gell, and G. E. Maurer, ASM, Metals Park, 1980, p. 513.

128. D. D. Pearson, B. H. Kear, and F. D. Lemkey; Creep and Fracture of Engineering Materials and Structures, ed. by B. Wilshire and D. R. J. Owen, Pineridge Press, Swansea, UK, 1981, p. 213.

129. I. L. Mirkin and O. D. Kancheev; Met. Science Heat Treatment, 1967, Vol. 1, p. 10.

130. C. C. Law and M. J. Blackburn; Metall. Trans., 1980, Vol. 11-A, p. 495.

131. R. Norhheim and N. J. Grant; J. Metals, 1954, Vol. 6, p. 211.

132. R. L. Dreshfield and R. L. Ashbrook; NASA TN D-6015, 1970.

133. M. V. Nathal, R. D. Maier, and L. J. Ebert; Metall. Trans. 1-982, Vol. 13A, p. 1775.

134. M. V. Nathal, R. D. Maier, and L. J. Ebert; Metall. Trans., 1982, Vol. 13A, p. 1767.

135. G. E. Maurer, L. A. Jackman, and J. A. Domingue; in Superalloys 1980, Proc. 4th Int. Symp. Superalloys, ed. by J. K. Tien, S. T. Wlodek, H. Morrow, M. Gell, and G. E. Maurer, ASM, Metals Park, 1980, p. 43.

136. R. N. Jarrett and J. K. Tien; Metall. Trans., 1982, Vol. 13A, p. 1021.

137. R. V. Miner; Metall. Trans., 1977, Vol. 8A, p. 259.

138. J. R. Mihalisin; in Reviews on High Temperature Materials, ed. by J. B. Newkirk, Freund Publishing House, Ltd., Tel Aviv, 1974, Vol. 2, No. 3, p. 244.

139. G. C. Fryburg, C. A. Stearns, and F. J. Kohl; J.Electrochemical Soc., 1977, Vol. 124, p. 1147.

140. S. W. Yang; Oxidation of Metals, 1981, Vol. 15, p. 375.

141. A. F. Giamei and B. H. Kear; Metall. Trans., 1970, Vol. 1, p. 2185.

142. S. M. Copley, A. F. Giamei, S. M. Johnson, and M. F. Hornbecker; Metall. Trans., 1970, Vol. 1, p. 2193.

143. M. J. Donachie and O. H. Kriege, J.; Materials, 1972, Vol. 7, p. 269.

144. D. C. Montgomery and E. A. Peck; Introduction to Linear Regression Analysis, John Wiley and Sons, New York, 1982, p. 184.

145. J. M. Oblak and B. H. Kear; in Electron Microscopy and Structure of Materials, ed. by G. Thomas, R. M. Fulrath, and R. M. Fisher, Univ. of California Press, Berkely, CA, 1971, p. 566.

146. R. L. Dreshfield; NASA TMX-73663, 1977.

147. F. C. Monkman and N. J. Grant; Proc. ASTM, 1956, Vol. 56, p. 834.

148. T. E. Strangman, B. R. Heath, and M. Fujii, NASA Cr-168218, 1983.

149. F. C. Hull; Metal Progress., 1969, Vol. 96, p. 139.

150. W. T. Loomis, J. W. Freeman, and D. L. Sponseller; Metall. Trans., 1972, Vol. 3, p. 989.

151. P. G. Shewmon; Transformations in Metals, McGraw-Hill, New York, 1969, p. 58.

152. R. L. Dreshfield and J. F. Wallace; Metall. Trans.,, 1974, Vol. 5, p. 71.

153. E. Aigeltinger and M. Kersker; Metals Forum, 1981, Vol. 4, p. 112.

154. W. B. Pearson; Handbook of Lattice Spacings and Structures of Metals, Pergamon, New York, 1959, Vols. I, II, p. 776.

155. C. E. Lowell, R. G. Garlick, and B. Henry; Metall. Trans., 1976, Vol. 7A, p. 655.

156. A. J. Porter, R. A. Ricks, and R. C. Ecob; J. Mat. Sci., 1983, Vol. 18, p. 1895.

157. H. I. Aaronson, in Decomposition of Austenite by Diffusional Processes, Ed. by V. F. Zackay and H. I. Aaronson, Interscience Publishers, New York, 1960, p. 387.

158. R. A. MacKay; PhD. Thesis, Case Western Reserve University, Cleveland, OH, 1984.

159. P. R. Strutt and R. A. Dodd; in Ordered Alloys: Structural Applications and Physical Metallurgy, ed. by B. H. Kear, C. T. Sims, N. S. Stolloff, and J. H. Westbrook, 1969, Claitor's Publishing, Baton Rouge, LA, p. 475.

160. J. W. Martins and R.D. Doherty, Stability of Microstructure in Metallic Systems, Cambridge University Press, Cambridge, 1976, p.154.

161. A. E. Saton-Bevon, Phil. Mag. A., 1983, Vol. 47, p. 939.

162. J. Lin and O. D. Sherby, Res. Mechanica, 1981, Vol. 2, p. 251.

163. O. D. Sherby, R. H. Klundt, and A. K. Miller, Metall. Trans., 1977, Vol. 8A, p. 843.

164. R. A. MacKay and R. D. Maier, Metall Trans. 1982, Vol. 13A, p. 1747.

165. M. M. P. Janssen, Metall. Trans., 1973, Vol. 4, p. 1623.

166. R. S. Polvani, Wen-Shian Tzeng, and P. R. Strutt, Metall. Trans., 1976, Vol. 7A, p. 33.

TABLE I

AIM COMPOSITIONS[a] OF ALLOYS STUDIED

Alloy	Cobalt	Tantalum	Tungsten	Comments
A	0	0	10	
B	0	3	10	NASAIR 100 (ref. 63)
C	0	0	13	
D	5	0	10	
E	5	3	10	Alloy 3 (ref. 63)
F	10	0	10	
G	10	3	10	"stripped"[b] MAR-M247
H	10	0	13	

Notes:

a. All values in weight percent. The following elements will remain constant at levels appropriate for MAR-M247: Al=5.5, Cr=8.5, Ti=1.0, Mo=0.7, Ni= balance.

b. All alloys will be stripped of the grain boundary elements C, B, Zr, and Hf.

TABLE II

CHEMICAL ANALYSIS OF SINGLE CRYSTAL ALLOYS (WEIGHT PERCENT)

Alloy:	A		B		C		D		E		F		G		H	
	a	b	a	b	a	b	a	b	a	b	a	b	a	b	a	b
Al	5.42	5.00	5.81	5.55	5.52	5.06	5.48	5.00	5.37	5.04	5.47	5.05	5.32	5.10	5.46	5.07
Cr	9.01	9.35	9.16	9.26	8.75	8.53	9.00	8.58	8.56	8.44	9.12	8.59	8.64	8.45	8.63	8.53
Co	0	0	0	0	0	0	5.31	5.05	5.14	4.93	10.4	9.84	10.4	9.75	10.3	9.91
Mo	0.68	0.66	0.92	1.01	0.65	0.65	0.66	0.66	0.64	0.64	0.65	0.66	0.64	0.65	0.66	0.66
Ni	74.1	70.5	69.0	64.7	71.9	66.5	69.1	64.5	65.3	61.3	64.0	60.1	60.6	56.7	62.2	61.3
Ta	0	0	2.80	2.84	0	0	0	0	2.95	3.02	0	0	2.60	3.00	0	0
Ti	1.79	1.02	1.70	1.25	1.69	1.04	1.69	1.07	1.68	1.06	1.68	1.05	1.68	1.08	1.28	1.06
W	9.00	9.38	10.7	9.70	11.5	12.1	8.70	9.29	10.4	9.33	8.70	9.37	10.1	9.36	11.4	12.0
O*	32		20		37		27		33		30		37		50	
C	0.002		0.005		0.005		0.003		0.004		0.004		0.006		0.002	
B	0.001		0.003		0.005		0.001		0.002		0.001		0.001		0.001	
Zr	<0.01		<0.01		<0.01		<0.01		<0.01		<0.01		<0.01		<0.01	
N*	3		4		3		3		5		3		4		4	

Notes: *ppm; a and b denote different vendors.

TABLE III

COMPOSITION OF PHASES IN THE SINGLE CRYSTAL ALLOYS (ATOMIC PERCENT)

Alloy:	A		B				C		D		E		F		G		H	
Phase:	γ	γ'	γ	γ'	α*	α+	γ	γ'	γ	γ'	γ	γ'	γ	γ'	γ	γ'	γ	γ'
Al	4.46	16.4	5.29	17.4	5.00	0.60	4.43	16.8	4.2	16.6	4.22	16.5	4.63	16.6	4.95	16.4	4.72	16.5
Cr	20.0	3.43	28.6	2.42	25.4	10.6	22.2	3.12	20.2	3.46	24.4	2.75	19.0	3.49	22.4	2.93	21.3	3.13
Co	0	0	0	0	0	0	0	0	8.89	3.36	9.54	2.89	16.4	6.13	17.8	6.28	16.5	6.52
Mo	0.62	0.30	0.89	0.48	5.10	10.2	0.63	0.26	0.59	0.32	0.70	0.34	0.54	0.31	0.53	0.34	0.60	0.28
Ni	72.3	74.2	63.0	70.8	7.50	2.90	69.9	72.5	63.8	70.4	58.6	69.8	57.0	67.5	52.2	65.8	54.0	66.9
Ta	0	0	0	1.98	1.00	1.80	0	0	0	0	0	1.80	0	0	0	1.83	0	0
Ti	0	1.92	0	2.12	0.50	0.30	0	1.92	0	1.94	0	1.96	0	1.95	0	1.93	0	2.01
W	2.49	3.75	1.97	4.84	55.6	73.8	2.72	5.37	2.26	3.94	2.26	3.90	2.21	3.92	1.89	4.53	2.77	4.66

Notes: *Full heat treatment

+Full heat treatment plus 976 hours at 1000°C

TABLE IV

LATTICE PARAMETER MEASUREMENTS

	Full Heat Treatment				Full Heat Treatment Plus 100 hrs. at 1000°C		
Alloy	γ' extracted	γ' in situ	γ in situ	δ in situ	γ' in situ	γ in situ	δ in situ
A	3.5757	3.5754	3.5754	nil	3.5734	3.5734	nil
B-1	3.5838	3.5859	3.5859	nil	3.5803	3.5938	0.0038
B-2	3.5840	3.5845	3.5926	0.0023	3.5793	3.5907	0.0032
C	3.5780	3.5787	3.5787	nil	3.5735	3.5817	0.002?
D	3.5757	3.5752	3.5752	nil	3.5744	3.5744	nil
E	3.5835	3.5842	3.5842	nil	3.5804	3.5804	nil
F	3.5771	3.5772	3.5772	nil	3.5746	3.5746	nil
G	3.5842	3.5843	3.5843	nil	3.5818	3.5818	nil
H	3.5792	——	——	nil	3.5780	3.5780	nil

TABLE V

CREEP-RUPTURE EXPONENTS

Alloy	$\dot{\varepsilon}_s = A_1\sigma^n$	$t_f = A_2\sigma^{-p}$	$t_t = A_3\sigma^{-l}$	$\dot{\varepsilon}_s = A_4 t_f^{-m}$
	n	p	l	m
A	8.37 ± 2.94*	6.24 ± 1.74	7.34 ± 2.66	1.34 ± 0.36
B	8.04 ± 0.93	5.87 ± 0.33	6.84 ± 0.46	1.39 ± 0.12
C	10.6 ± 1.33	7.21 ± 0.65	8.15 ± 0.59	1.47 ± 0.14
D	8.27 ± 0.69	6.03 ± 0.76	7.37 ± 1.12	1.37 ± 0.27
E	7.91 ± 2.45	5.15 ± 1.68	6.35 ± 1.76	1.50 ± 0.42
F	7.51 ± 0.90	5.66 ± 0.59	5.83 ± 1.72	1.32 ± 0.24
G	6.42 ± 1.15	5.18 ± 1.03	5.68 ± 1.37	1.22 ± 0.43
H	9.46 ± 1.62	6.77 ± 0.45	7.82 ± 0.54	1.40 ± 0.17
B (925^oC)	7.21 ± 2.09	5.13 ± 1.21	6.16 ± 3.7	1.37 ± 0.22

Note: * 95% Confidence intervals

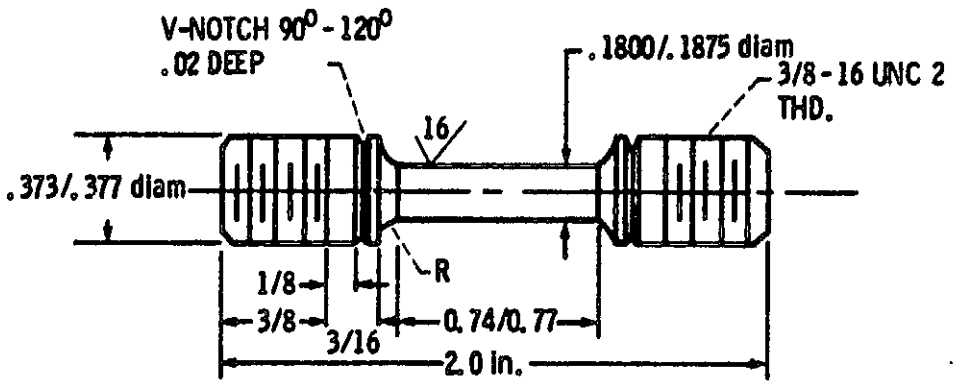

Figure 1. Specimen design for tensile and creep-rupture tests.

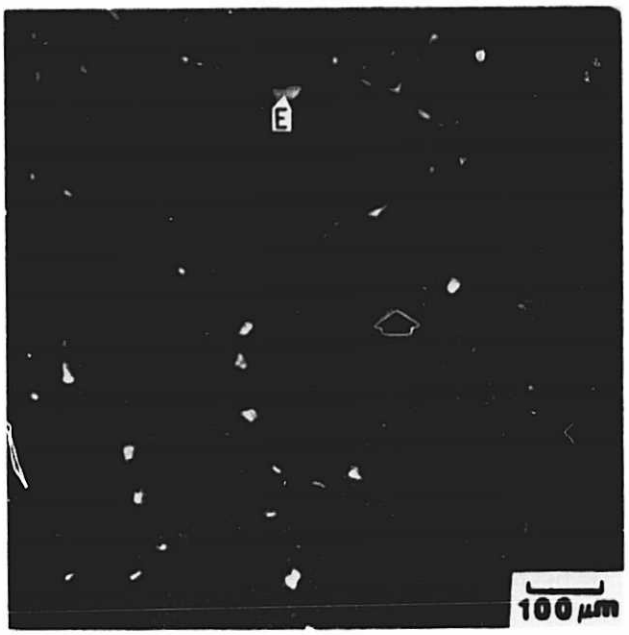

(a)

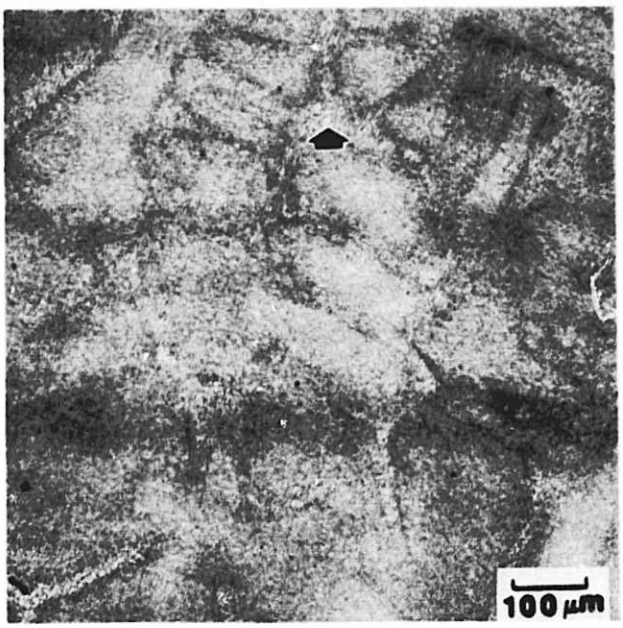

(b)

Figure 2. As cast microstructure of single crystal alloys showing dendritic morphology. Note coarse γ'(arrows) and γ' eutectic pools(E) in interdendritic regions. (a) Alloy B, (b) Alloy H.

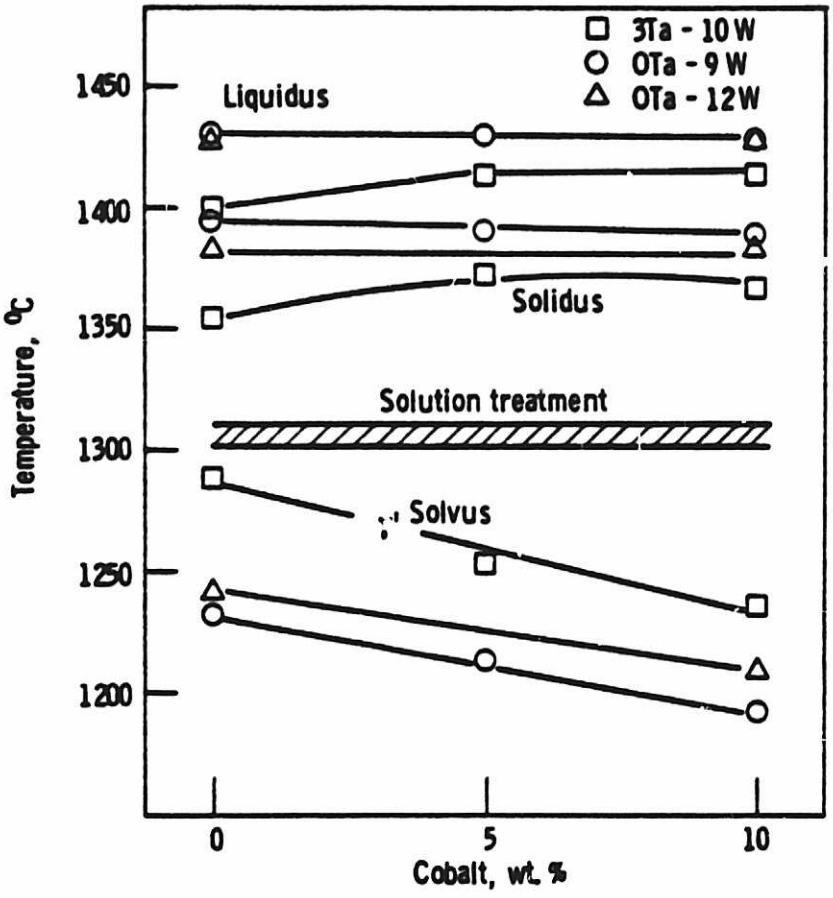

Figure 3. Results of differential thermal analysis exhibiting the transformation temperatures and heat treatment range for the single crystal alloys.

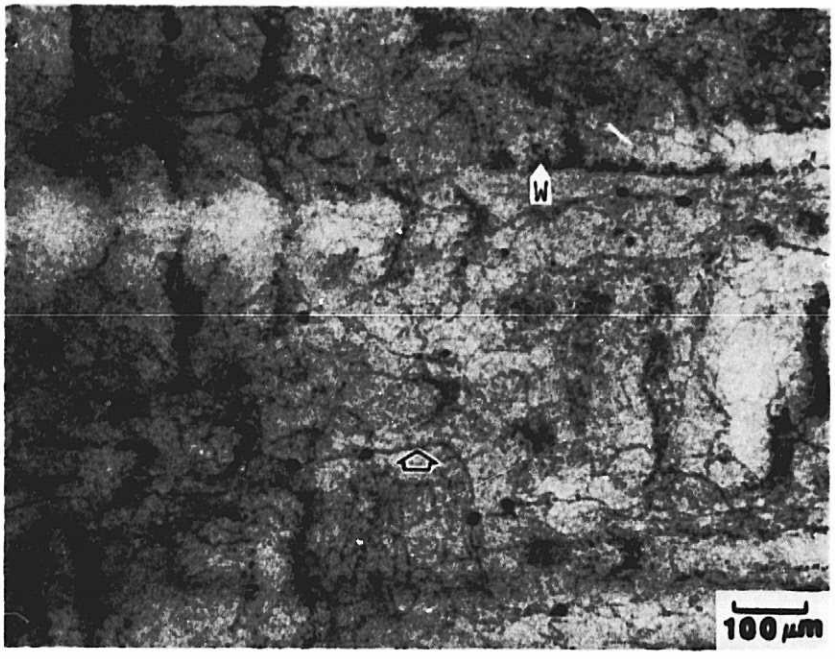

Figure 4. Optical micrograph of heat treated Alloy B. Note the presence of micropores and subgrain boundaries(arrow). The fine precipitates decorating the dendrite cores are α-W particles(W).

Figure 5. Optical photomicrograph of a sample of Alloy B showing incipient melting.

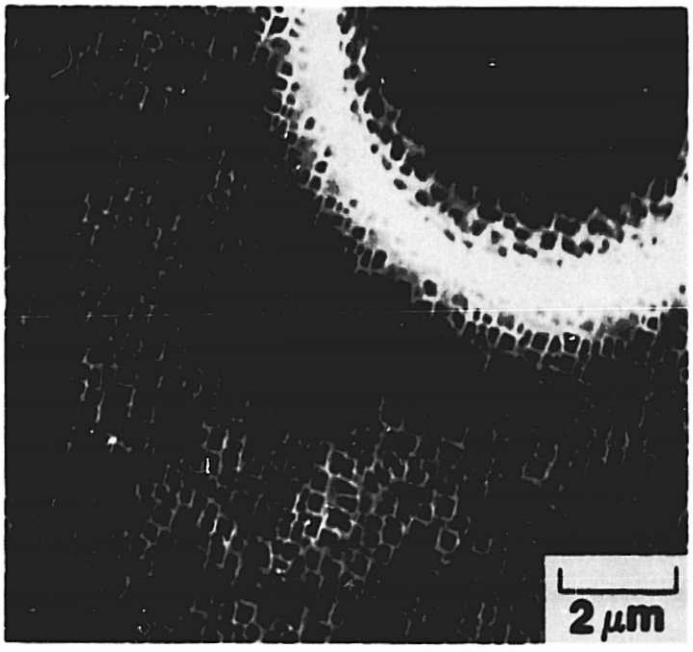

Figure 6. Scanning electron micrograph of heat treated Alloy B showing the γ' particle morphology in and around a micropore.

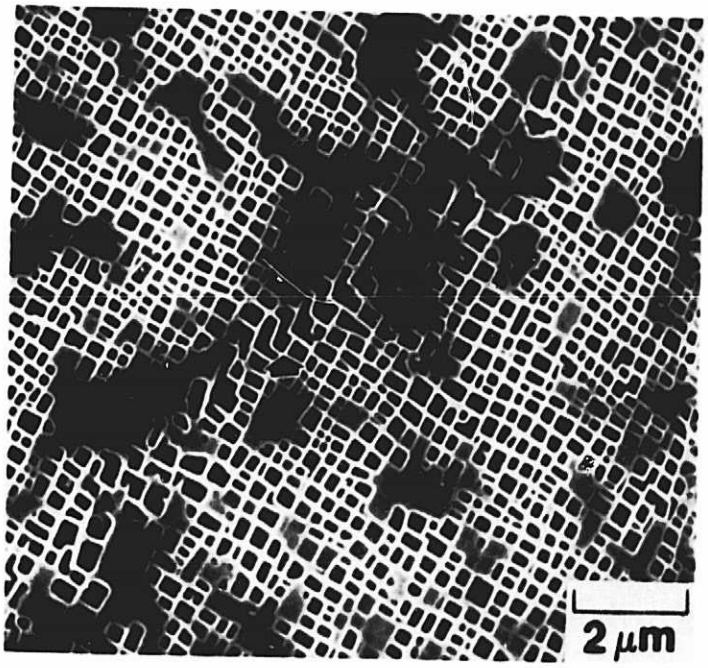

Figure 7. Scanning electron micrograph of heat treated Alloy B showing γ' particle morphology along a subgrain boundary(arrow).

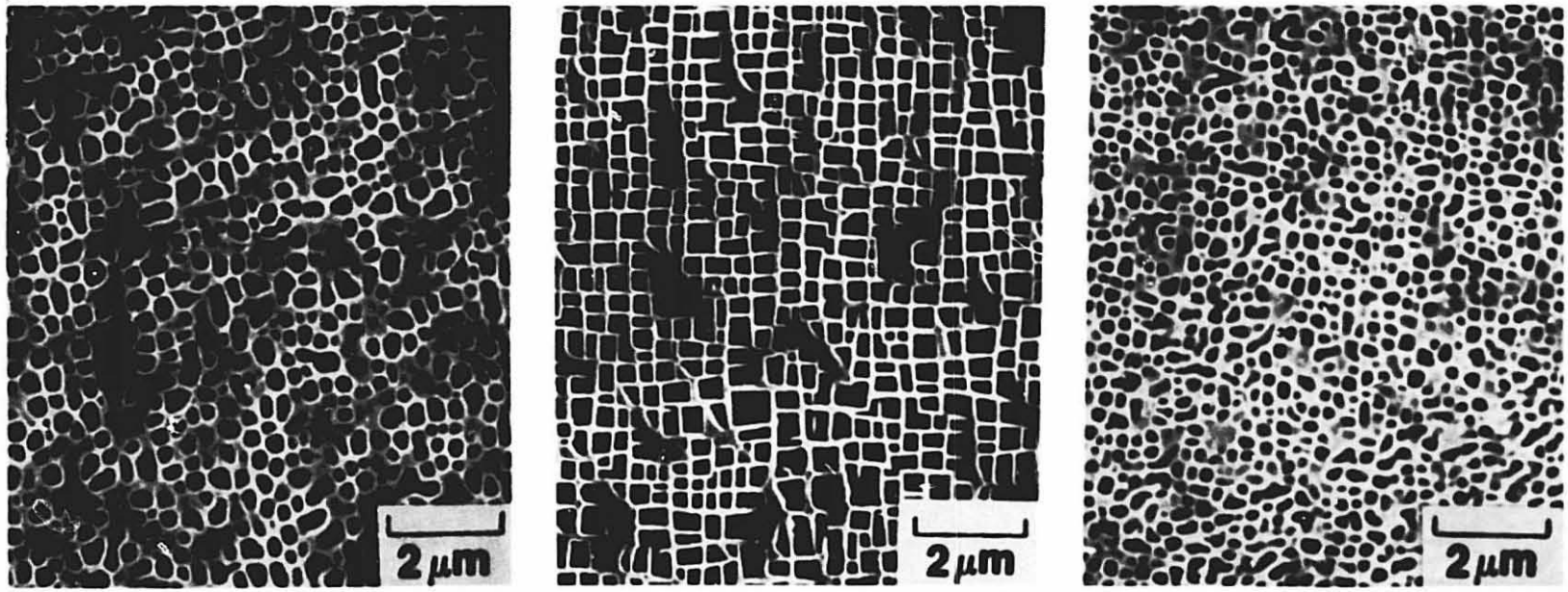

(a) (b) (c)

Figure 8. Scanning electron micrographs of fully heat treated single crystal alloys. Cubic and spherical γ' morphologies are illustrated. (a) Alloy A, (b) Alloy B, (c) Alloy G.

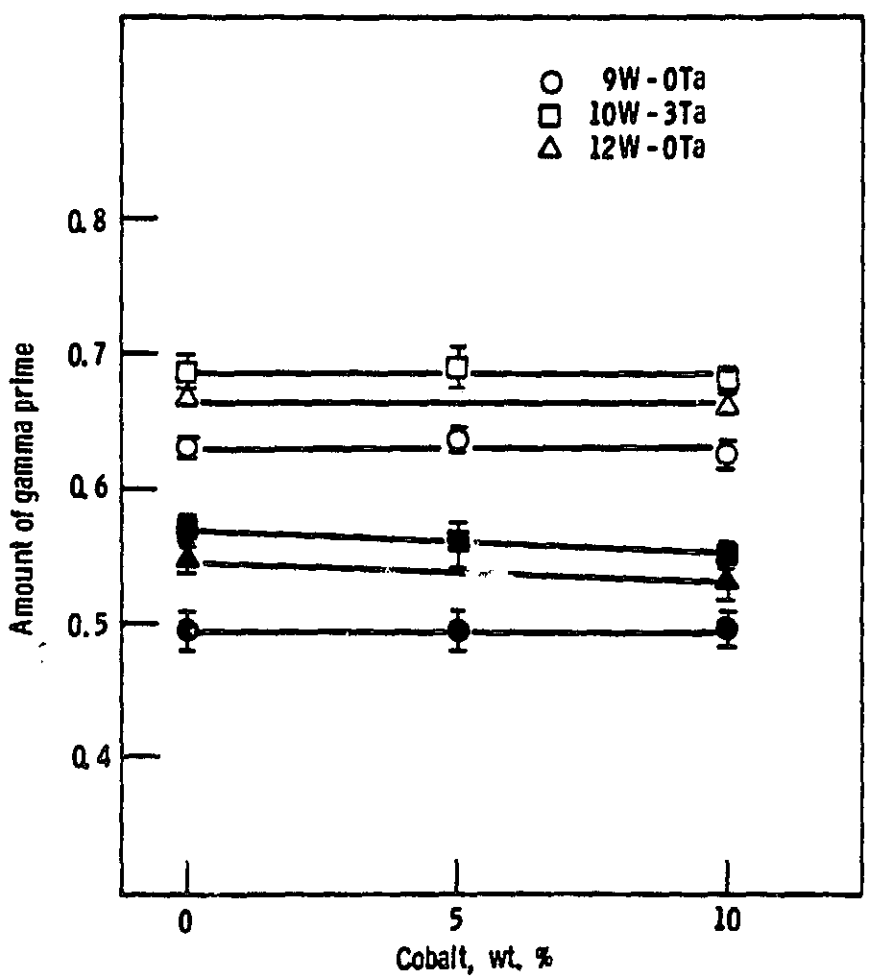

Figure 9. The amount of γ' phase in the single crystal alloys. Open symbols correspond to phase extraction results on heat treated samples. Closed symbols correspond to quantitative metallographic results on failed creep rupture specimens.

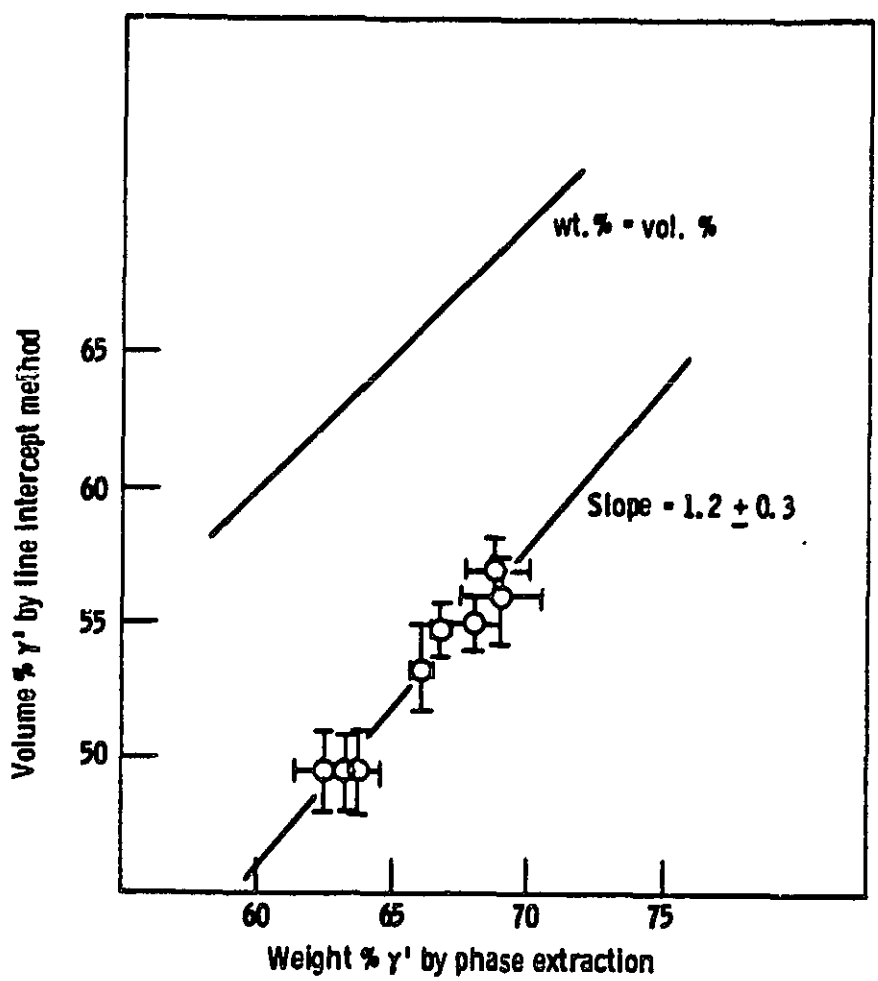

Figure 10. Comparison of the percentage of γ' phase measured by two techniques.

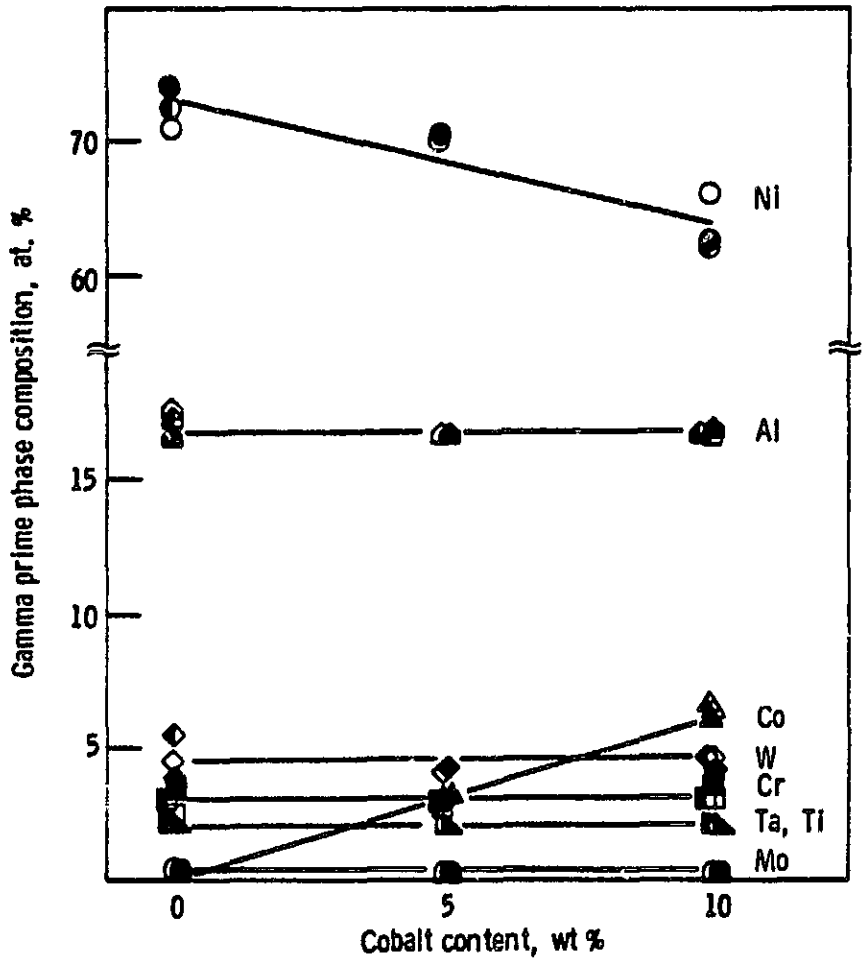

Figure 11. Composition of the γ' phases of the single crystal alloys. Open, filled, and half-filled symbols correspond to 3Ta-10W, 0Ta-9W, and 0Ta-12W alloys, respectively.

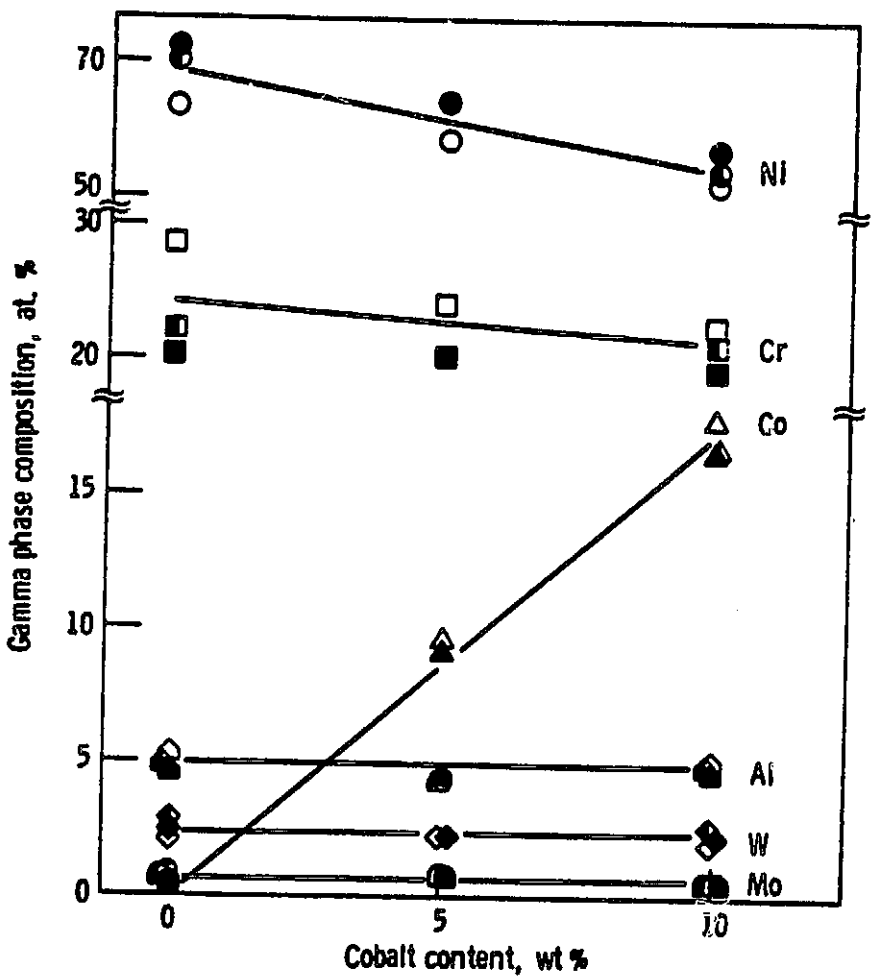

Figure 12. Composition of the γ phases of the single crystal alloys. Open, filled, and half-filled symbols correspond to 3Ta-10W, 0Ta-9W, and 0Ta-12W alloys, respectively.

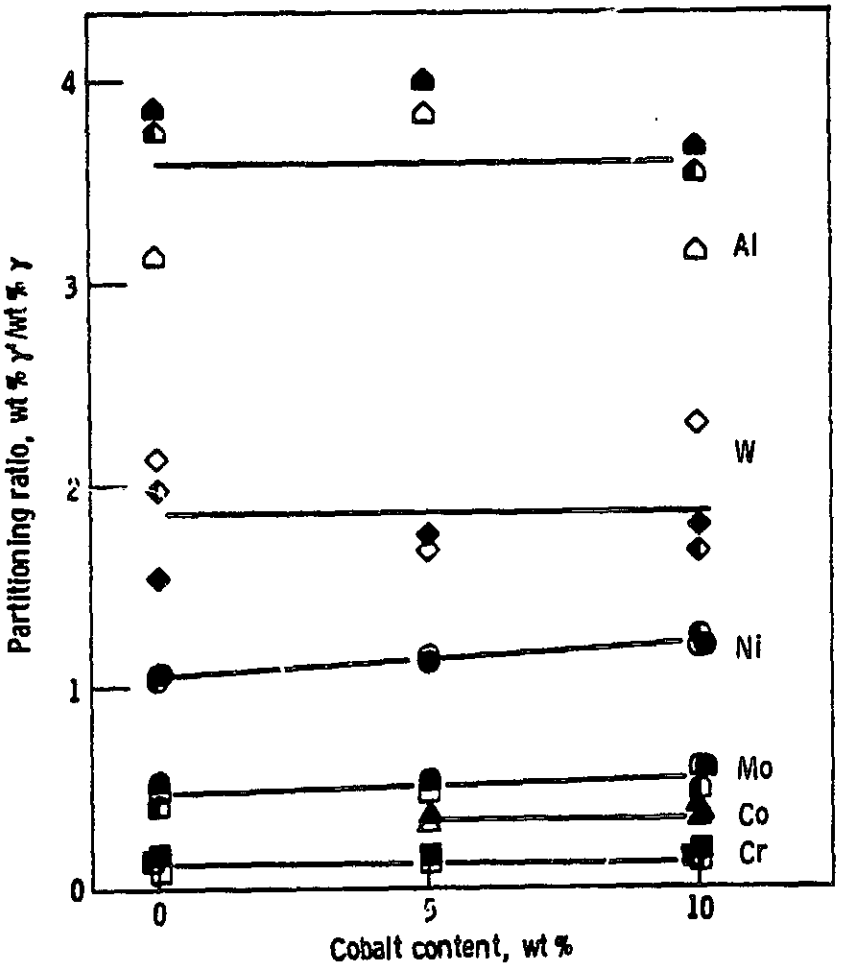

Figure 13. Partitioning of elements between γ and γ' in the single crystal alloys. Open, filled, and half-filled symbols correspond to 3Ta-10W, 0Ta-9W, and 0Ta-12W alloys, respectively.

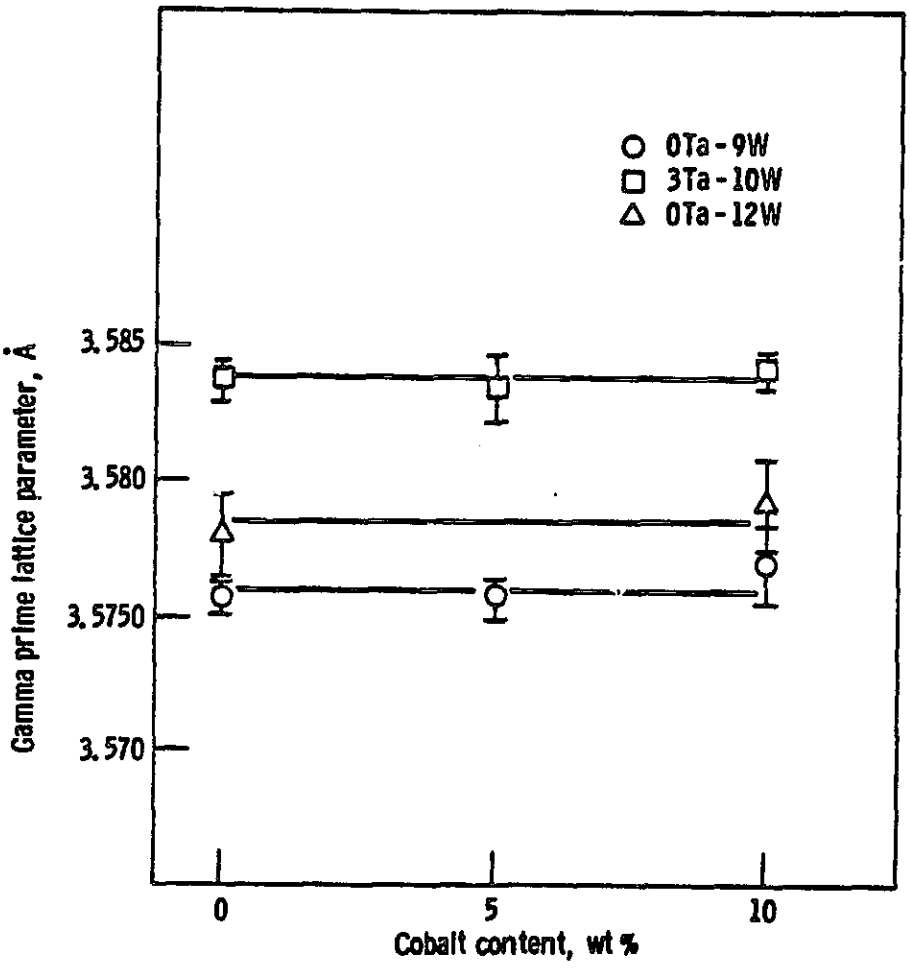

Figure 14. Lattice parameters of extracted γ' particles in the the single crystal alloys.

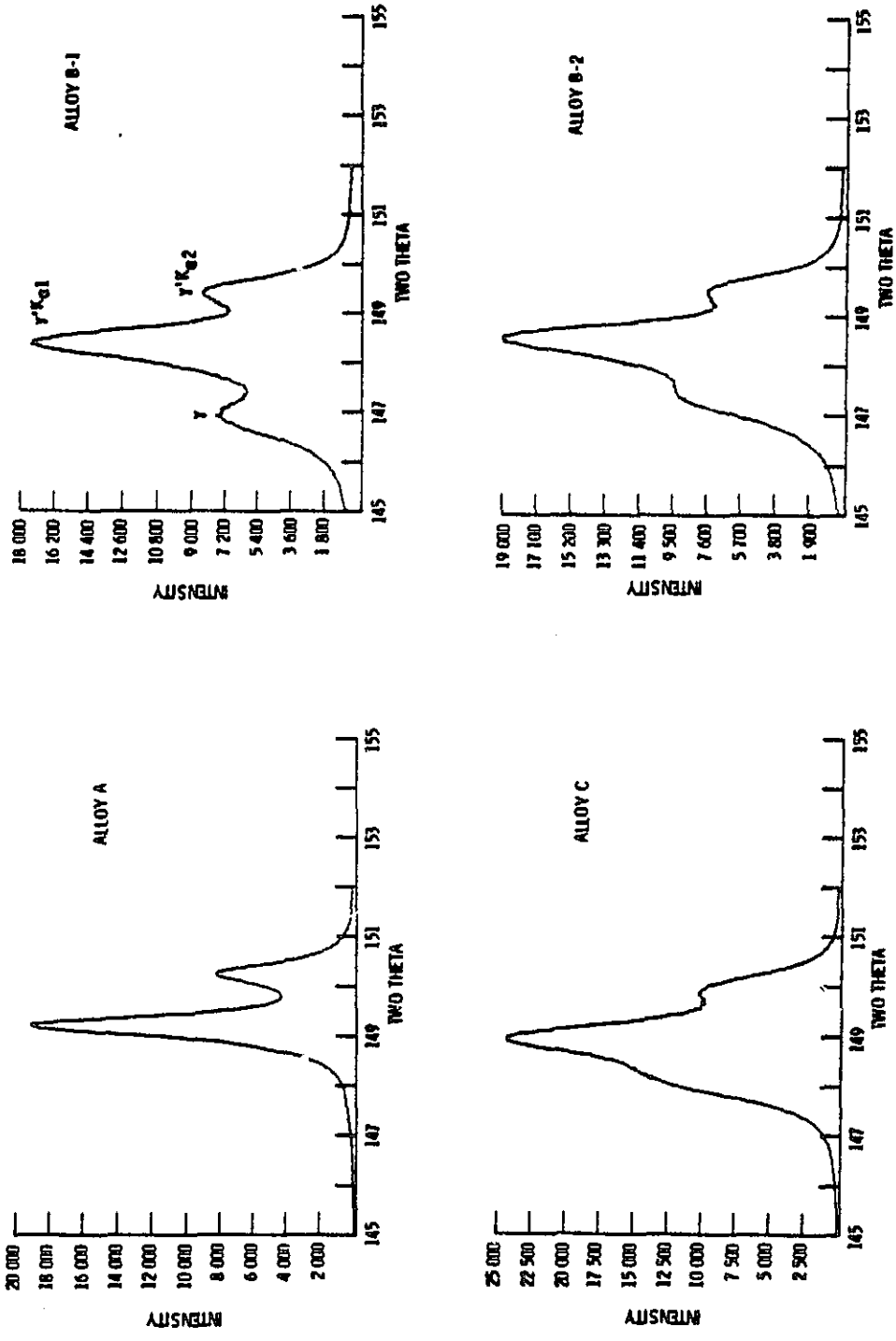

Figure 15. Diffractometer scans of the (420) peaks from bulk samples of single crystal alloys.

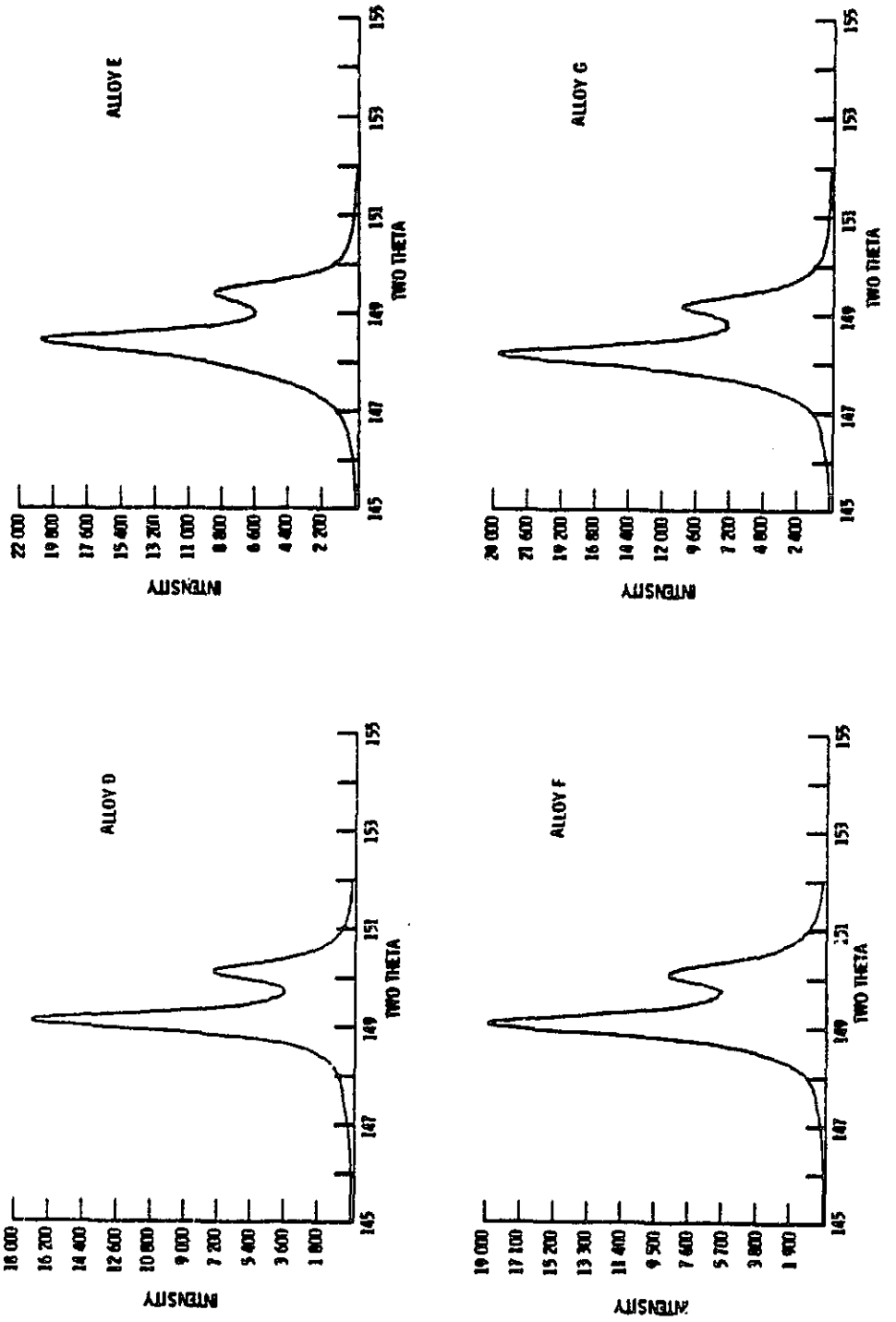

Figure 15. continued

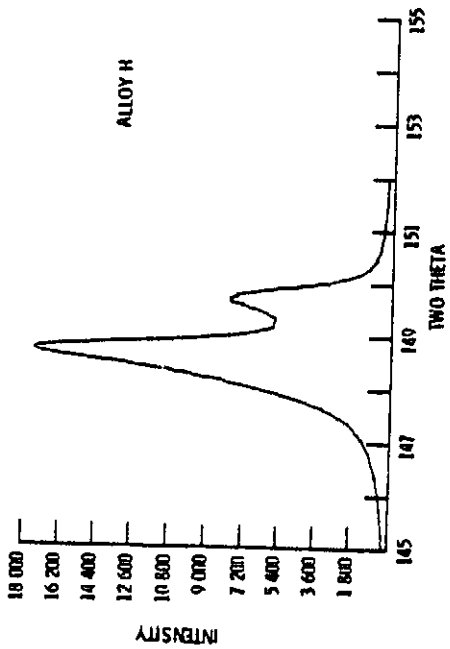

Figure 15. concluded

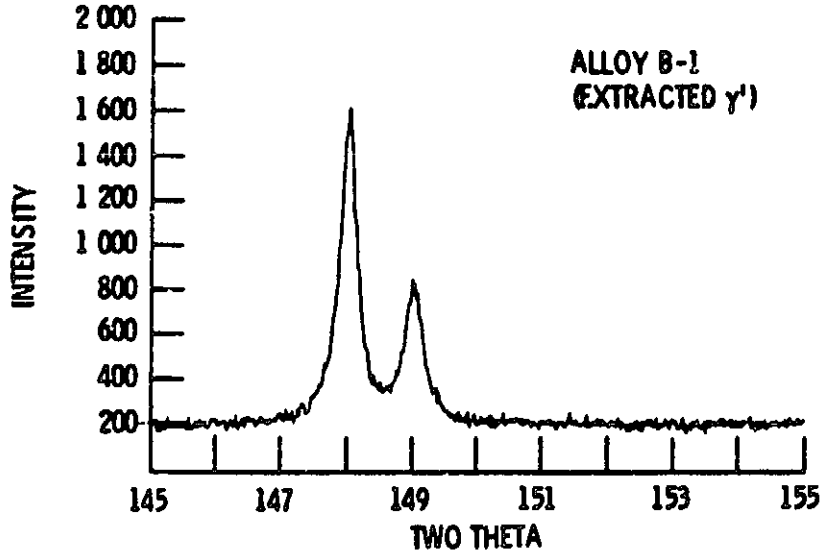

Figure 16. Diffractometer scan of the (420) peak of the extracted γ' of Alloy B. Note the good resolution of the $K\alpha_1/K\alpha_2$ doublet.

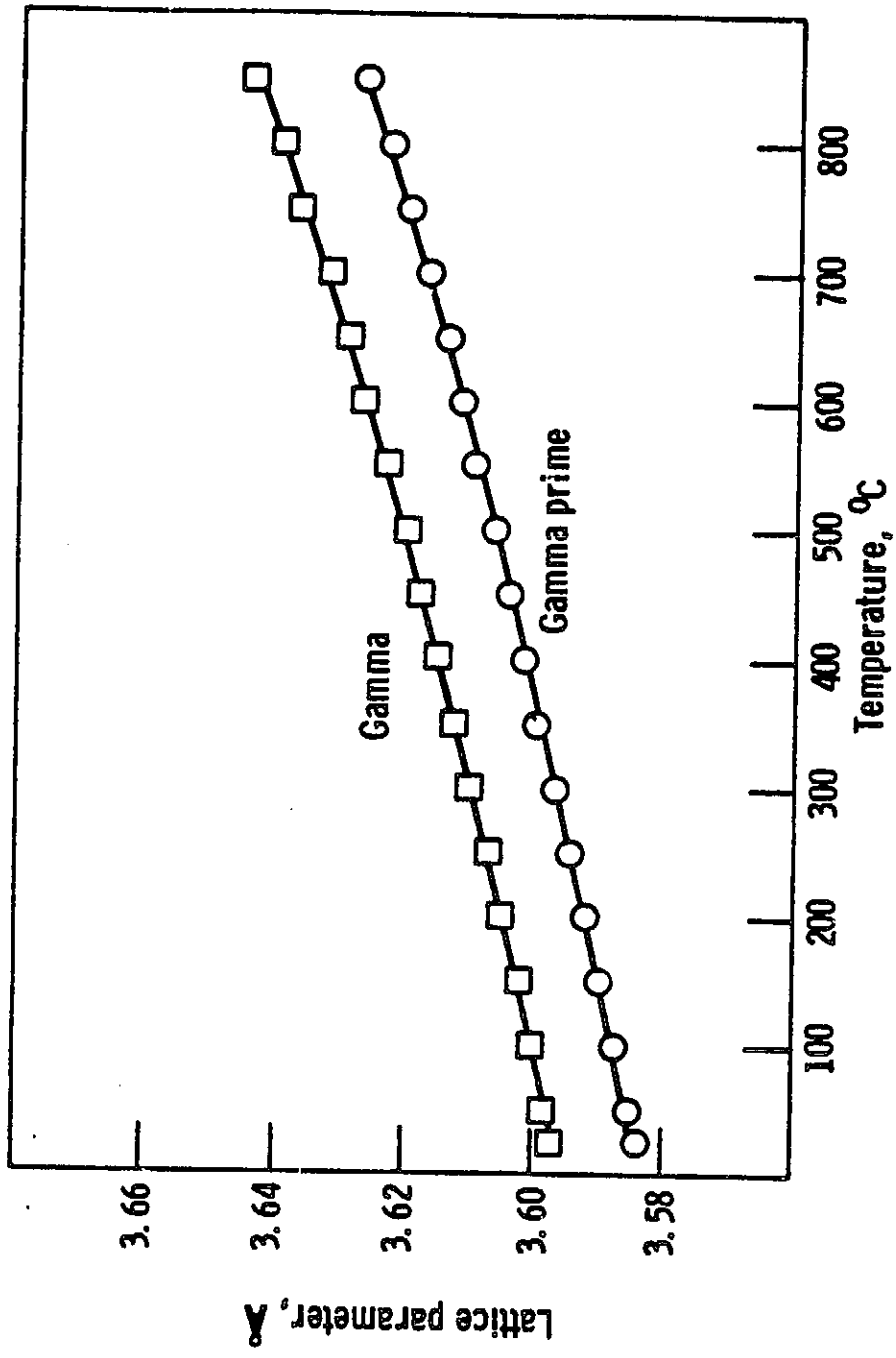

Figure 17. Temperature dependence of γ and γ' lattice parameters for Alloy B.

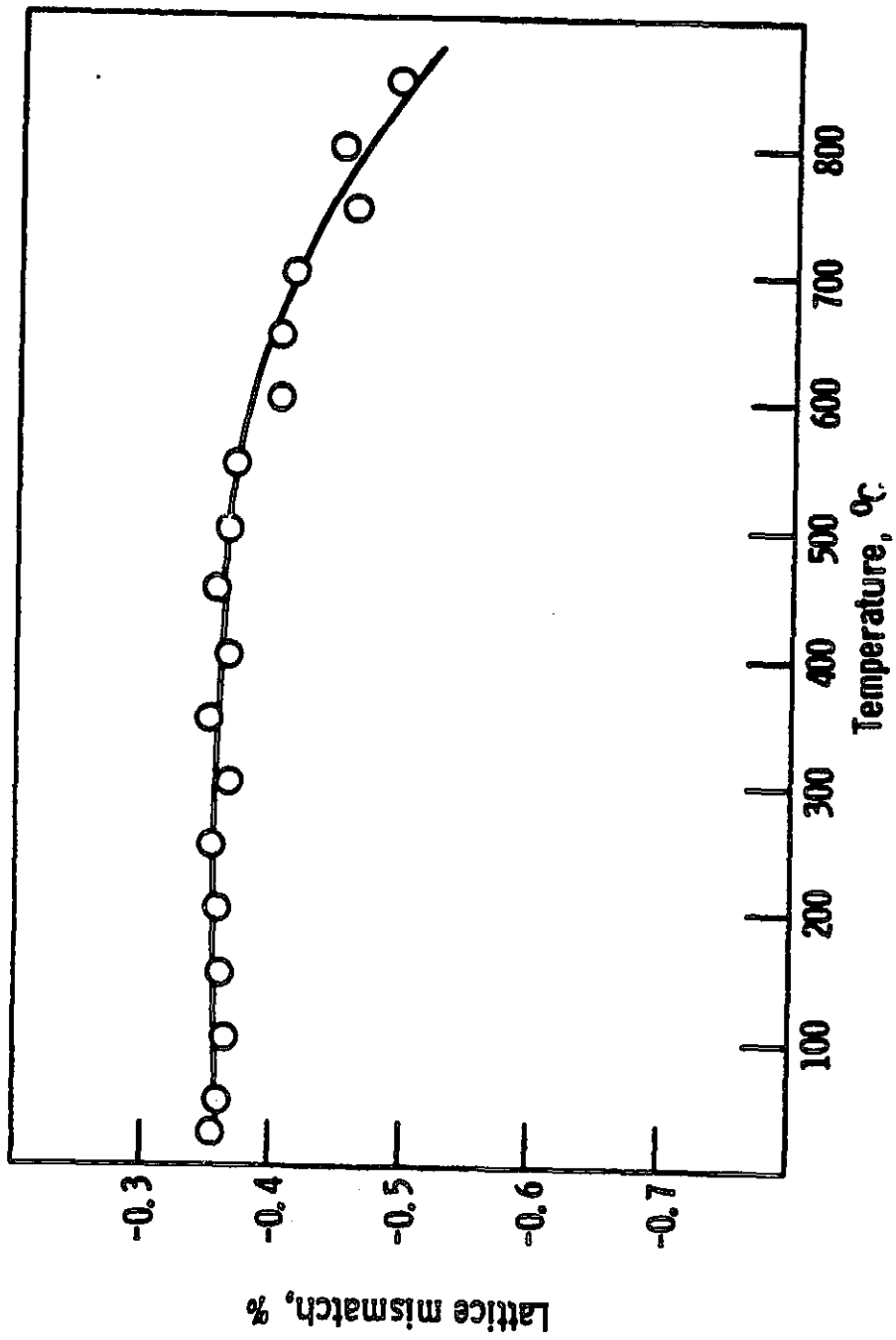

Figure 18. Temperature dependence of the γ-γ' lattice mismatch for Alloy B.

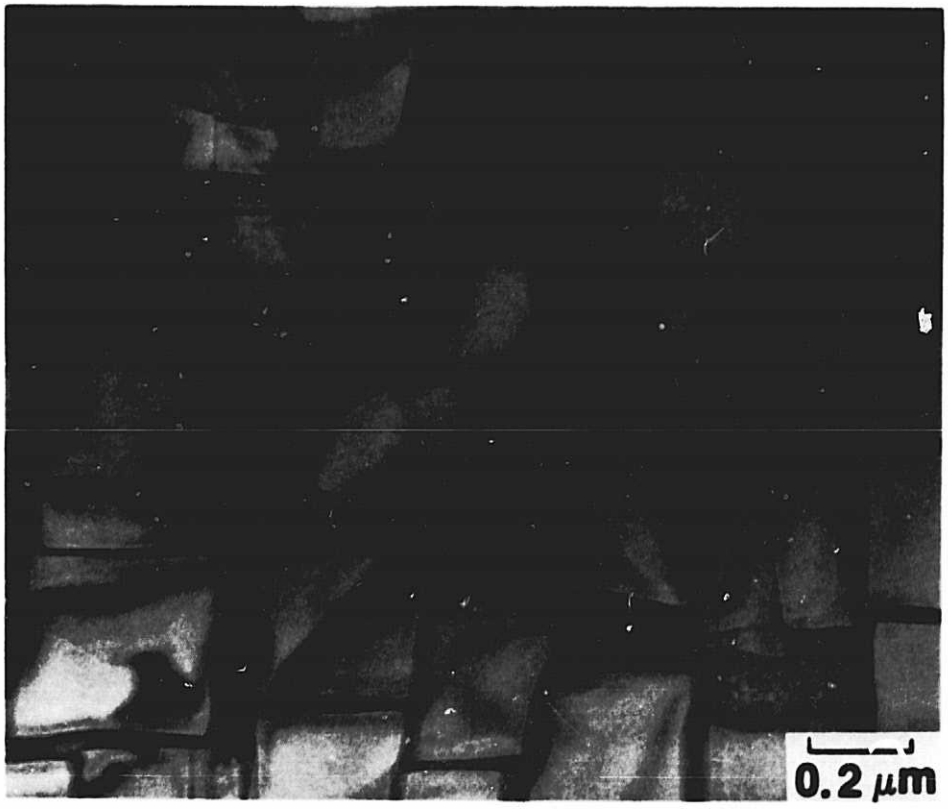

Figure 19. Transmission electron micrograph of heat treated Alloy B showing fully coherent γ' precipitates.

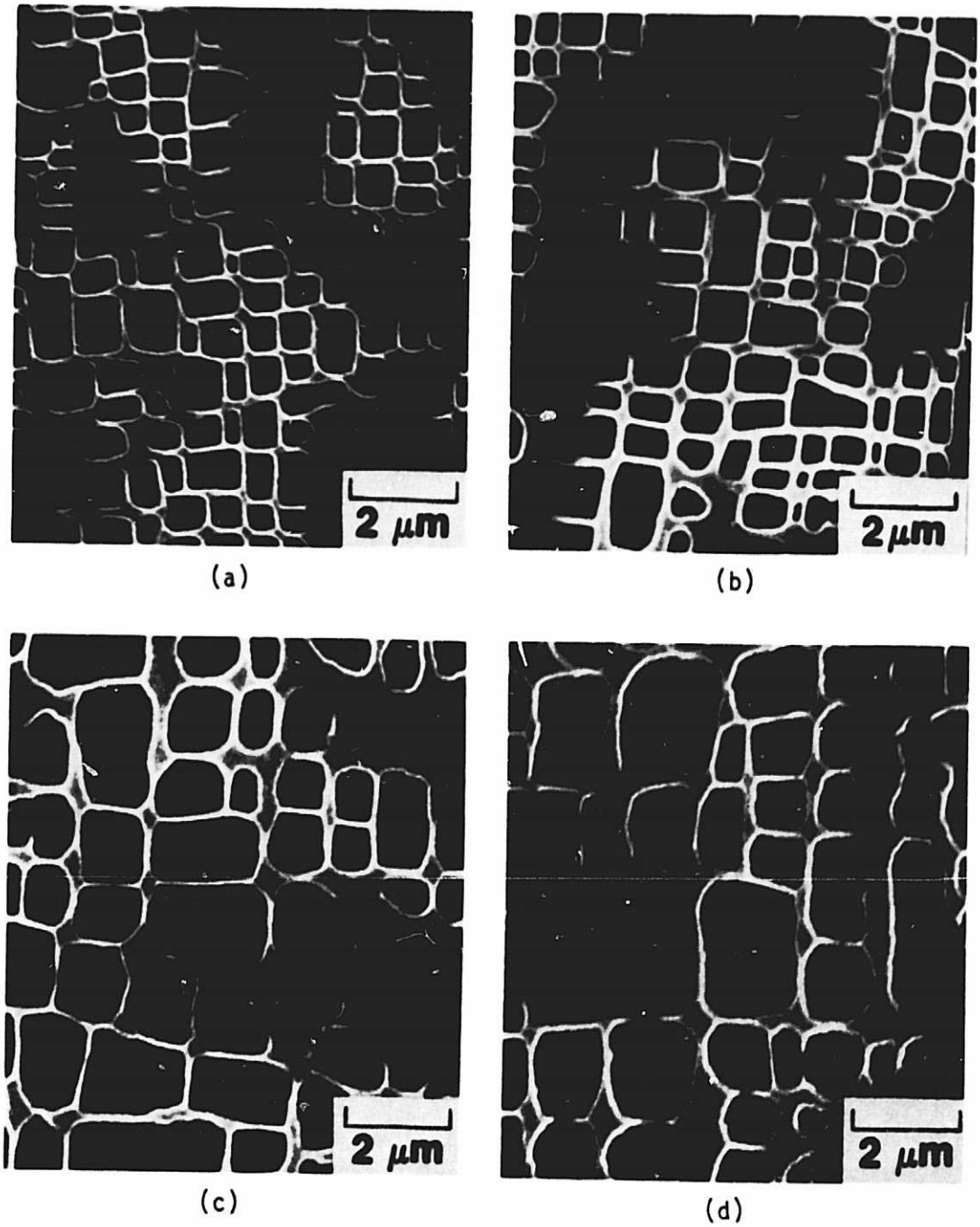

Figure 20. Scanning electron micrographs of Alloy A after aging at 1000°C for various times. (a) 95.3 hours, (b) 215.4 hours, (c) 479.4 hours, (d) 976.0 hours.

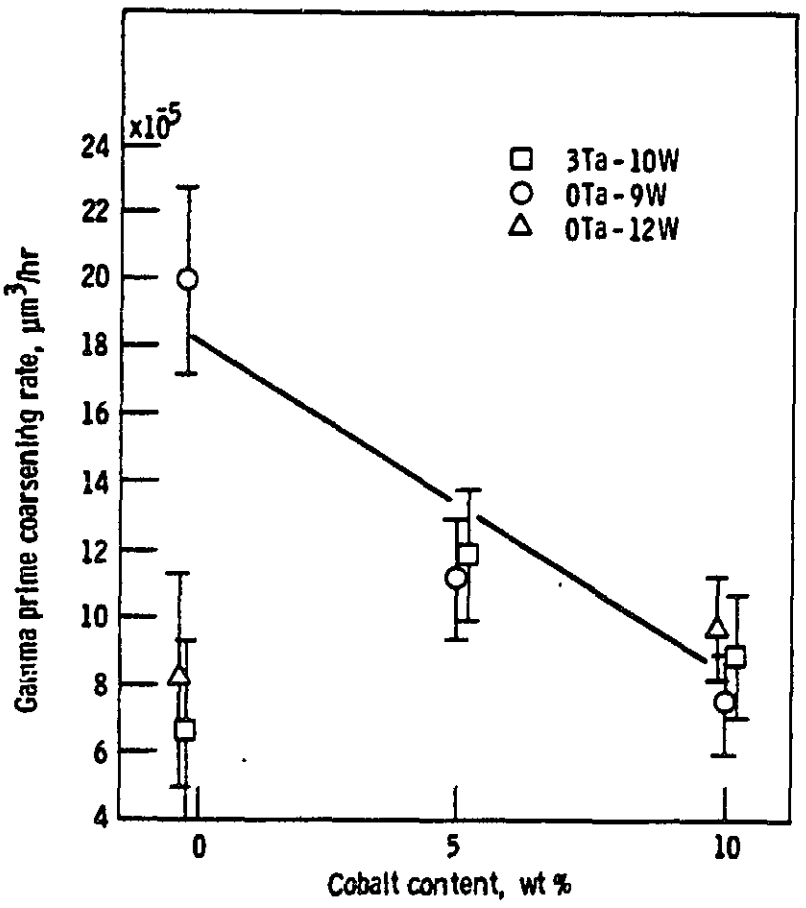

Figure 21. Gamma prime coarsening rate, k, for the single crystal alloys at 1000°C.

Figure 22. Transmission electron micrograph of Alloy B aged for 976 hours at 1000°C. Note the irregular γ' shape, extensive dislocation networks, and α-W precipitates.

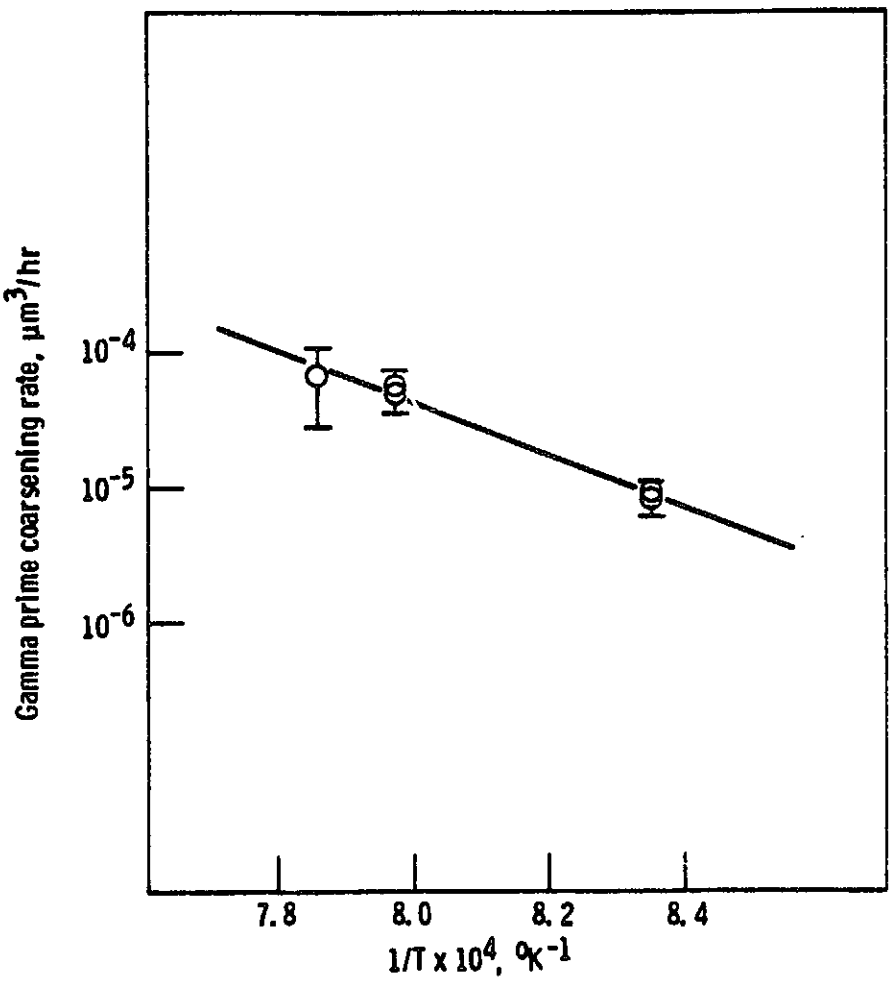

Figure 23. Temperature dependence of the γ' coarsening rate for Alloy B.

Figure 24. Optical micrograph of Alloy B aged for 976 hours at 1000°C depicting W-rich precipitates α-W and µ.

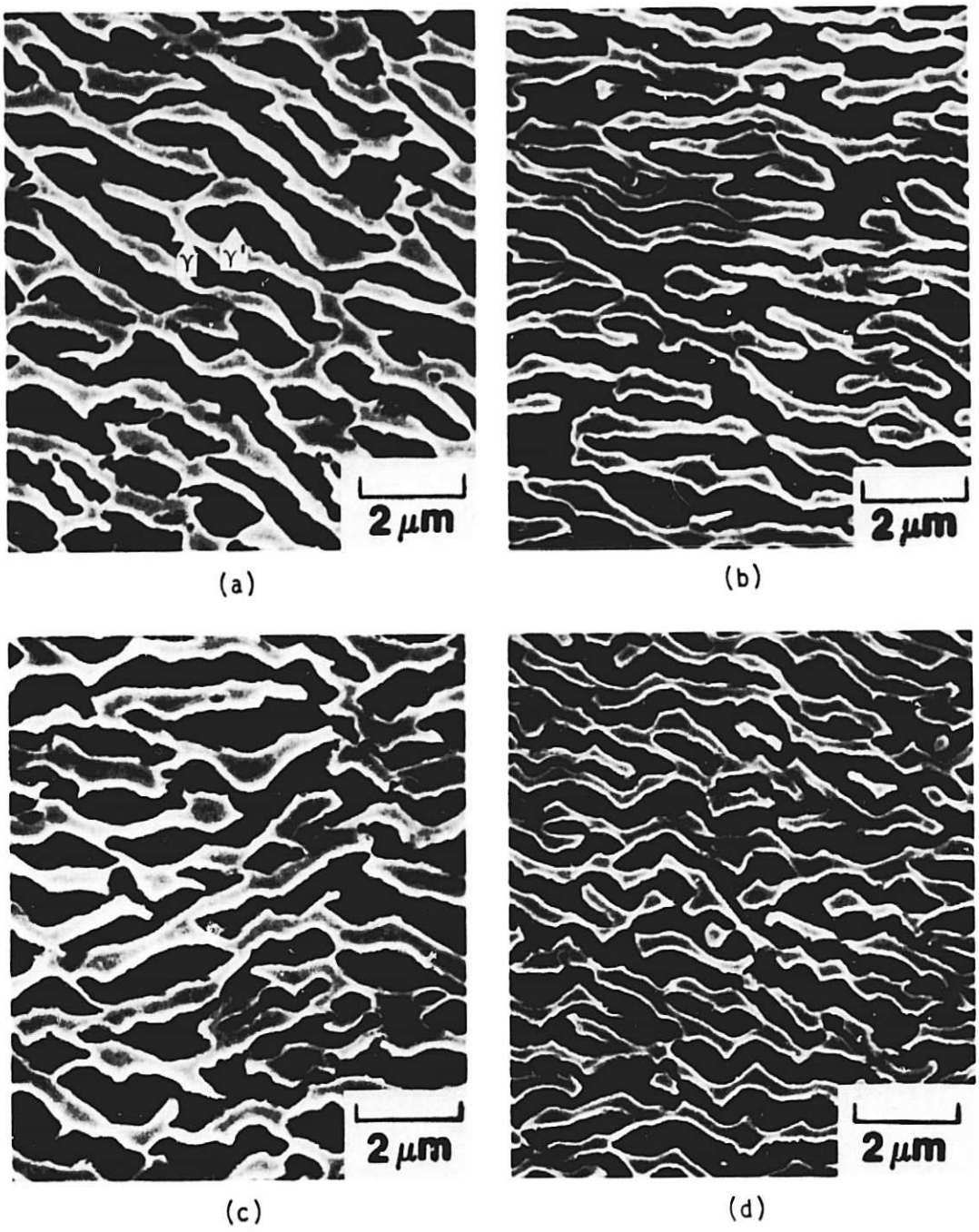

Figure 25. Scanning electron micrographs of longitudinal sections of failed creep-rupture specimens. (a) Alloy A, (b) Alloy C, (c) Alloy D, (d) Alloy E, (e) Alloy F, (f) Alloy G, (g) Alloy H. Stress axis is vertical in all photos.

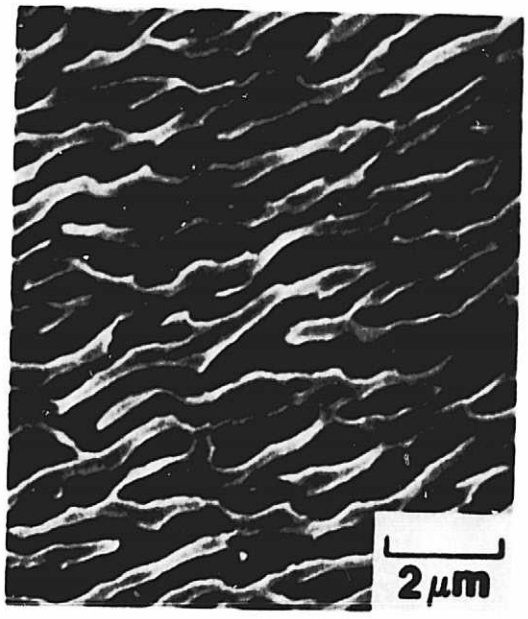

(e)

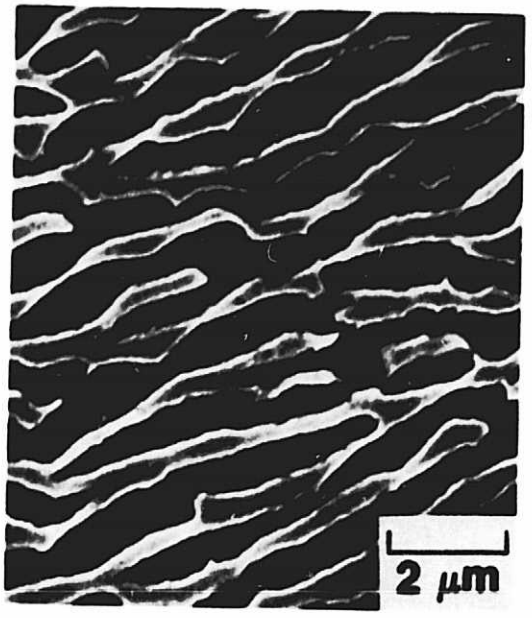

(f)

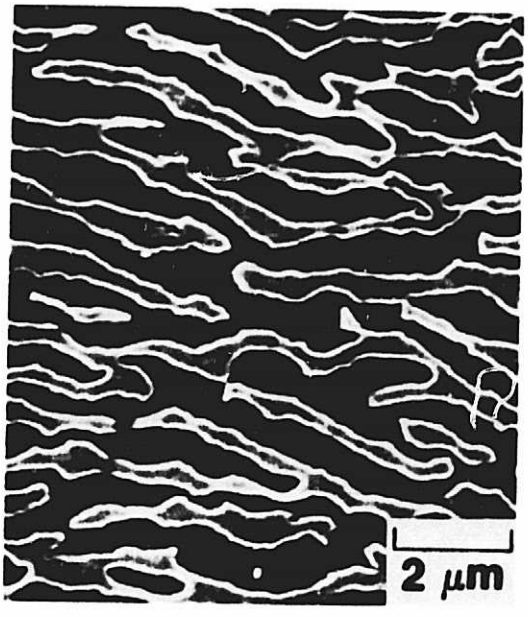

(g)

Figure 25. concluded

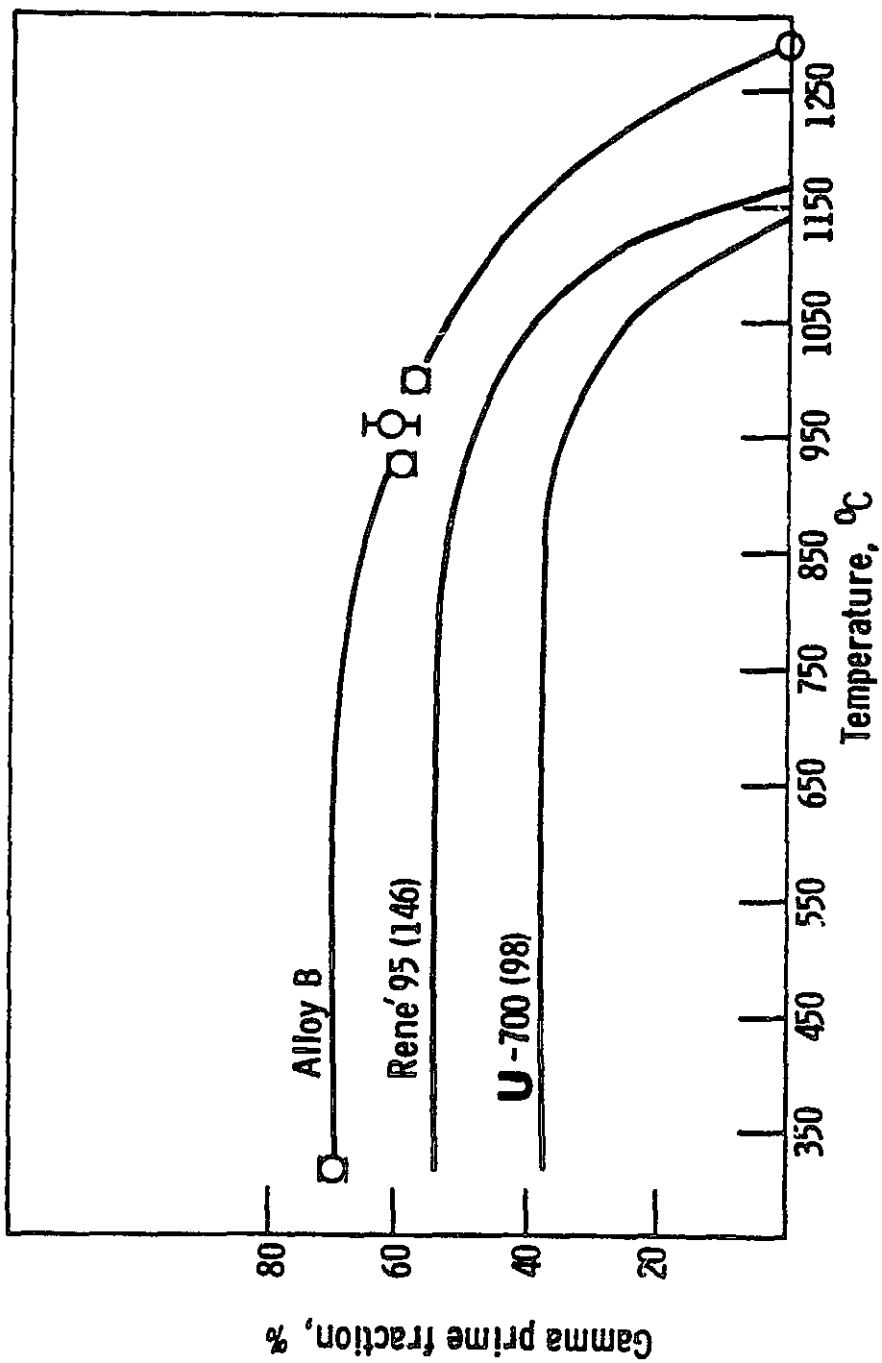

Figure 26. Temperature dependence of γ' volume fraction for Alloy B.

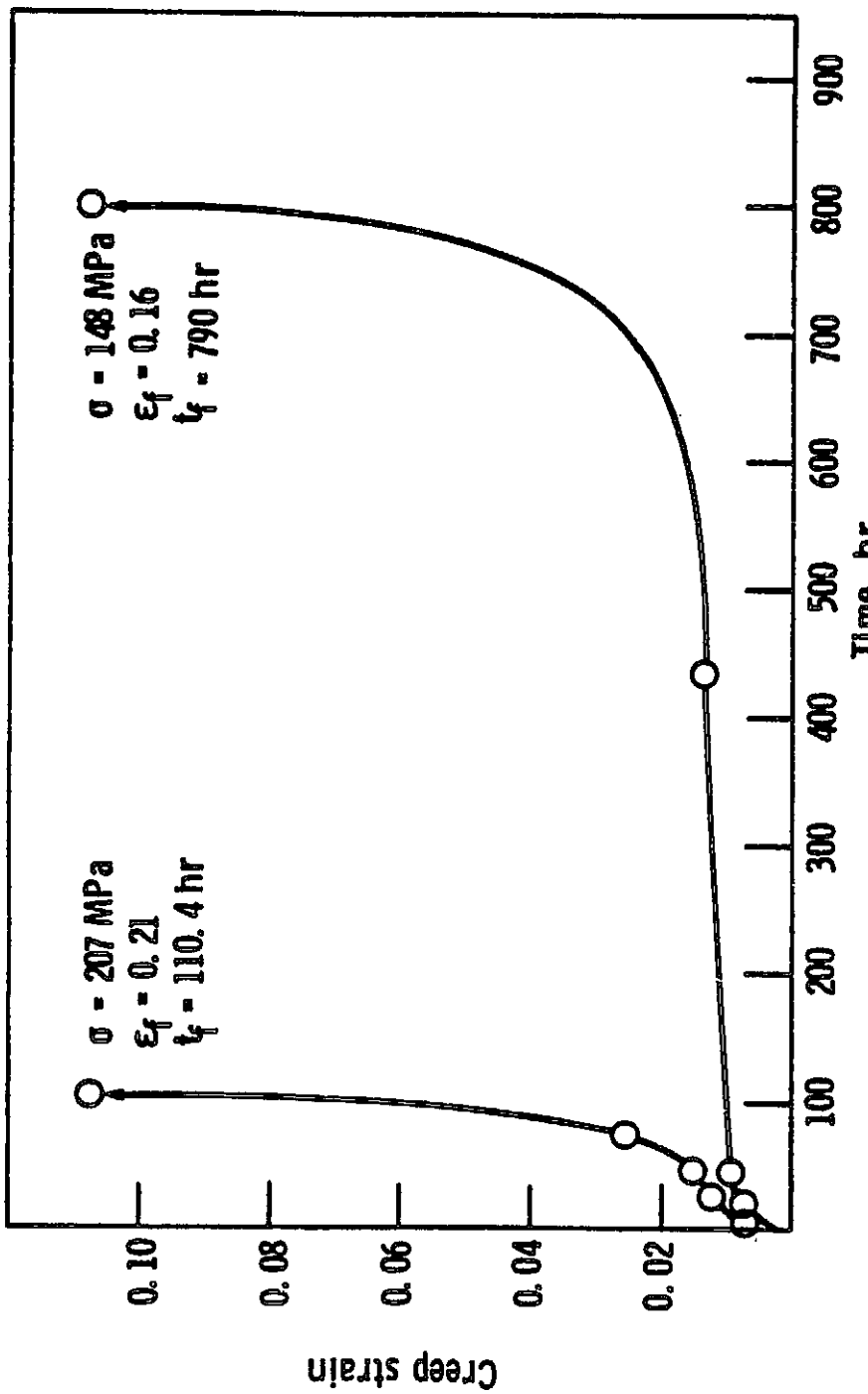

Figure 27. Typical creep curves for Alloy B at 1000°C. Open symbols correspond to times at which microstructures were evaluated and presented in Figures 28 and 30.

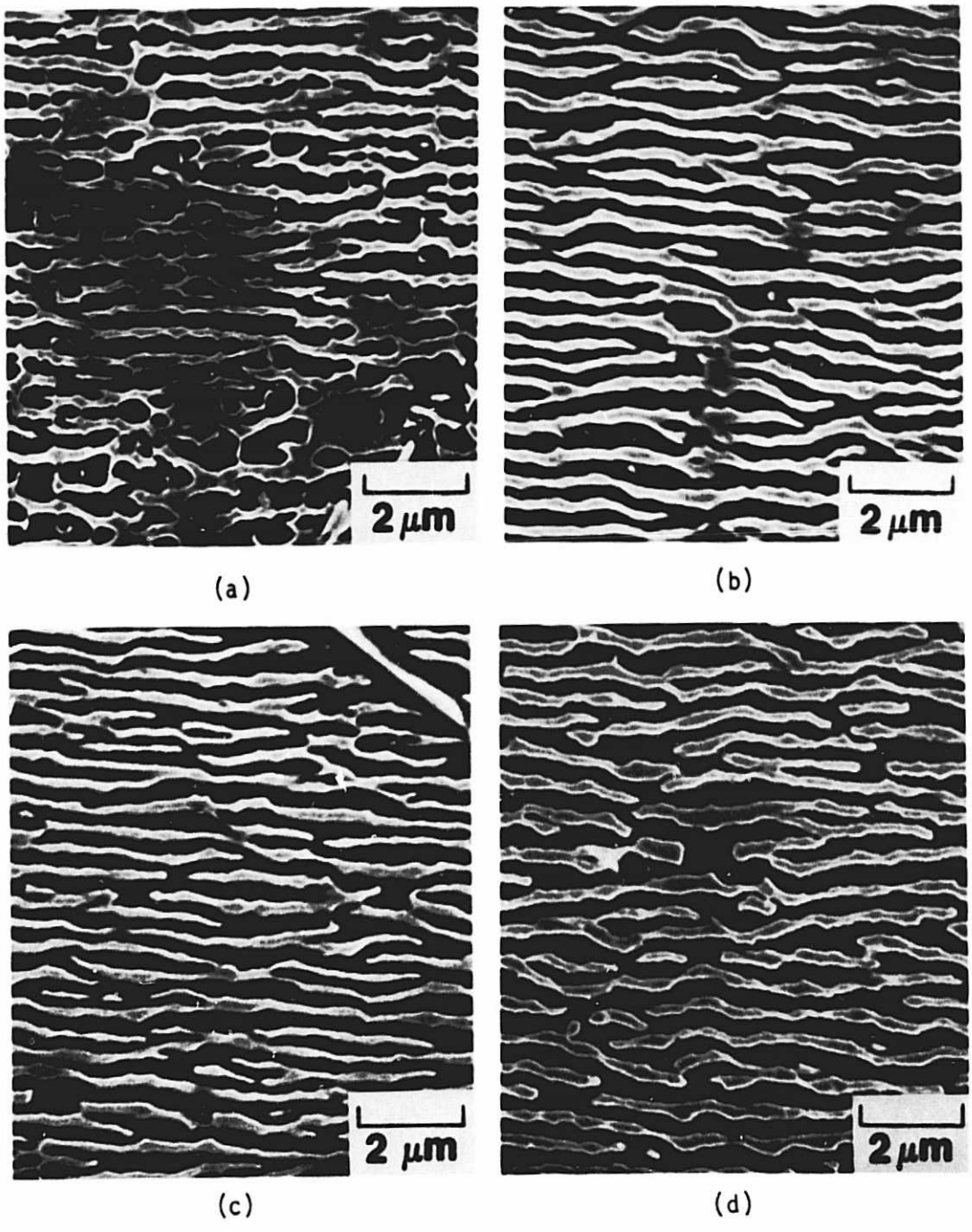

Figure 28. Longitudinal microstructures of samples creep tested at 1000°C and 207 MPa for (a) 5 hours, (b) 24.55 hours, (c) 46.6 hours, (d) 75.5 hours, (e) 110.4 hours. Stress axis is vertical in all photos.

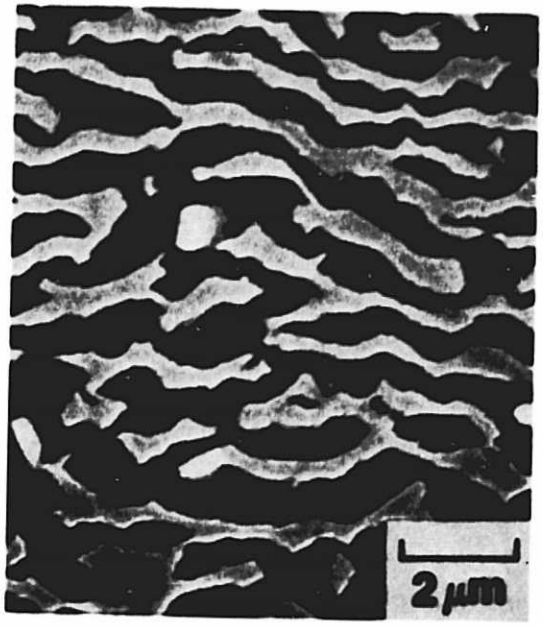

(e)

Figure 28. concluded

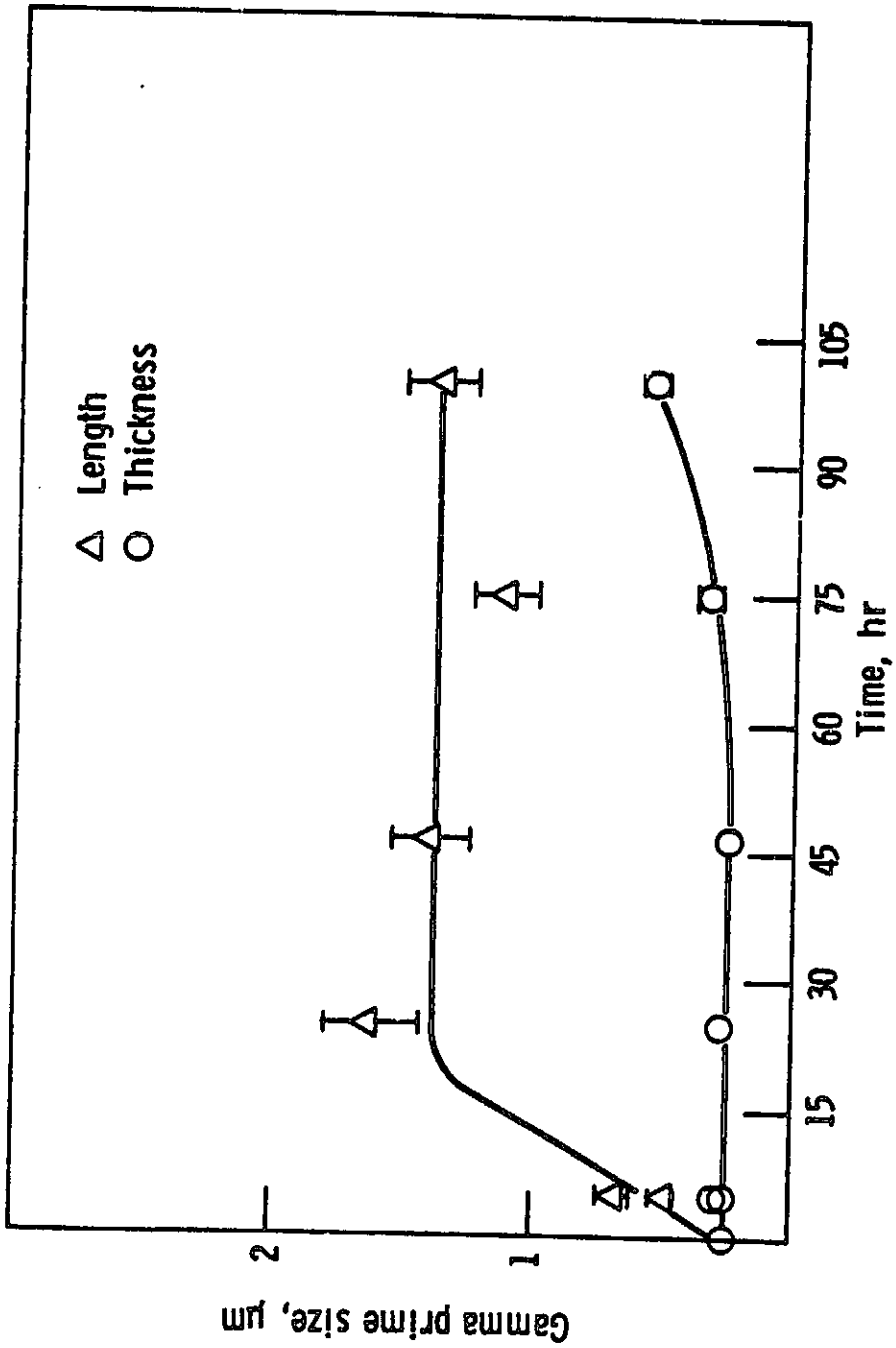

Figure 29. Gamma prime dimensions as a function of creep exposure at 1000°C and 207 MPa.

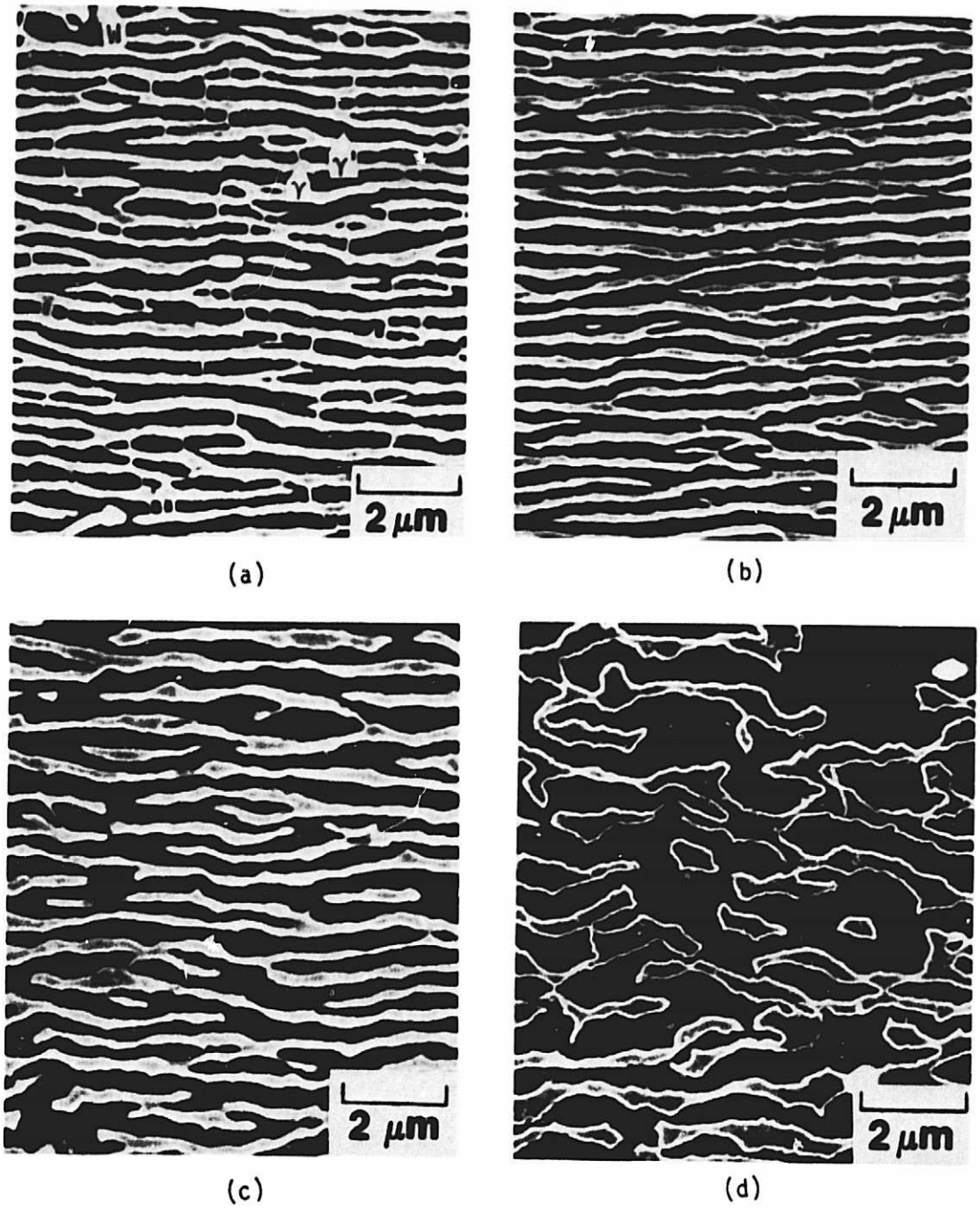

Figure 30. Longitudinal microstructures of samples creep tested at 1000°C and 148 MPa for (a) 20 hours, (b) 45.8 hours, (c) 434.5 hours, (d) 790 hours.

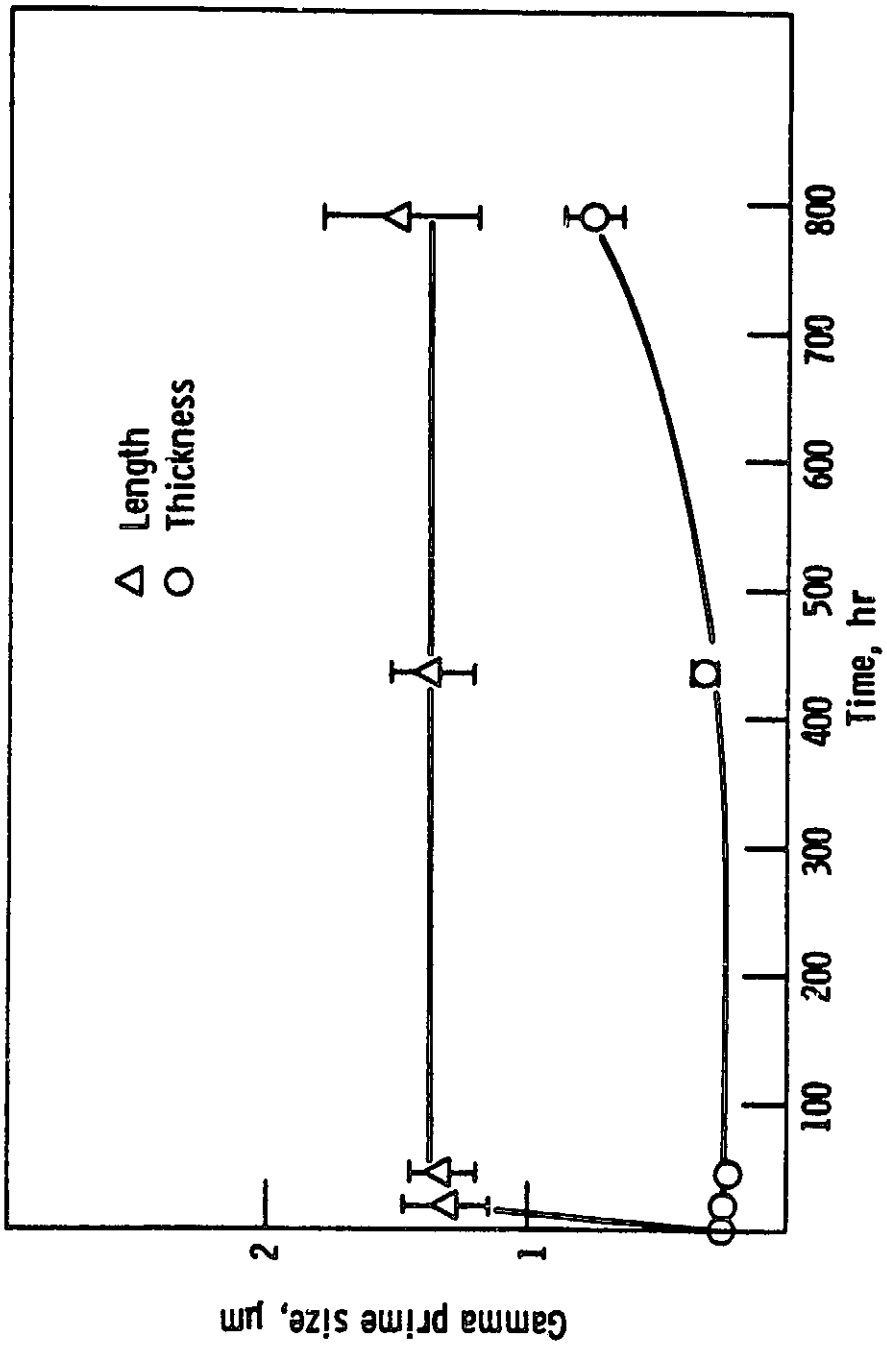

Figure 31. Gamma prime dimensions as a function of creep exposure at 1000°C and 148 MPa.

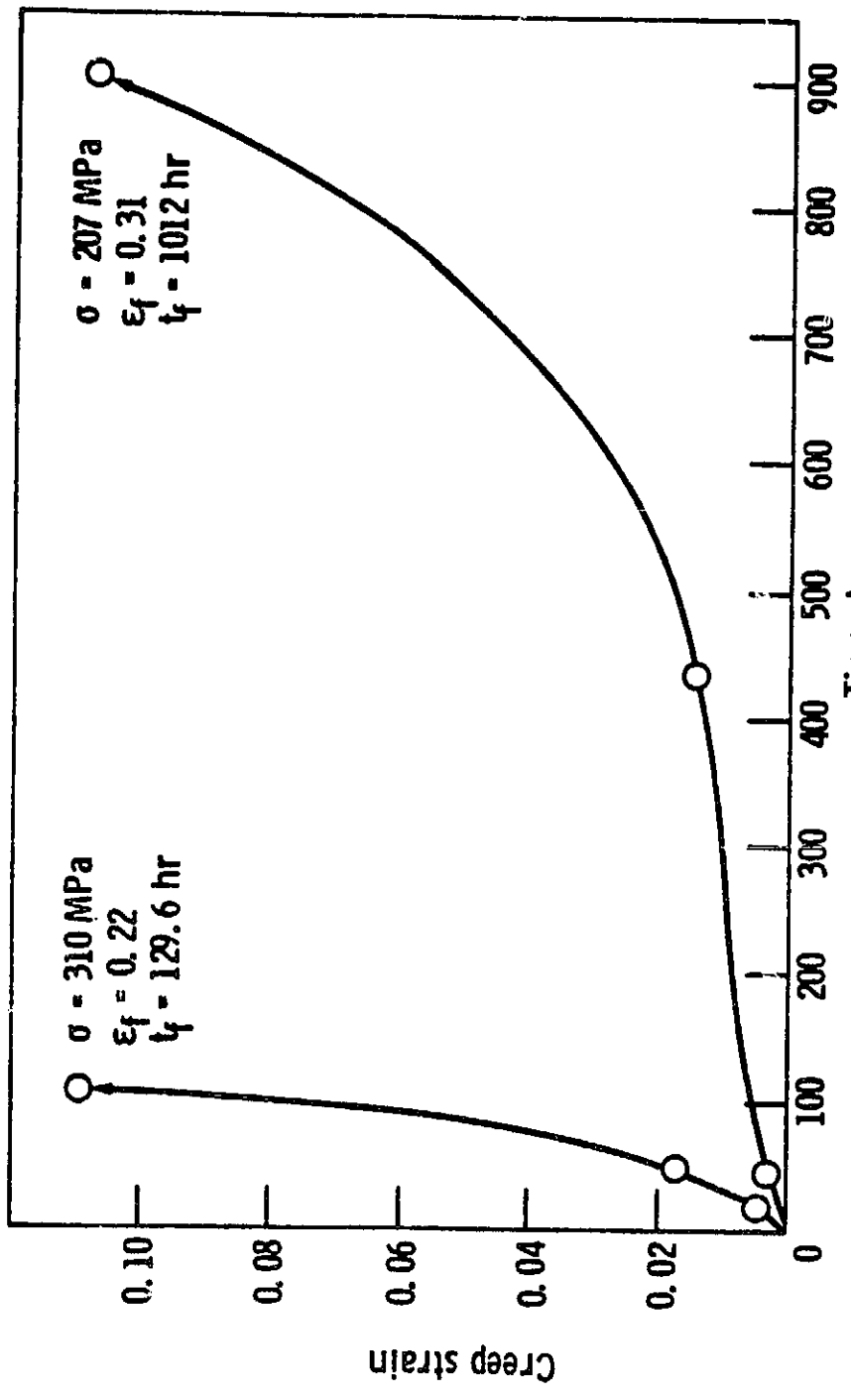

Figure 32. Typical creep curves for Alloy B at 925°C. Open circles correspond to times at which microstructures were evaluated and presented in Figures 33 and 35.

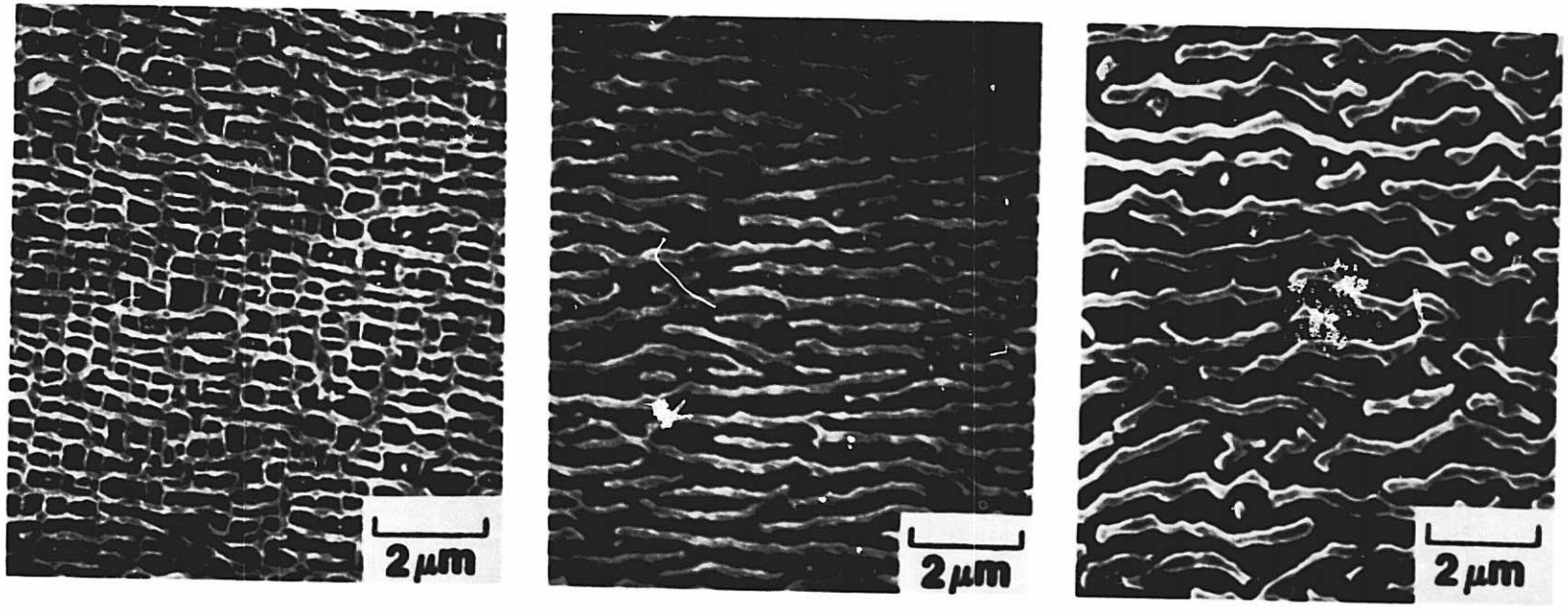

(a) (b) (c)

Figure 33. Longitudinal microstructures of samples creep tested at 925°C and 310 MPa for (a) 17.3 hours, (b) 48 Hours, and (c) 129.6 hours. Stress axis is vertical in all photos.

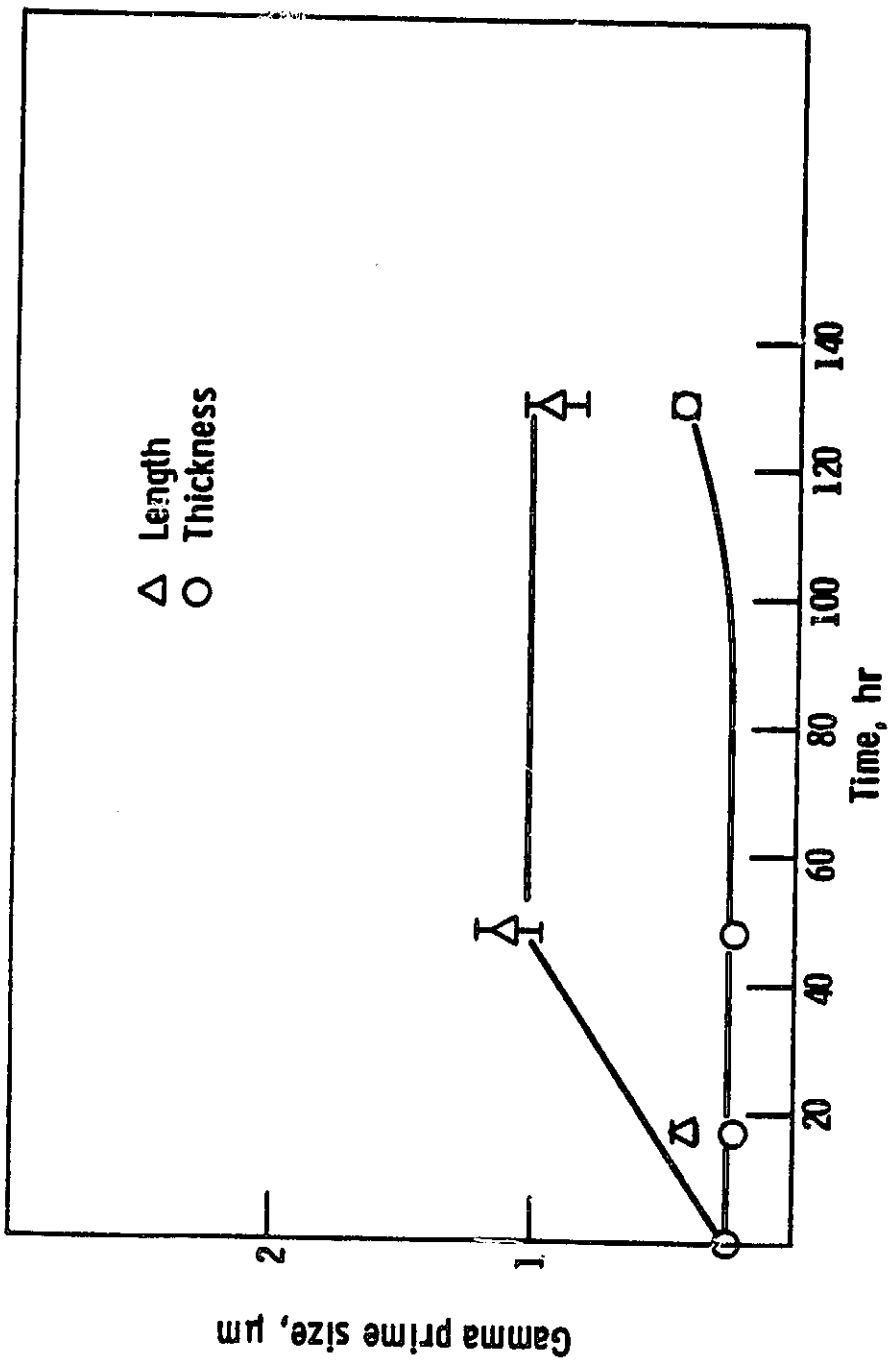

Figure 34. Gamma prime dimensions as a function of creep exposure at 925°C and 310 MPa.

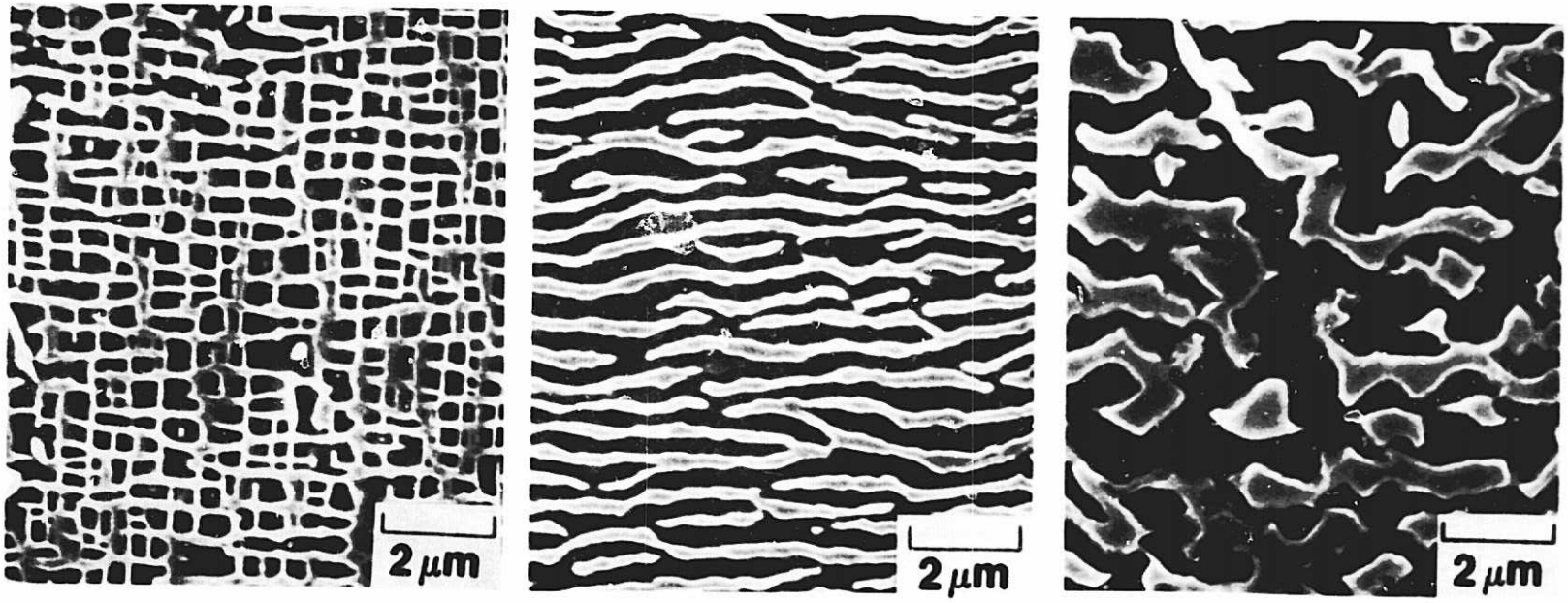

(a) (b) (c)

Figure 35. Longitudinal microstructures of samples creep tested at 925°C and 207 MPa for (a) 45 hours, (b) 434.5 hours, and (c) 1012.65 hours. Stress axis is vertical in all photos.

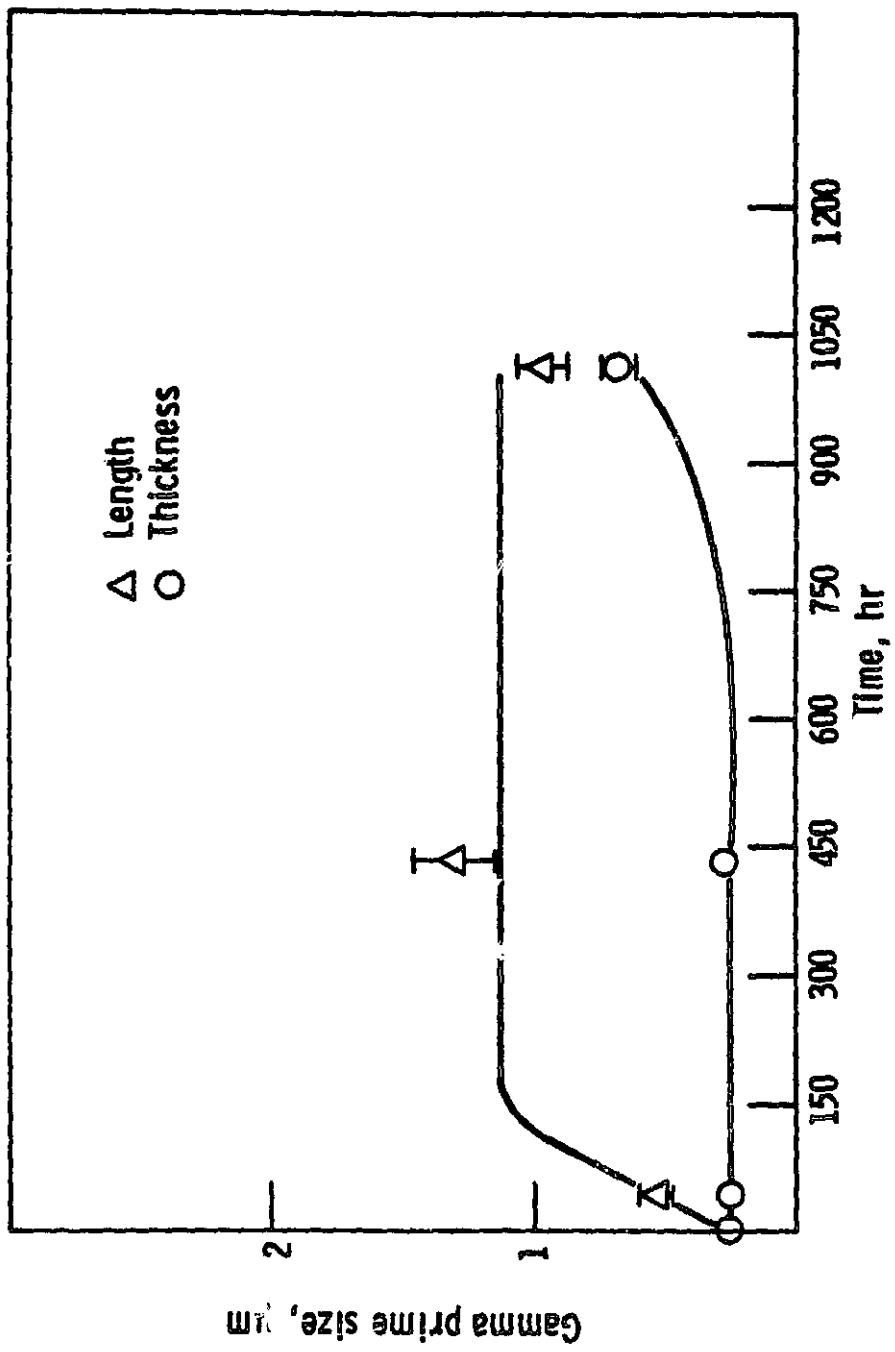

Figure 36. Gamma prime dimensions as a function of creep exposure at 925°C and 207 MPa.

Figure 37. Longitudinal microstructures of samples creep tested at 1000°C and 148 MPa. (a) Alloy C, 30 hours; (b) Alloy E, 20 hours; (c) Alloy F, 20 hours. Stress axis is vertical in all photos.

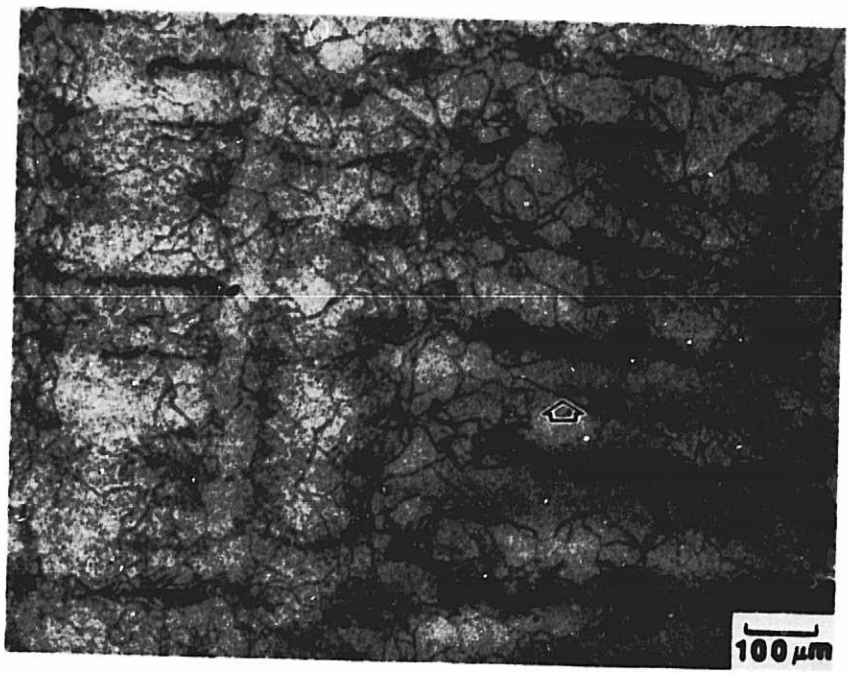

Figure 38. Optical micrograph of Alloy B creep tested at 1000°C and 207 MPa for 5 hours, showing subgrain boundaries(arrow).

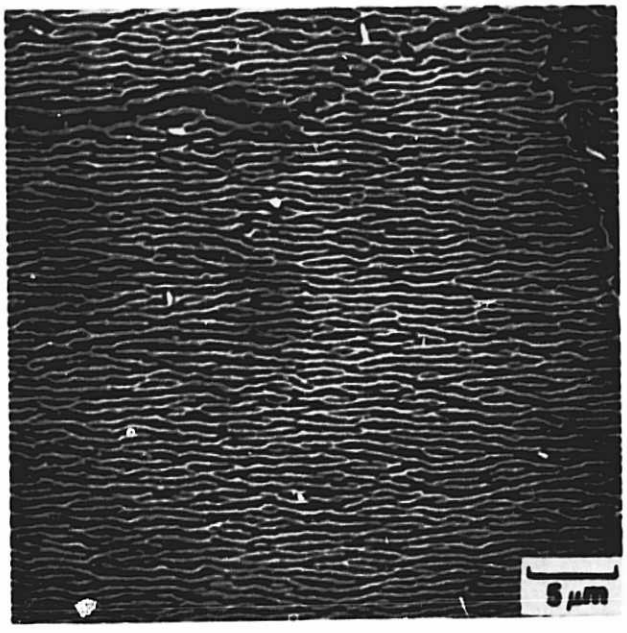

(a)

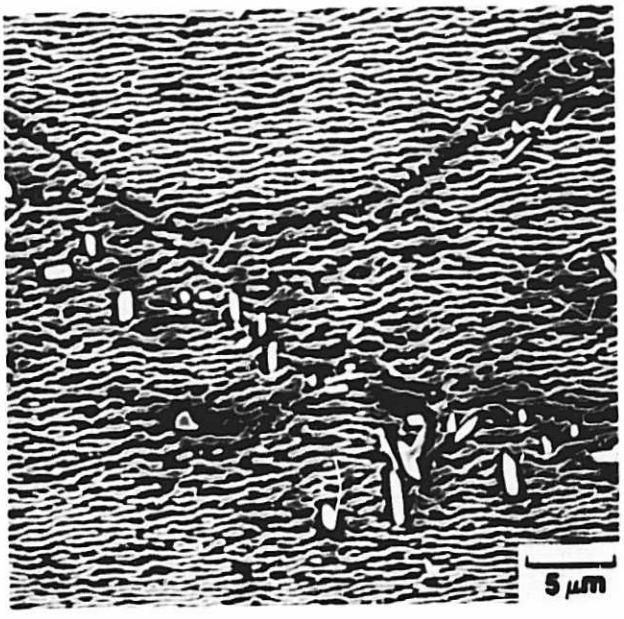

(b)

Figure 39. Examples of discontinuities in the γ-γ' lamellar structure developed during creep of Alloy B at 1000°C and 207 MPa for 46.6 hours. (a) Subgrain boundaries, (b) Tungsten-rich precipitates. Stress axis is verticle in all photos.

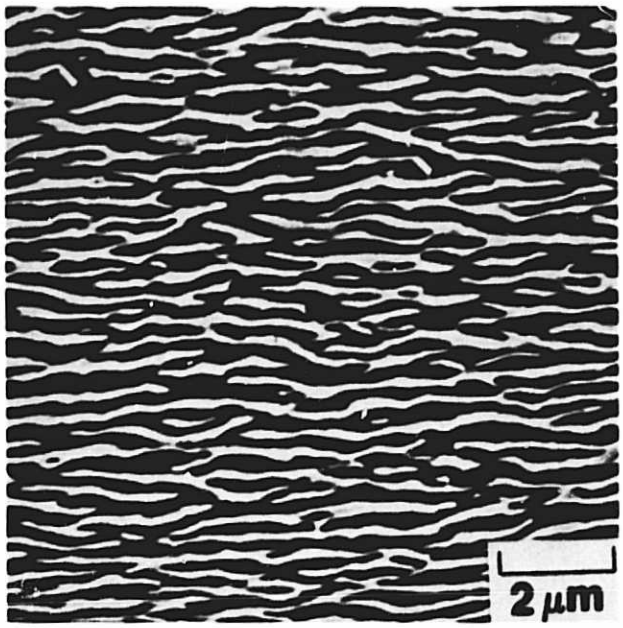

(a)

(b)

Figure 40. Longitudinal microstructures of oil quenched samples of Alloy B tested at 1000°C and 186 MPa. (a) Test interrupted at 37.95 hours; (b) Failed specimen with life of 235.3 hours. Stress axis is vertical in all photos.

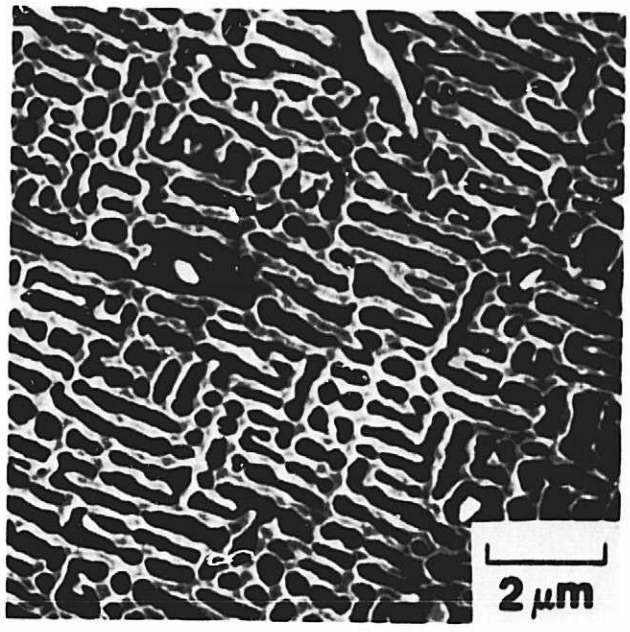

(a)

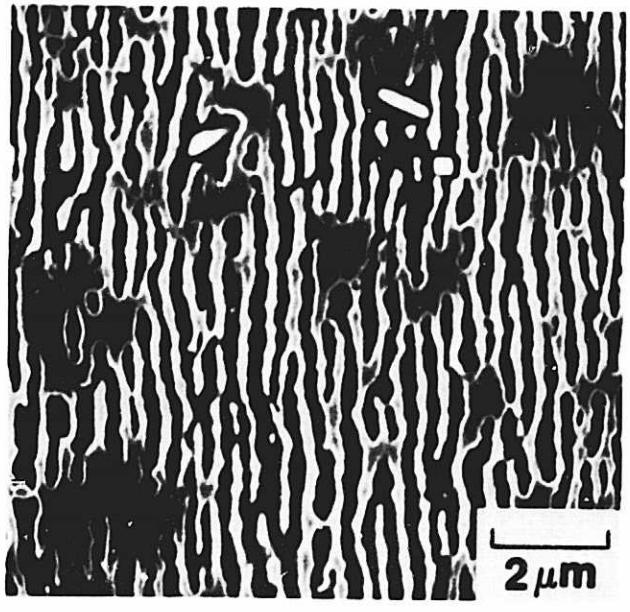

(b)

Figure 41. Microstructure of [001] oriented sample tested in compression at 1000°C for 18.3 hours. (a) Transverse section showing (001) plane; (b) longitudinal section showing (010) plane. Compressive axis is vertical in (b).

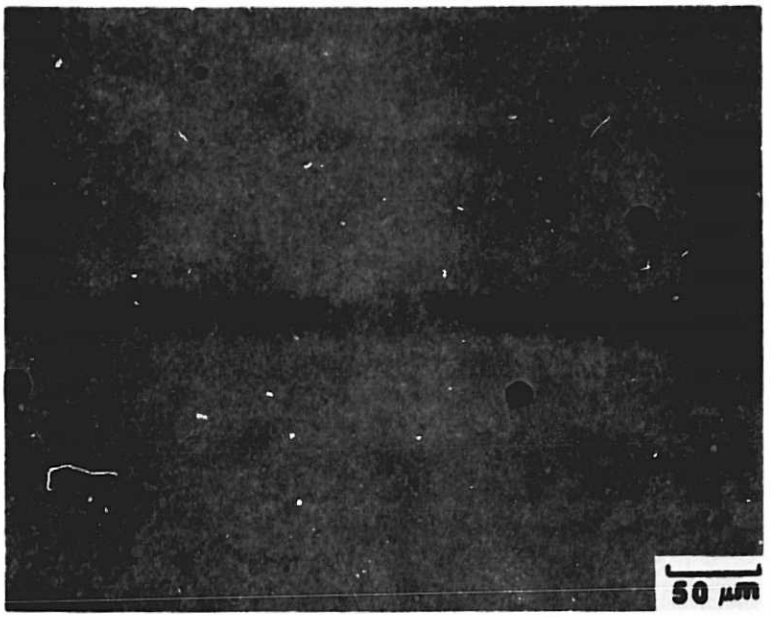

(a)

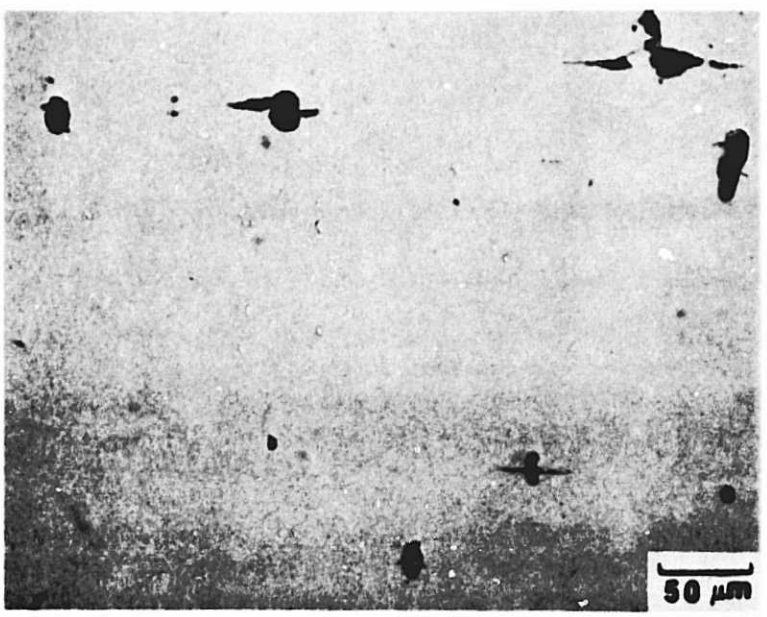

(b)

Figure 42. Optical micrographs of longitudinal sections of Alloy B creep tested at 1000°C and 207 MPa: (a) Test interrupted at 75.5 hours; (b) After failure at 110.4 hours. Cracks initiated at pores are present only in (b).

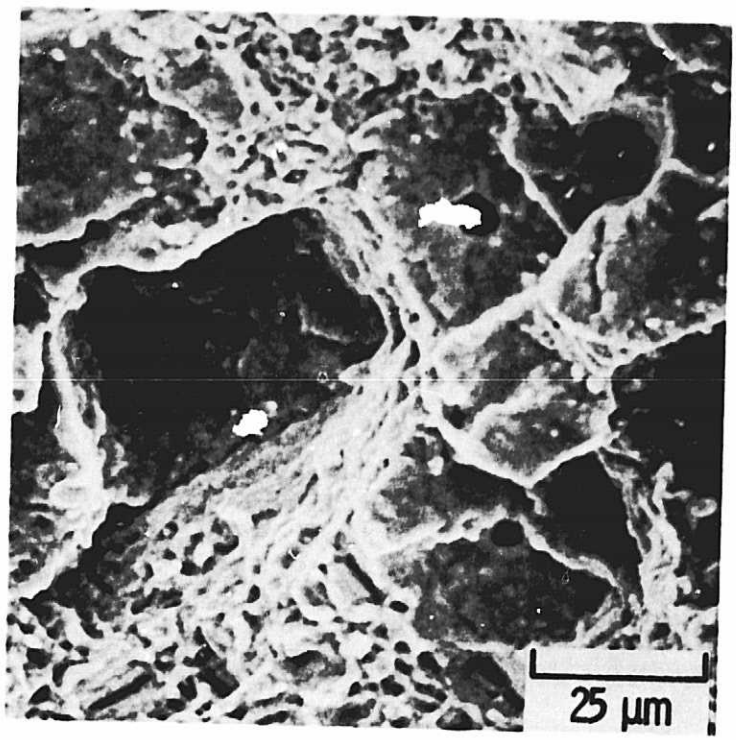

Figure 43. Scanning electron micrograph of the fracture surface of Alloy B at 1000°C and 207 MPa.

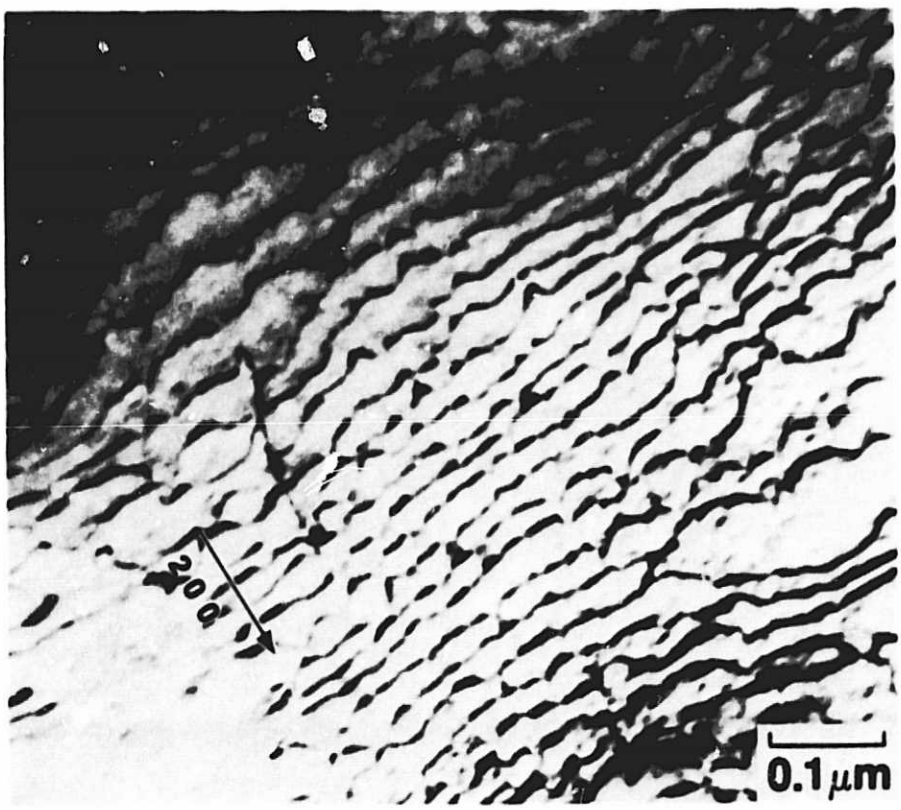

Figure 44. Transverse section of Alloy B creep tested at 1000°C and 148 MPa for 45.89 hours, illustrating the hexagonal array of misfit dislocations.

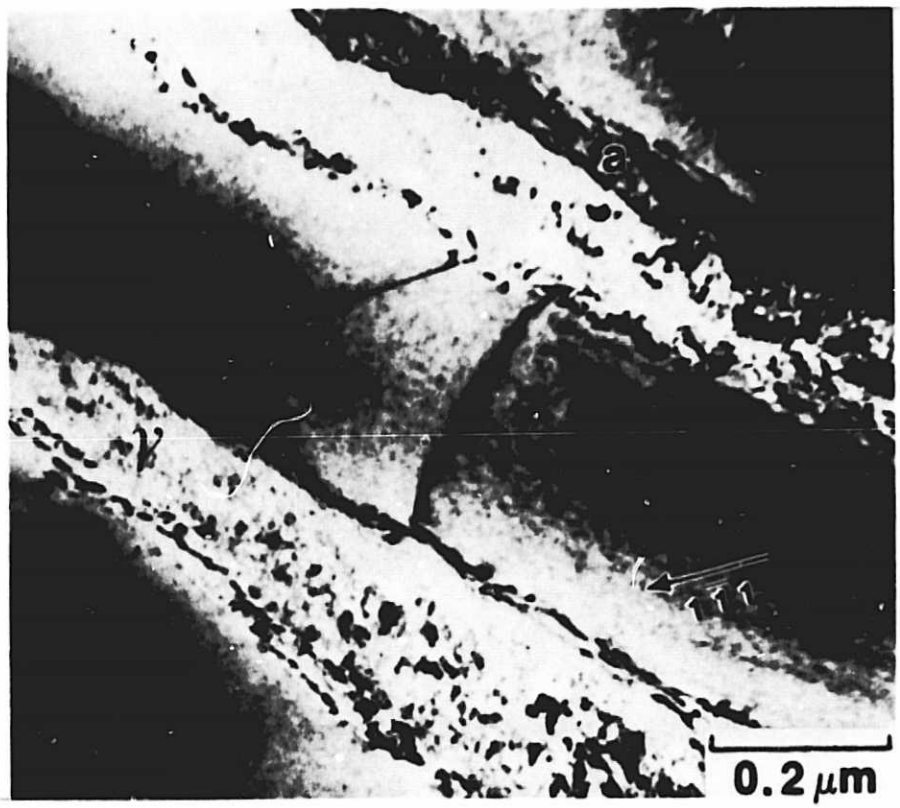

Figure 45. Longitudinal section of the same specimen illustrated in Figure 44. Note dislocations in the γ' phase and misfit dislocations at "a".

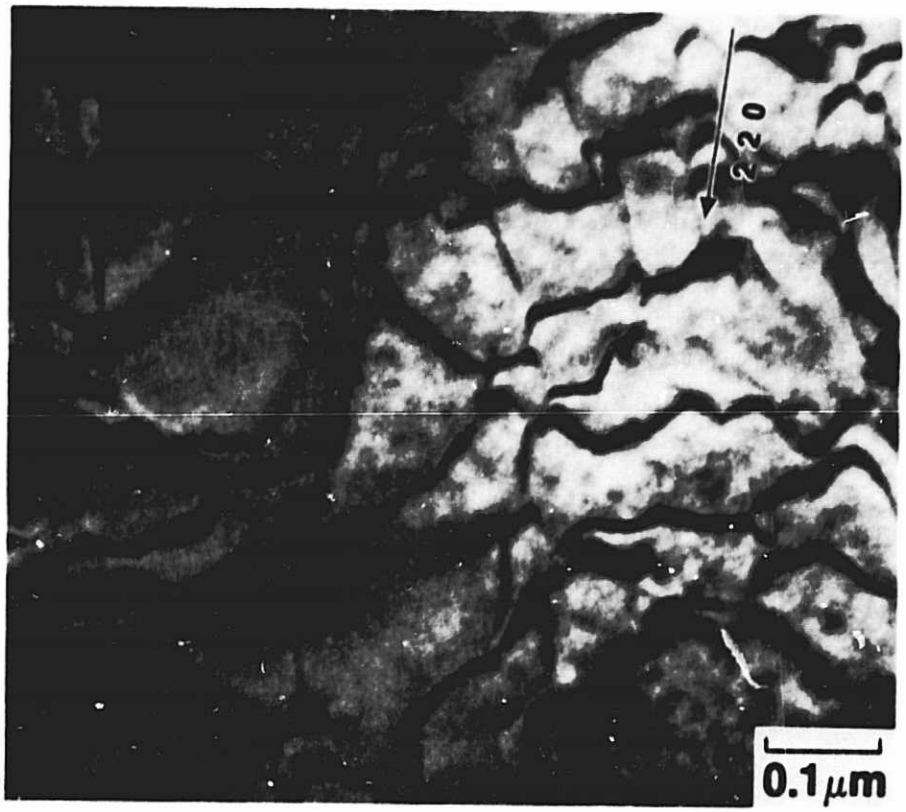

Figure 46 Transverse section of Alloy E creep tested at 1000°C and 148 MPa for 60.3 hours. Note the dislocation spacings for this alloy in comparison with Alloy B.

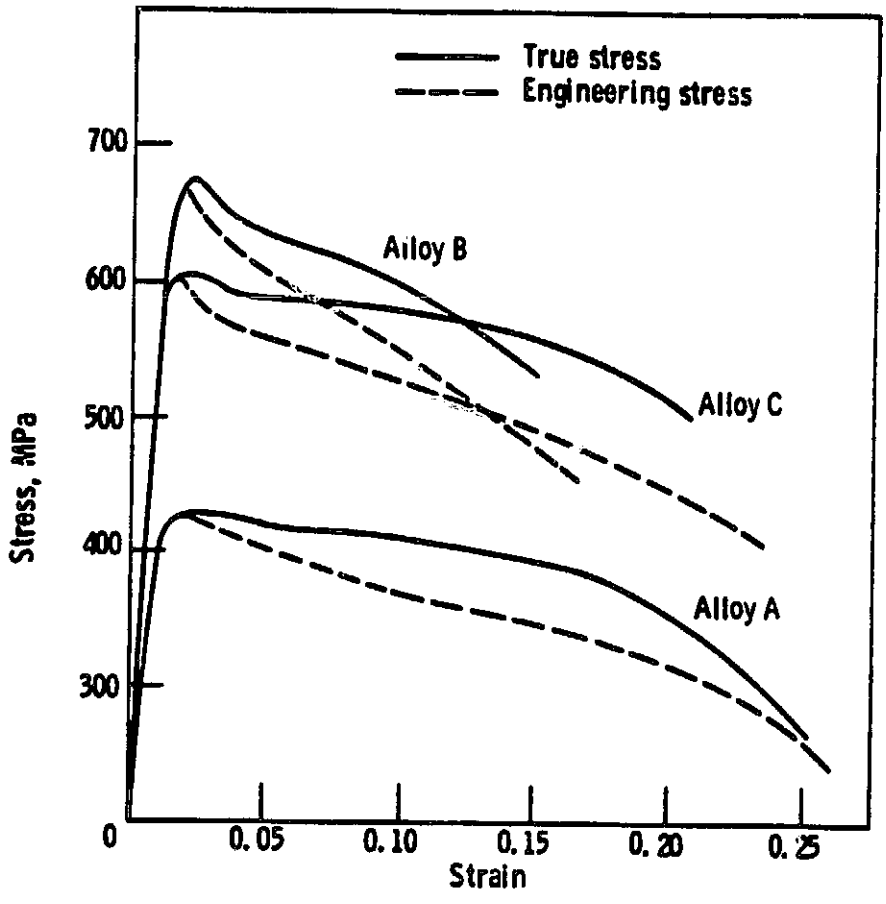

Figure 47 Stress-strain curves for single crystal alloys at 1000°C.

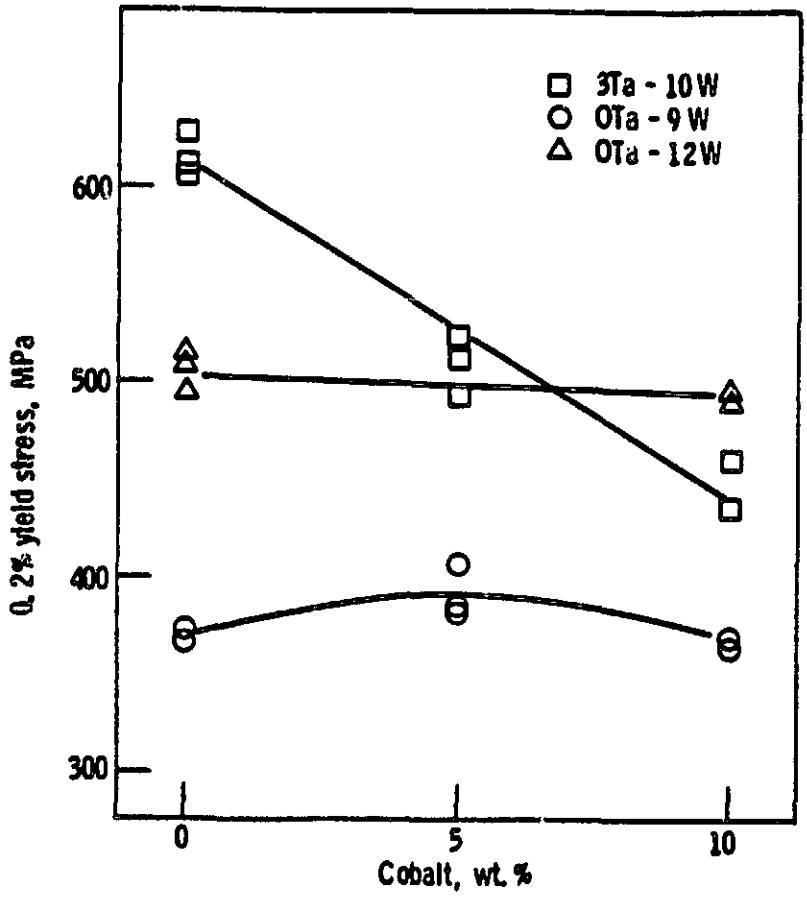

Figure 48. The 0.2 percent yield stress at 1000°C for the single crystal alloys.

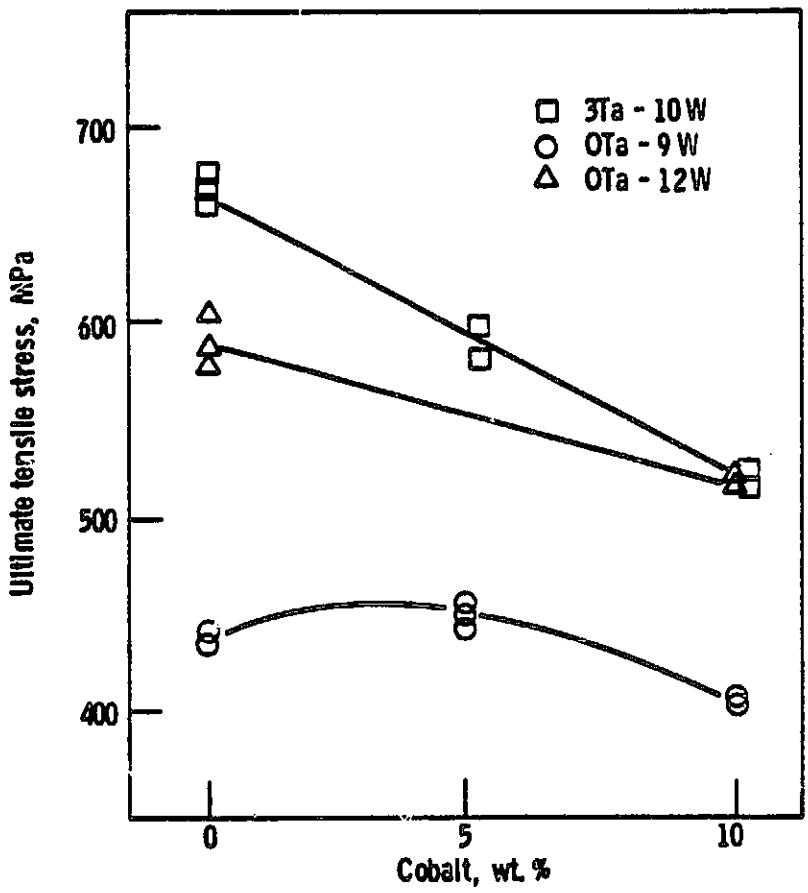

Figure 49. The ultimate tensile strength at 1000°C for the single crystal alloys.

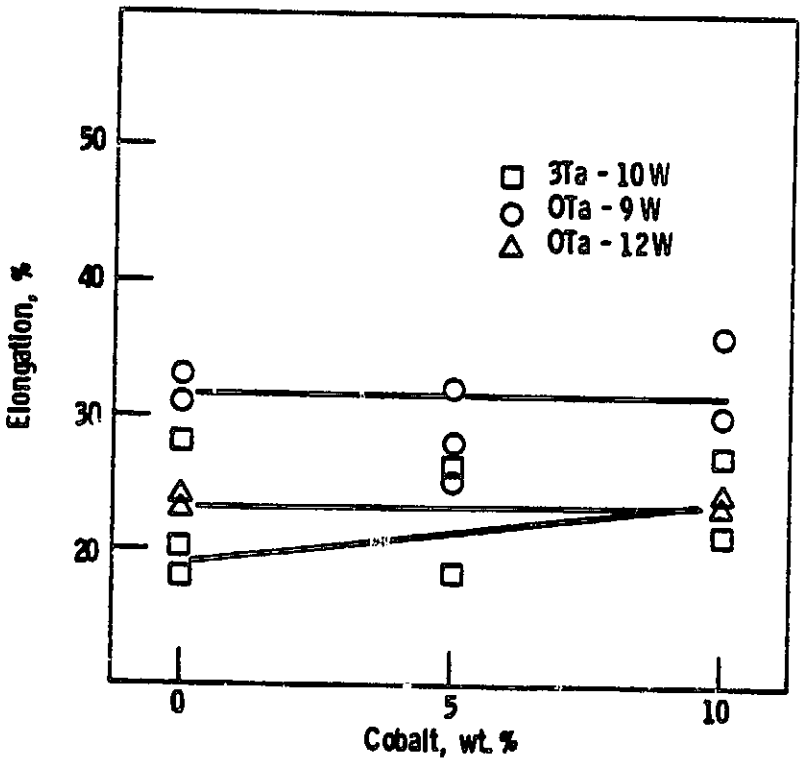

Figure 90. Tensile ductilities at 1000°C for the single crystal alloys.

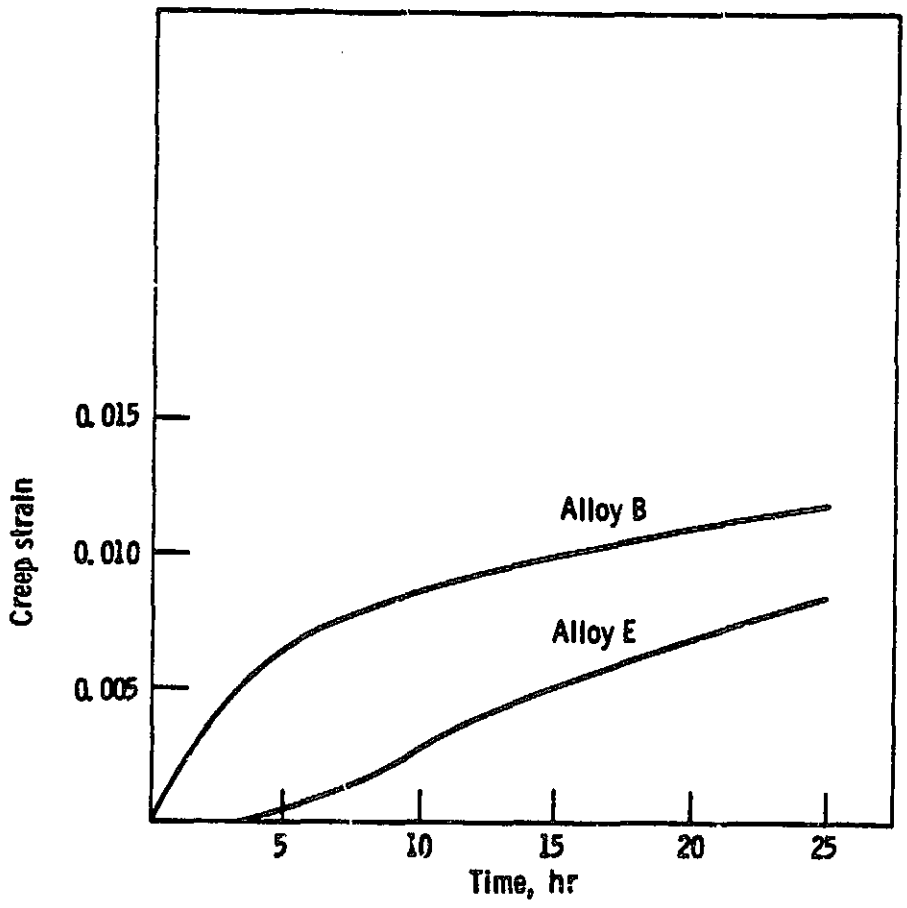

Figure 51. Primary creep curves for Alloys B and E at 1000°C and 207 MPa.

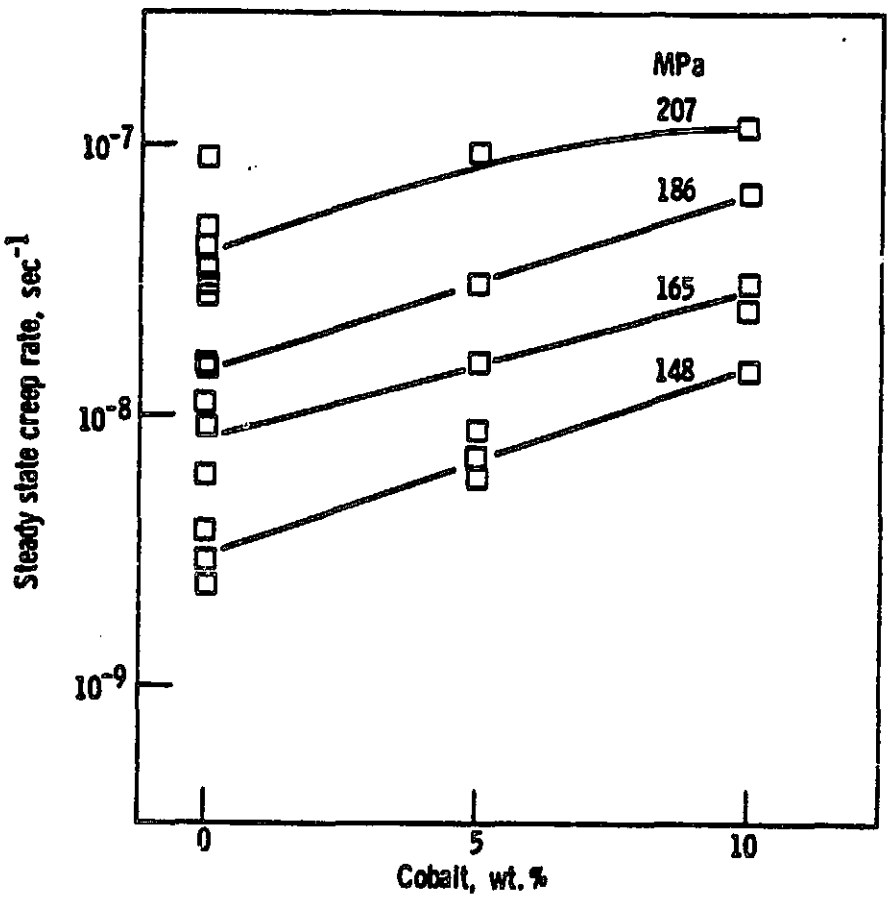

Figure 52. Steady state creep rates at 1000°C and various stress levels as a function of Co level in the 3Ta-10W alloys.

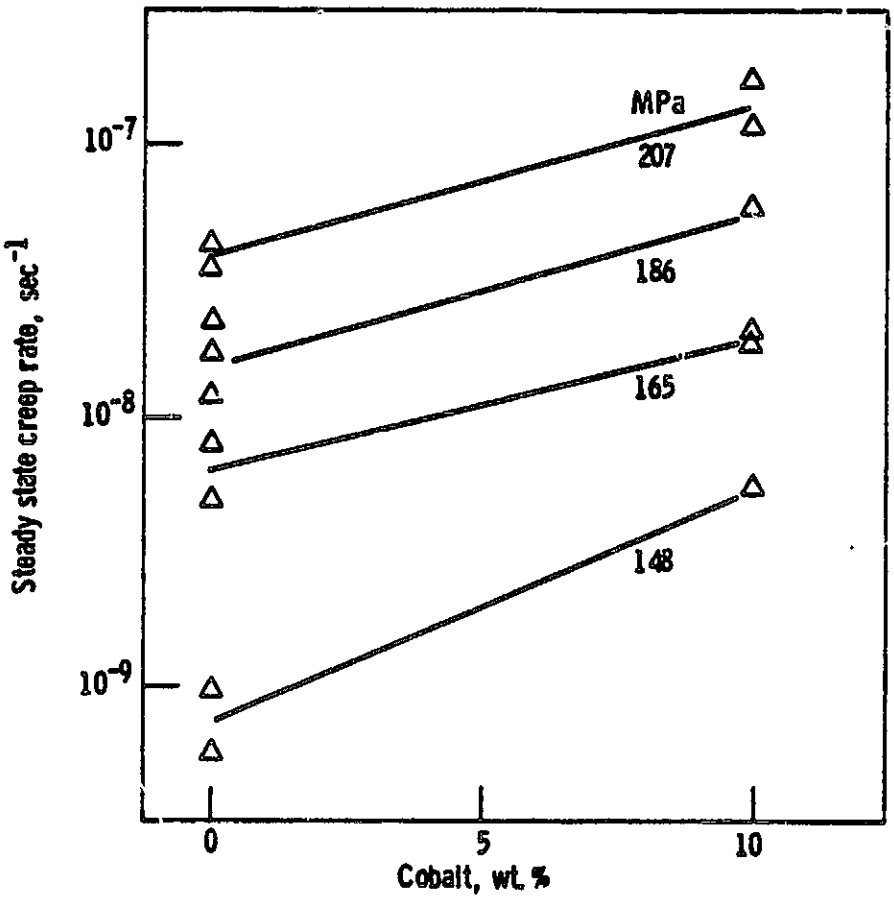

Figure 53. Steady state creep rates at 1000°C and various stress levels as a function of Co level in the 0Ta-12W alloys.

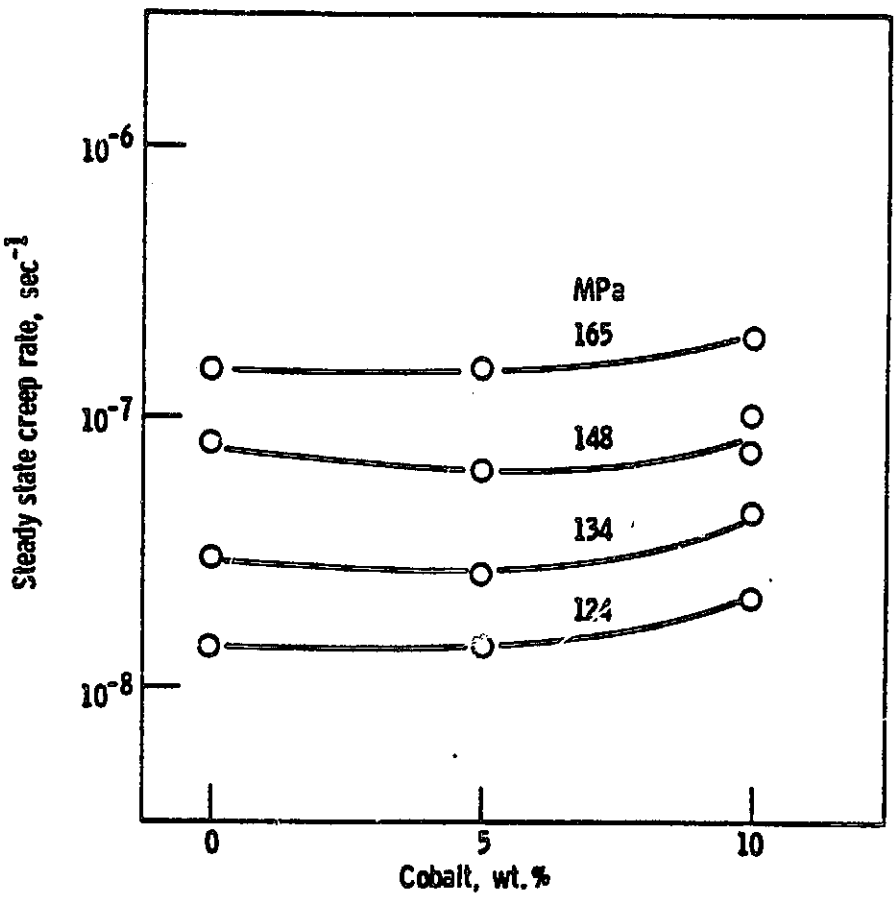

Figure 54. Steady state creep rates at 1000°C and various stress levels as a function of Co level in the OTa-9W alloys.

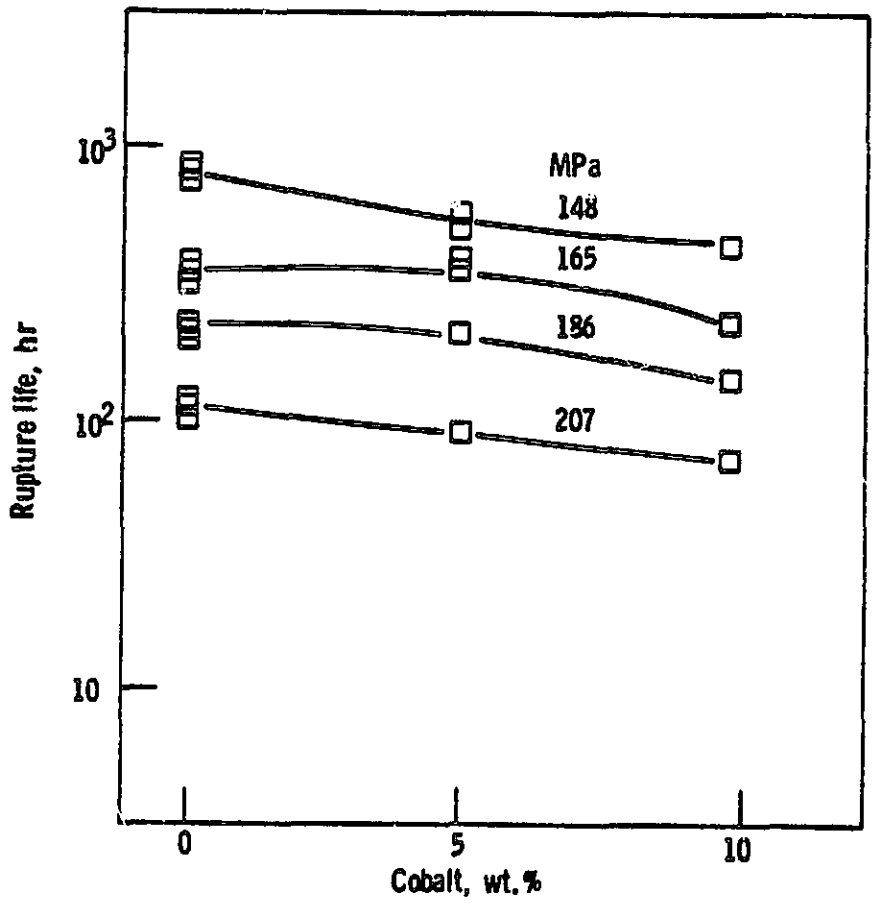

Figure 55. Rupture lives at 1000°C and various stress levels as a function of Co level in the 3Ta-10W alloys.

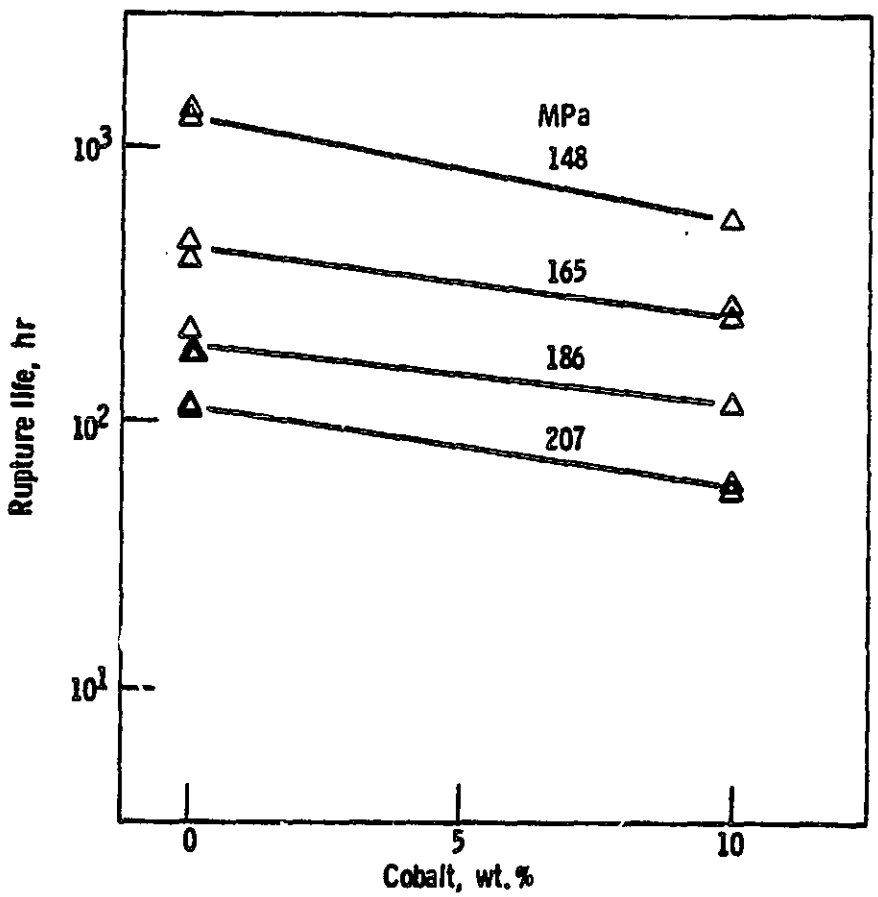

Figure 56. Rupture lives at 1000°C and various stress levels as a function of Co level in the 0Ta-12W alloys.

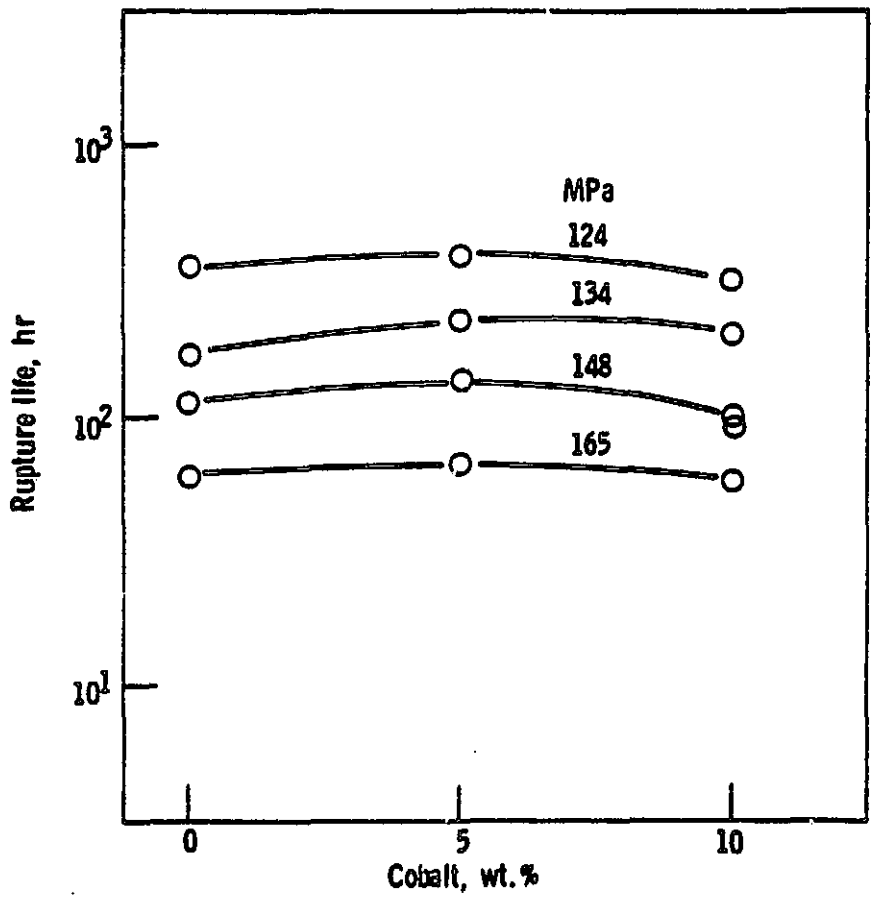

Figure 57. Rupture lives at 1000°C and various stress levels as a function of Co level in the 0Ta-9W alloys.

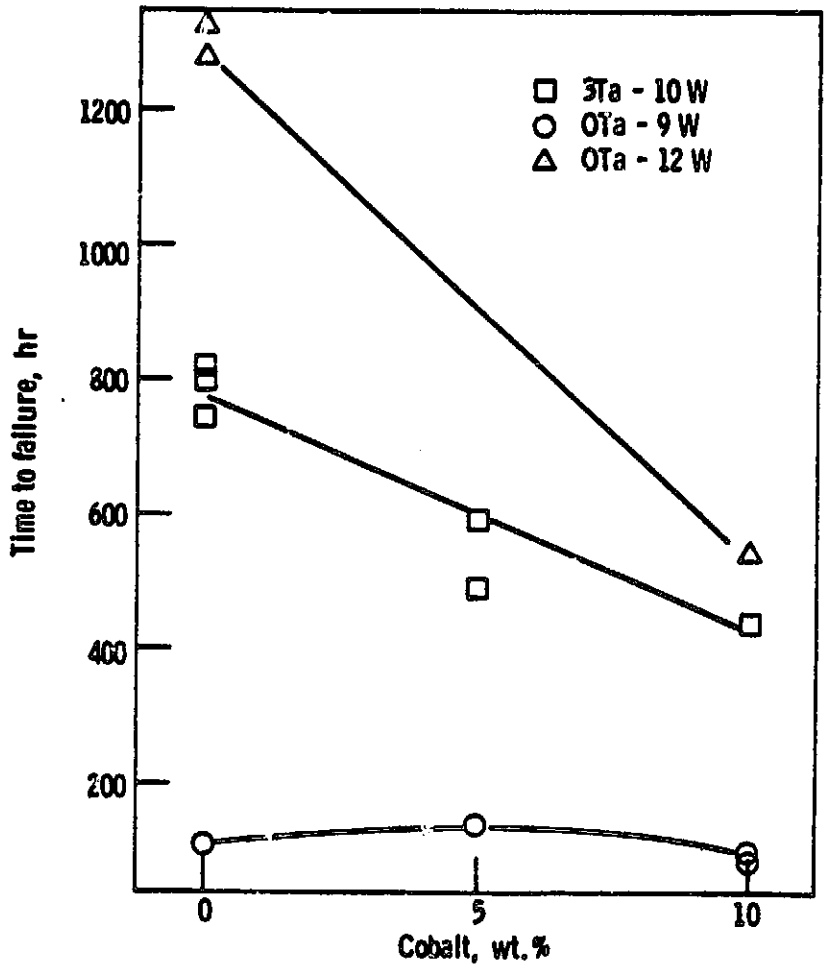

Figure 58. A summary plot of the rupture lives of the single crystal alloys at 1000°C and 148 MPa.

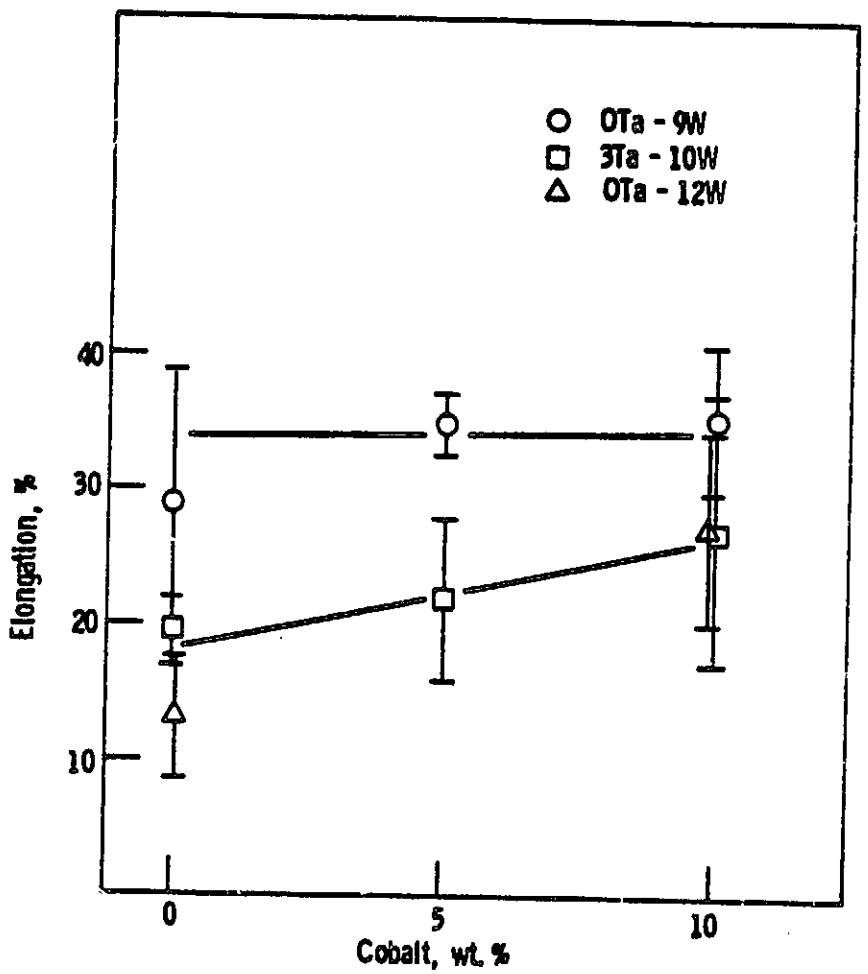

Figure 59. Creep ductility at 1000°C for the single crystal alloys.

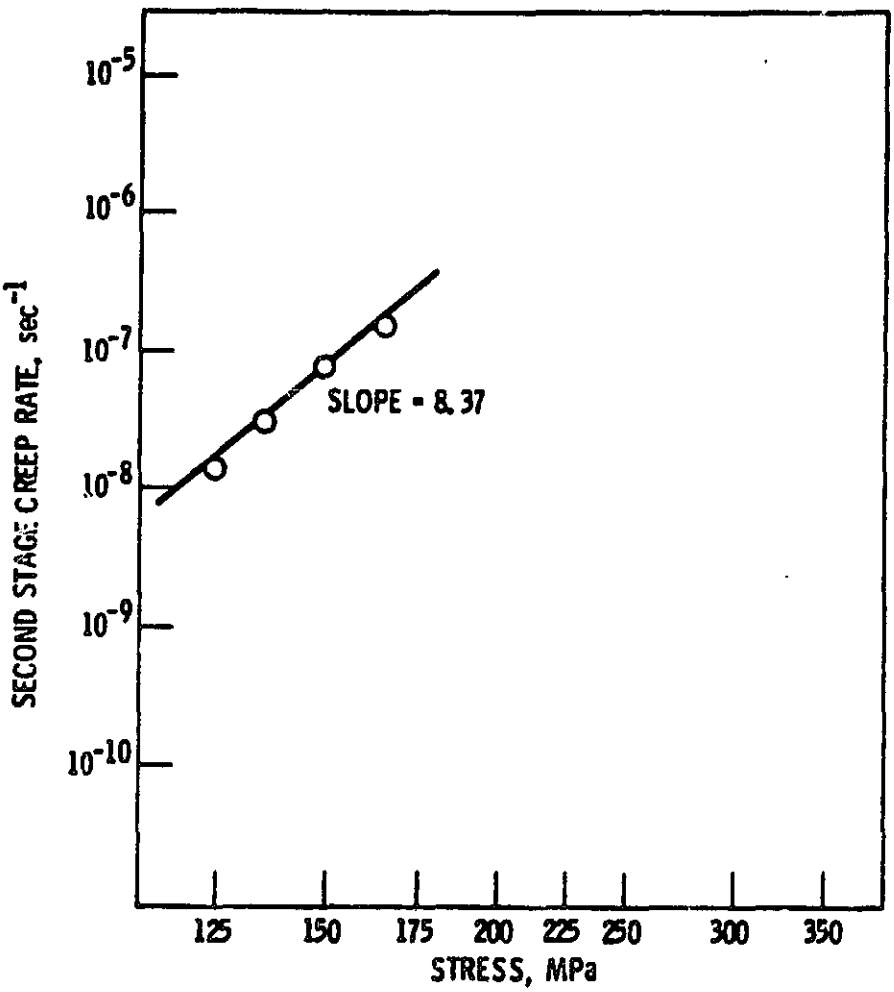

Figure 60. Stress dependence of the steady state creep rate of Alloy A at 1000°C.

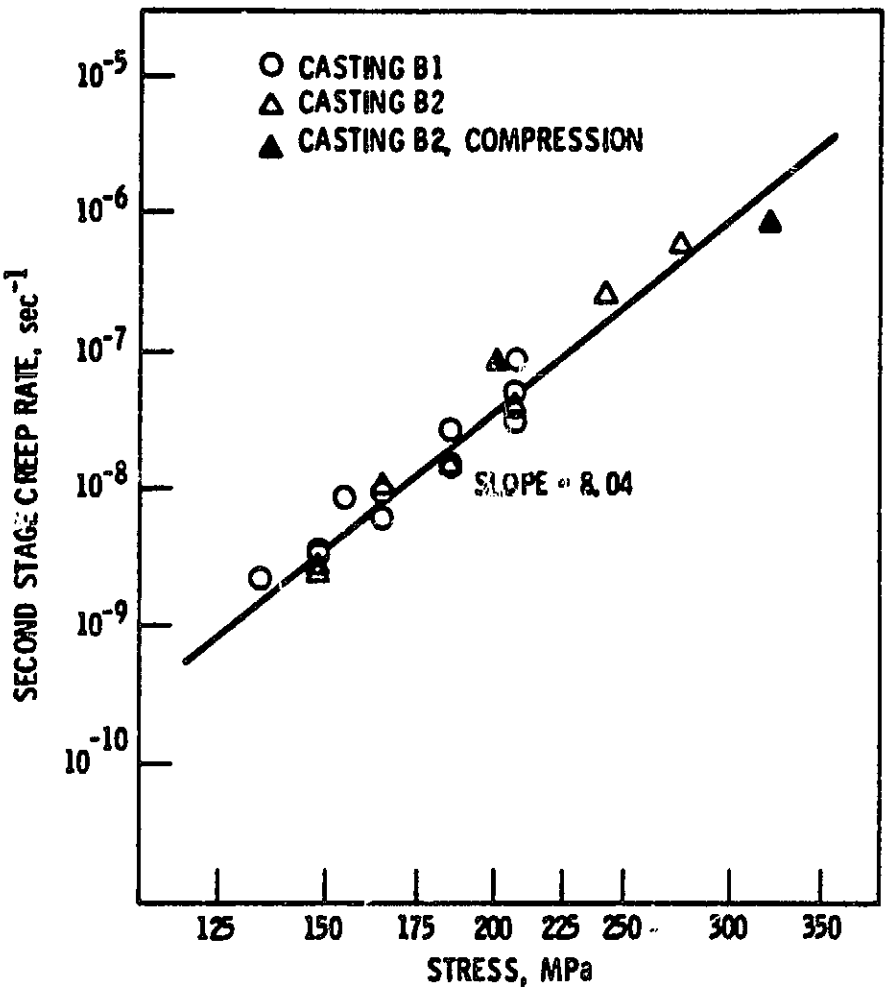

Figure 61. Stress dependence of the steady state creep rate of Alloy B at 1000°C.

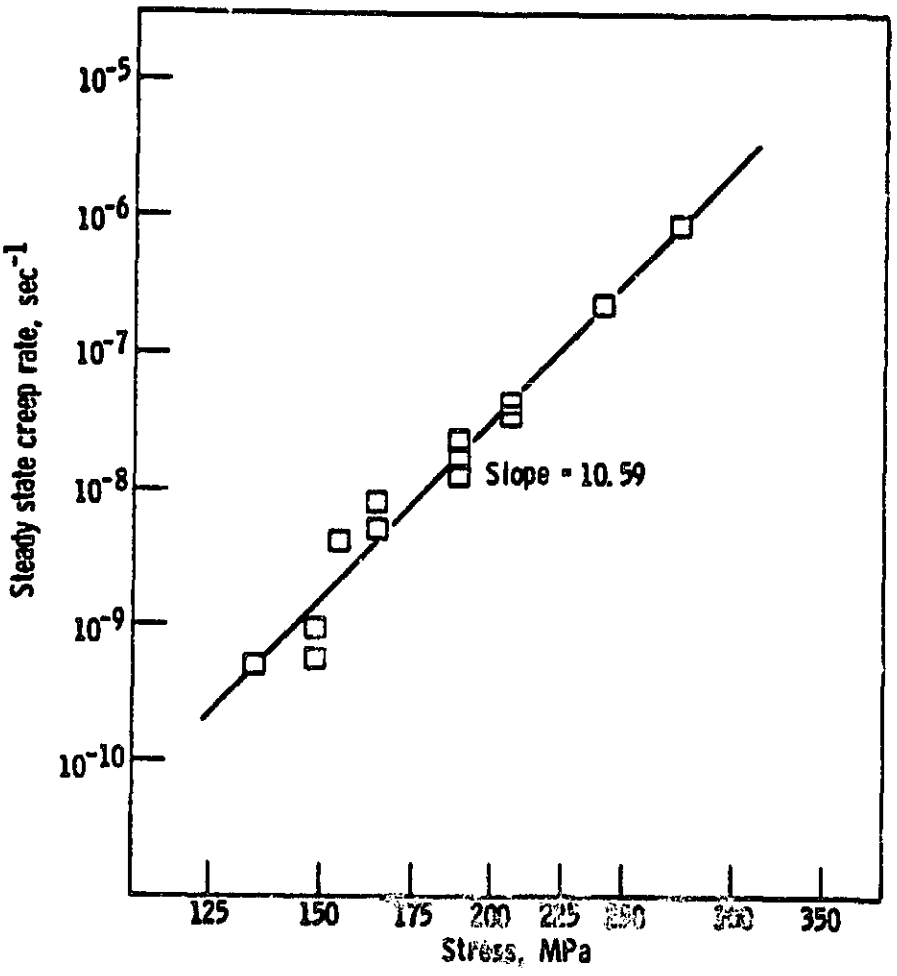

Figure 62. Stress dependence of the steady state creep rate of Alloy C at 1000°C.

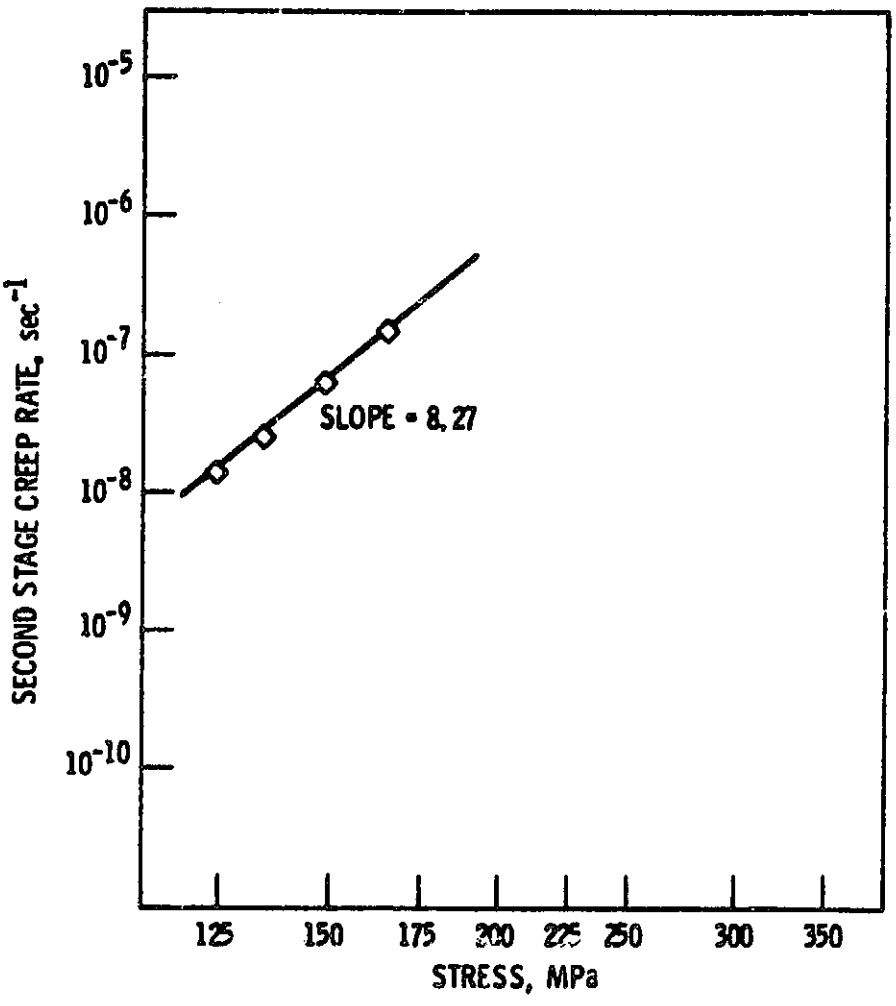

Figure 63. Stress dependence of the steady state creep rate of Alloy D at 1000°C.

C-3

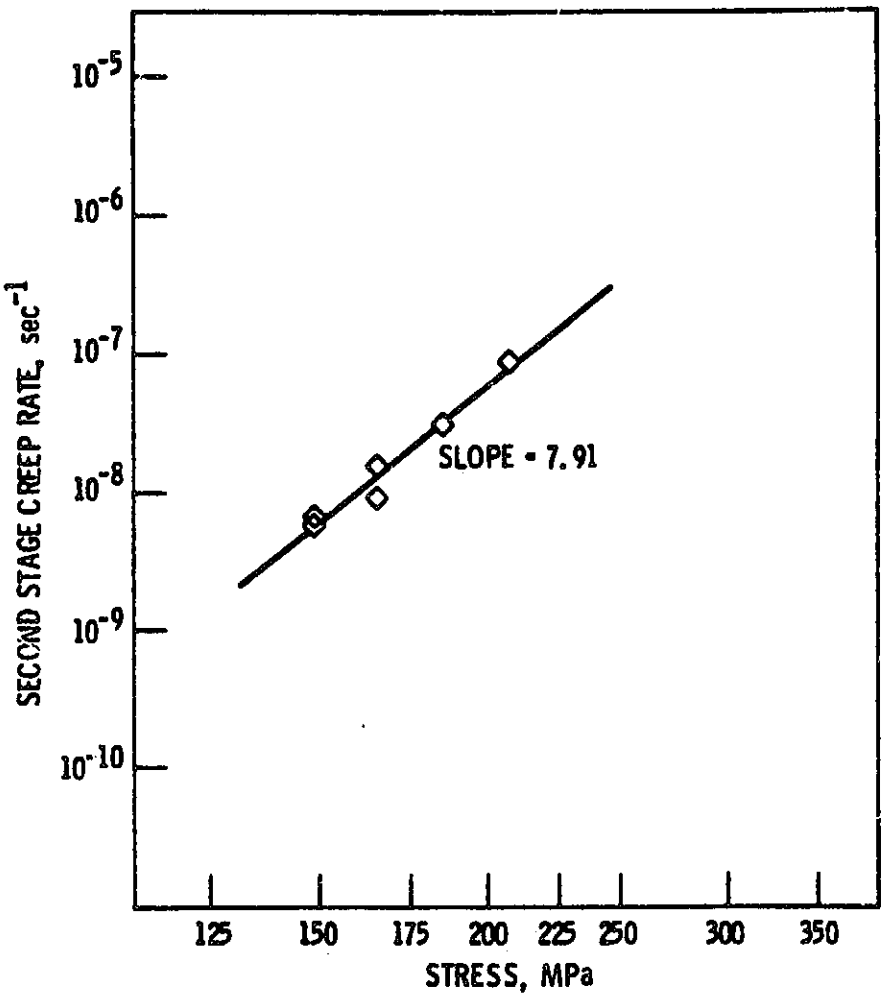

Figure 64. Stress dependence of the steady state creep rate of Alloy E at 1000°C.

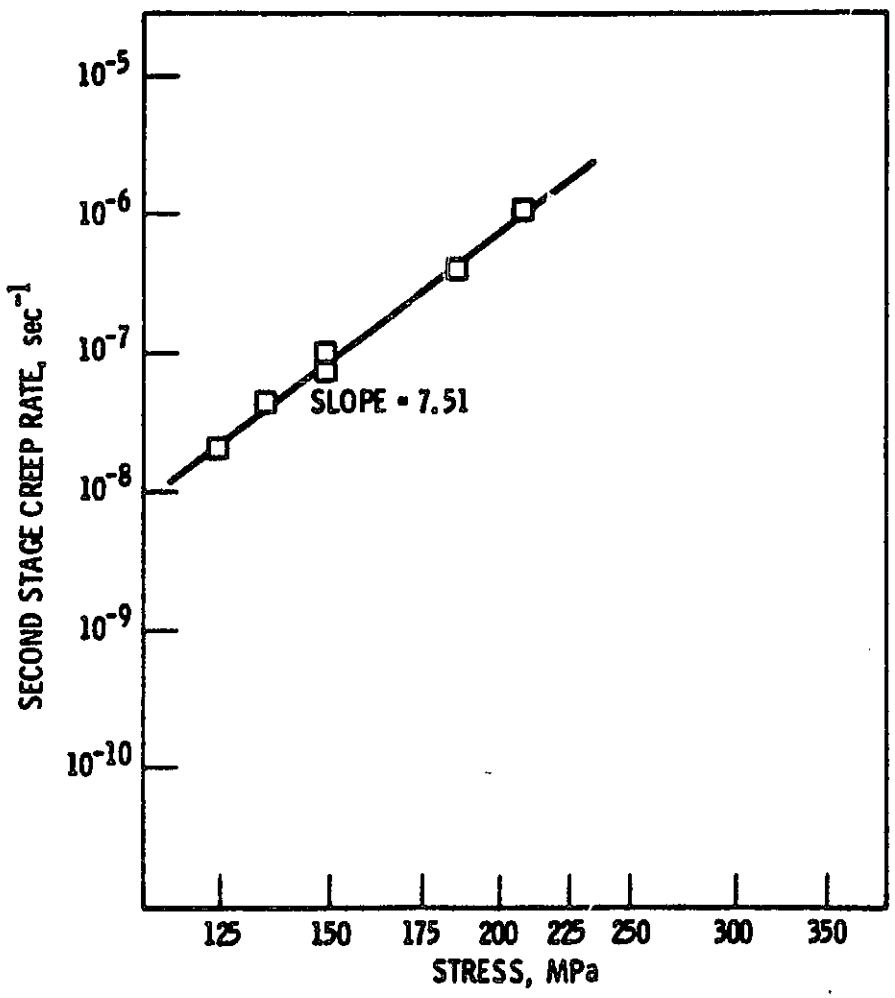

Figure 65. Stress dependence of the steady state creep rate of Alloy F at 1000°C.

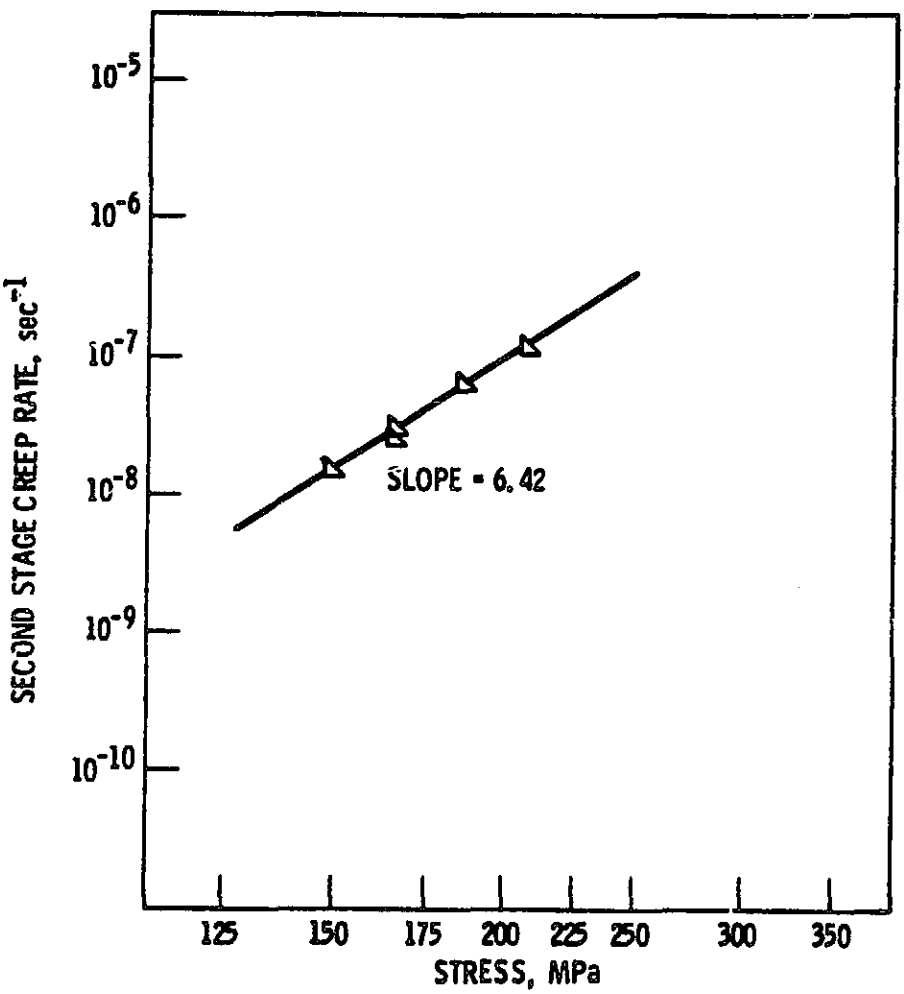

Figure 66. Stress dependence of the steady state creep rate of Alloy G at 1000°C.

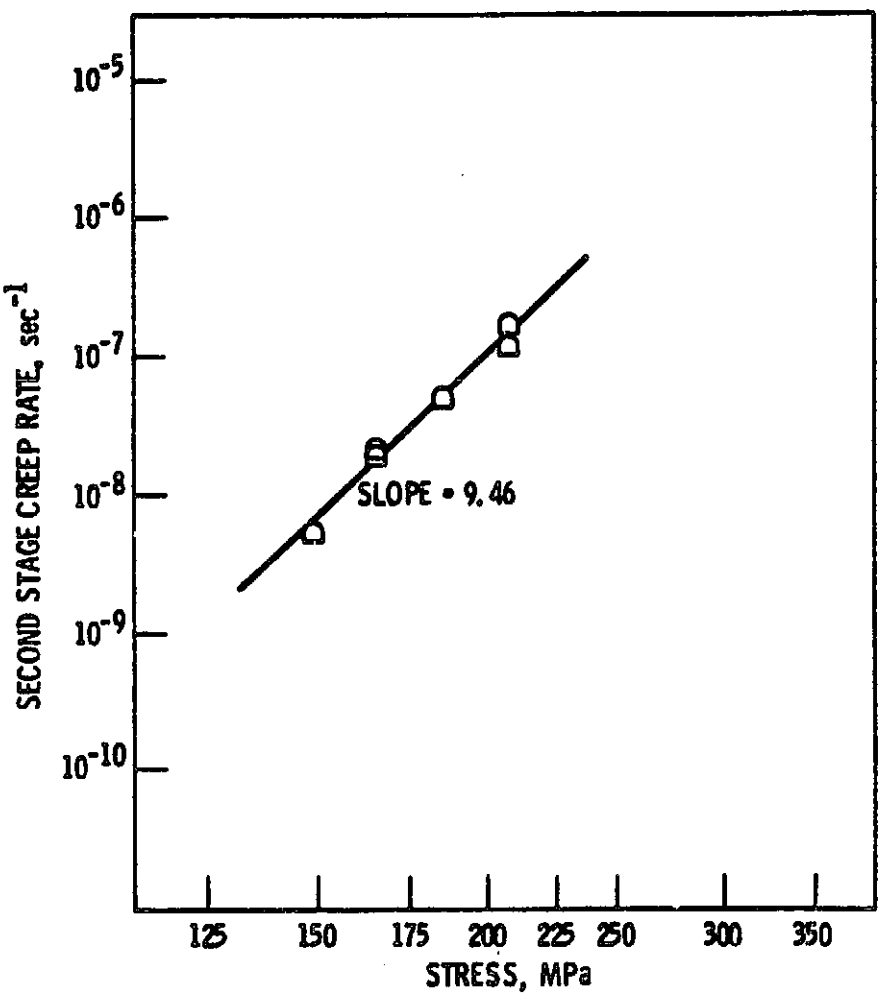

Figure 67. Stress dependence of the steady state creep rate of Alloy H at 1000°C.

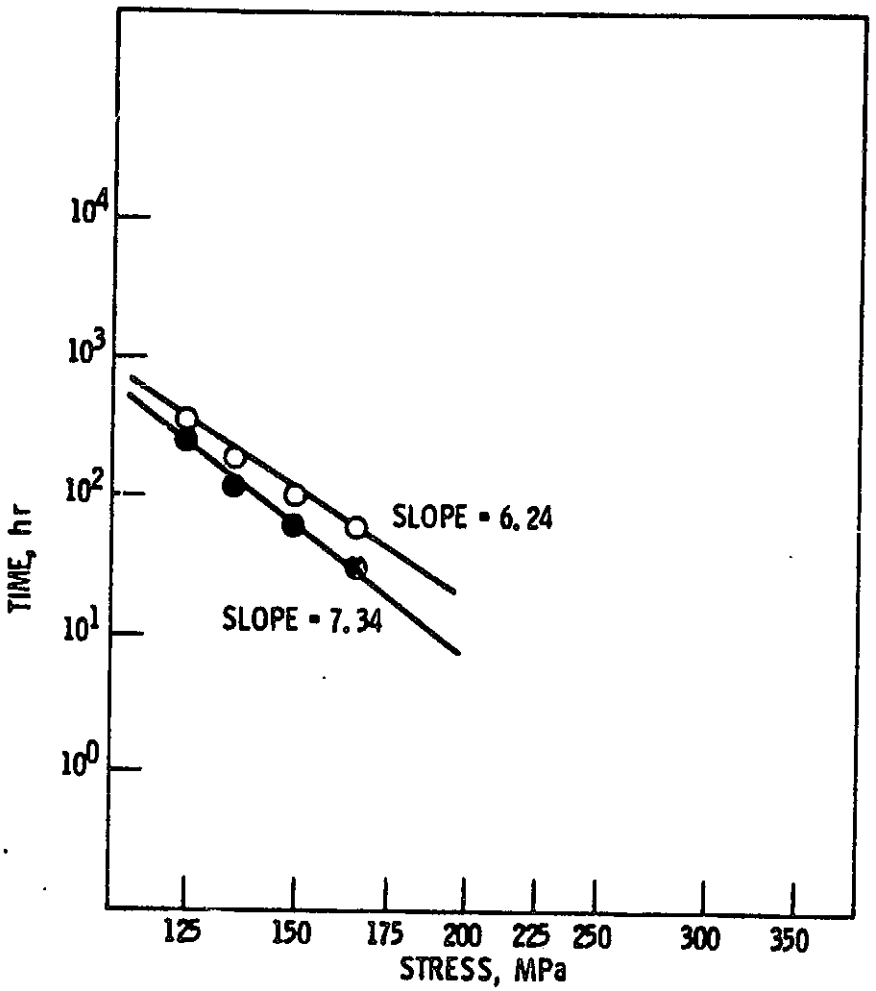

Figure 68. Stress dependence of the time to failure (open symbols) and the time to the onset of tertiary creep (filled symbols) for Alloy A at 1000°C

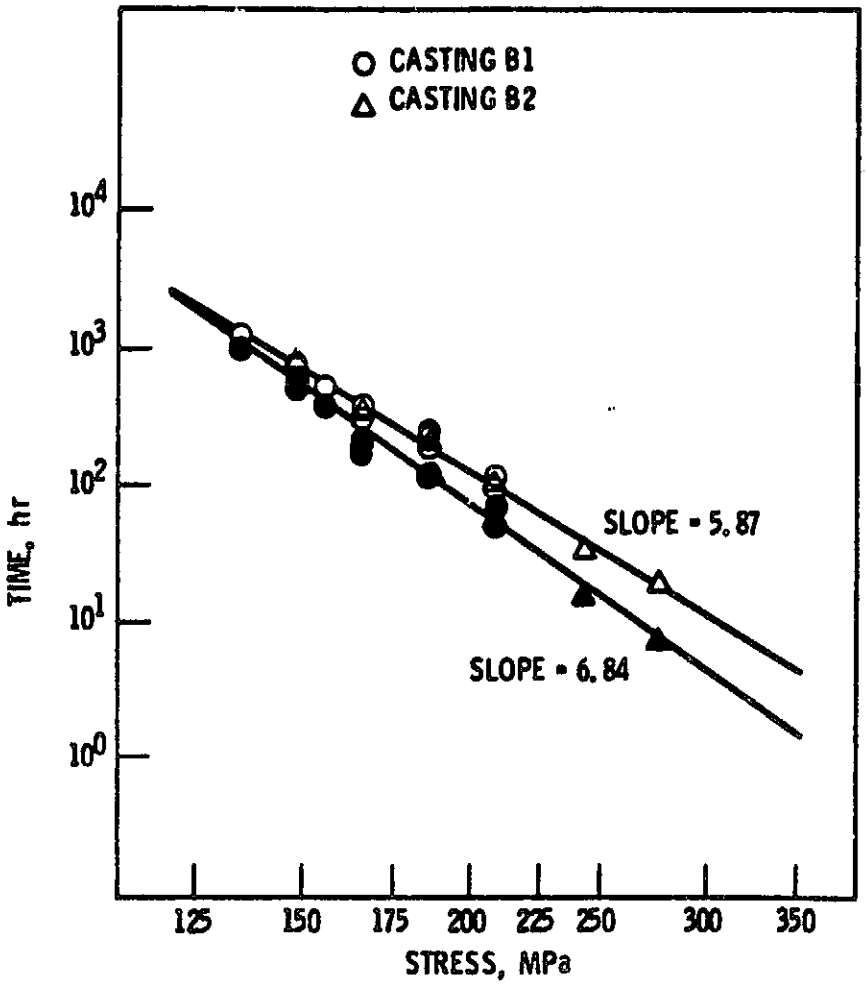

Figure 69. Stress dependence of the time to failure (open symbols) and the time to the onset of tertiary creep (filled symbols) for Alloy B at 1000°C.

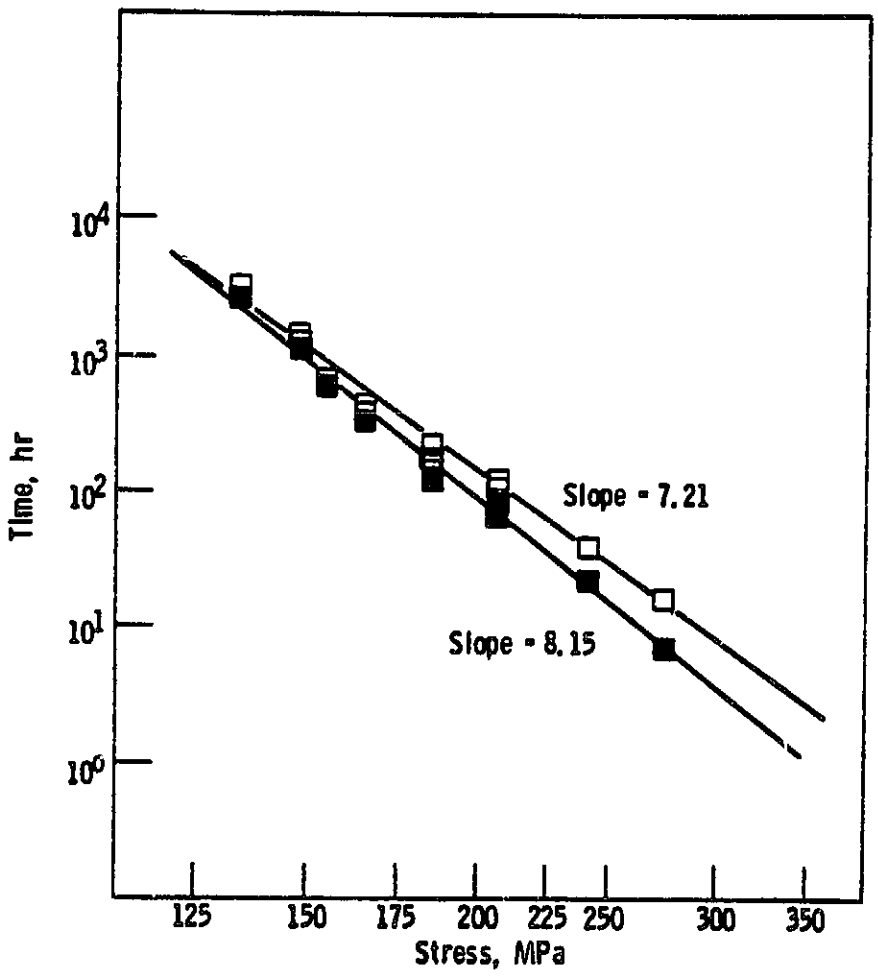

Figure 70. Stress dependence of the time to failure (open symbols) and the time to the onset of tertiary creep (filled symbols) for Alloy C at 1000°C.

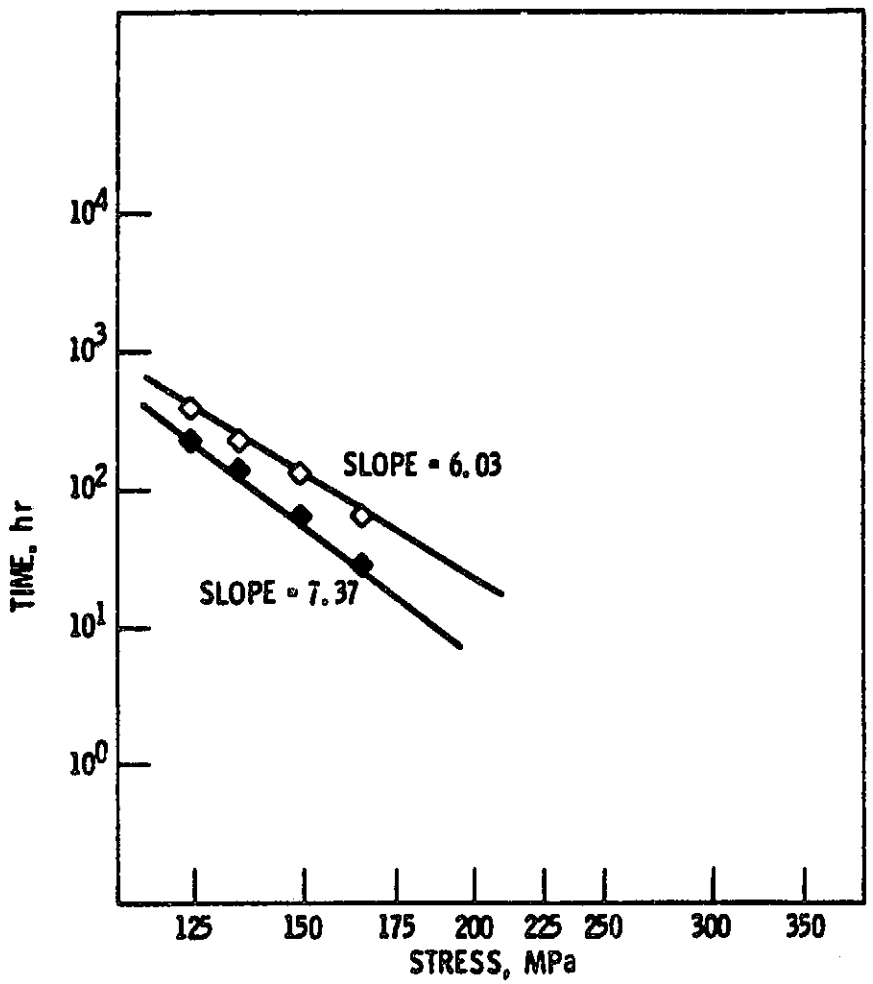

Figure 71. Stress dependence of the time to failure (open symbols) and the time to the onset of tertiary creep (filled symbols) for Alloy D at 1000°C.

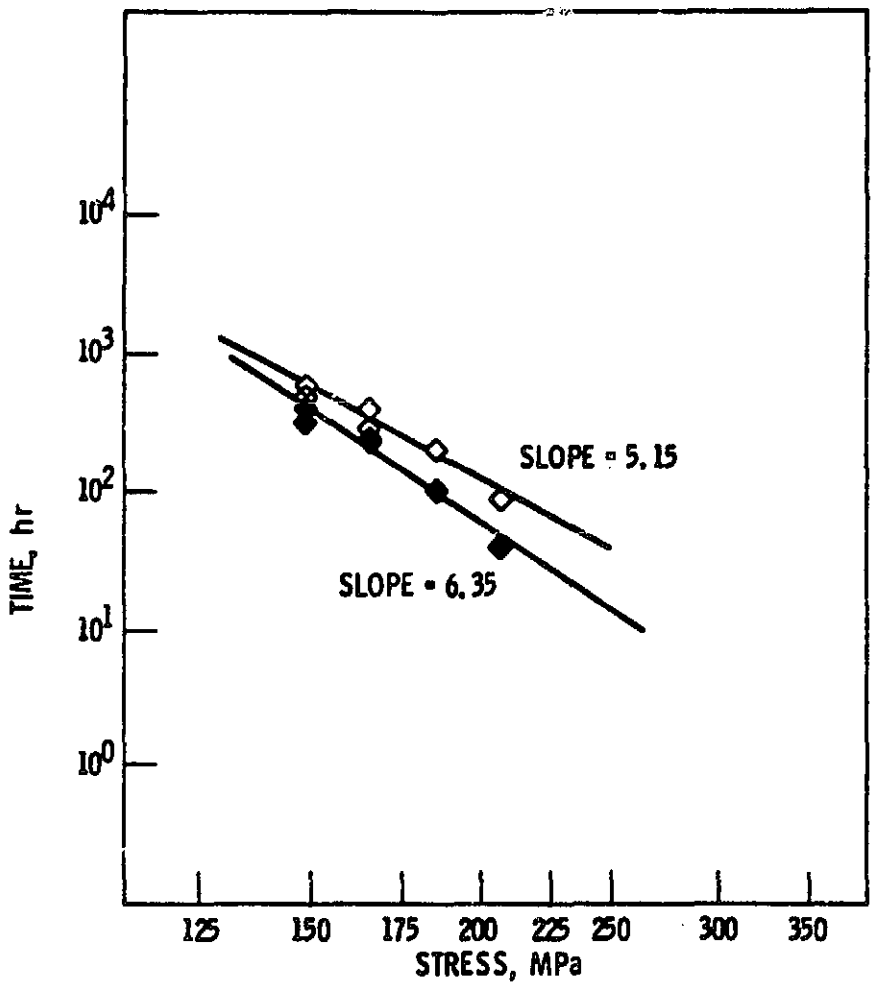

Figure 72. Stress dependence of the time to failure (open symbols) and the time to the onset of tertiary creep (filled symbols) for Alloy E at 1000°C.

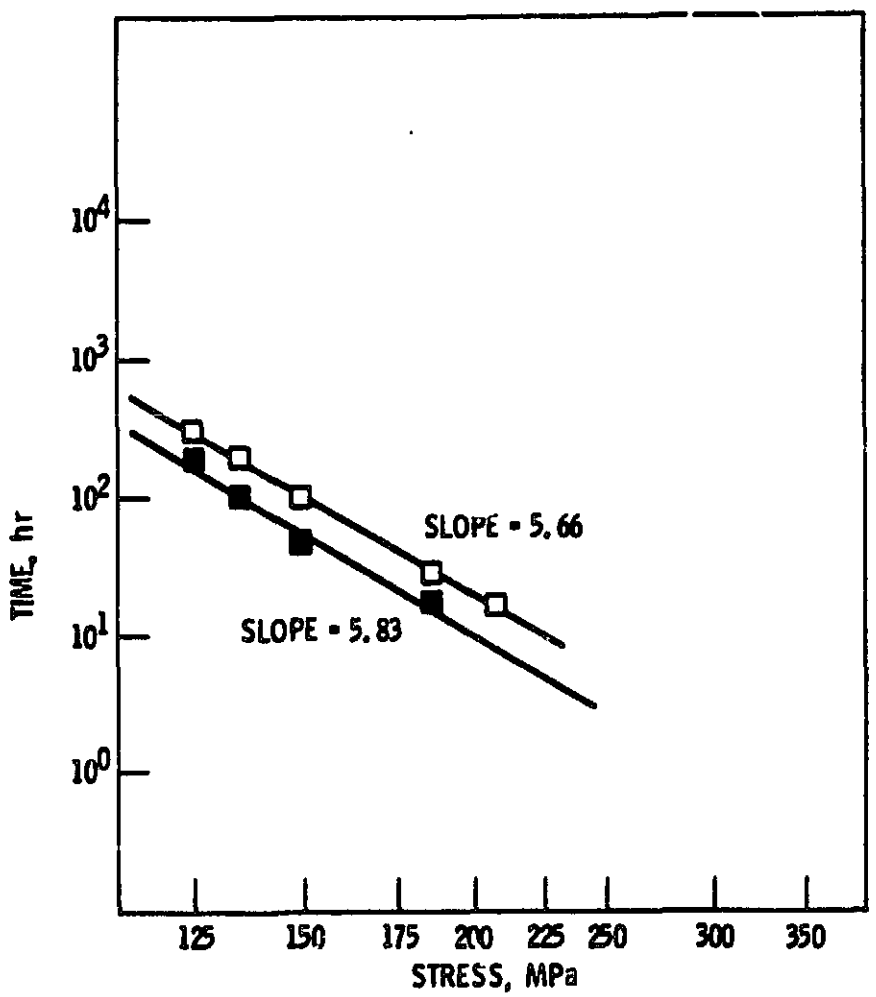

Figure 73. Stress dependence of the time to failure (open symbols) and the time to the onset of tertiary creep (filled symbols) for Alloy F at 1000°C.

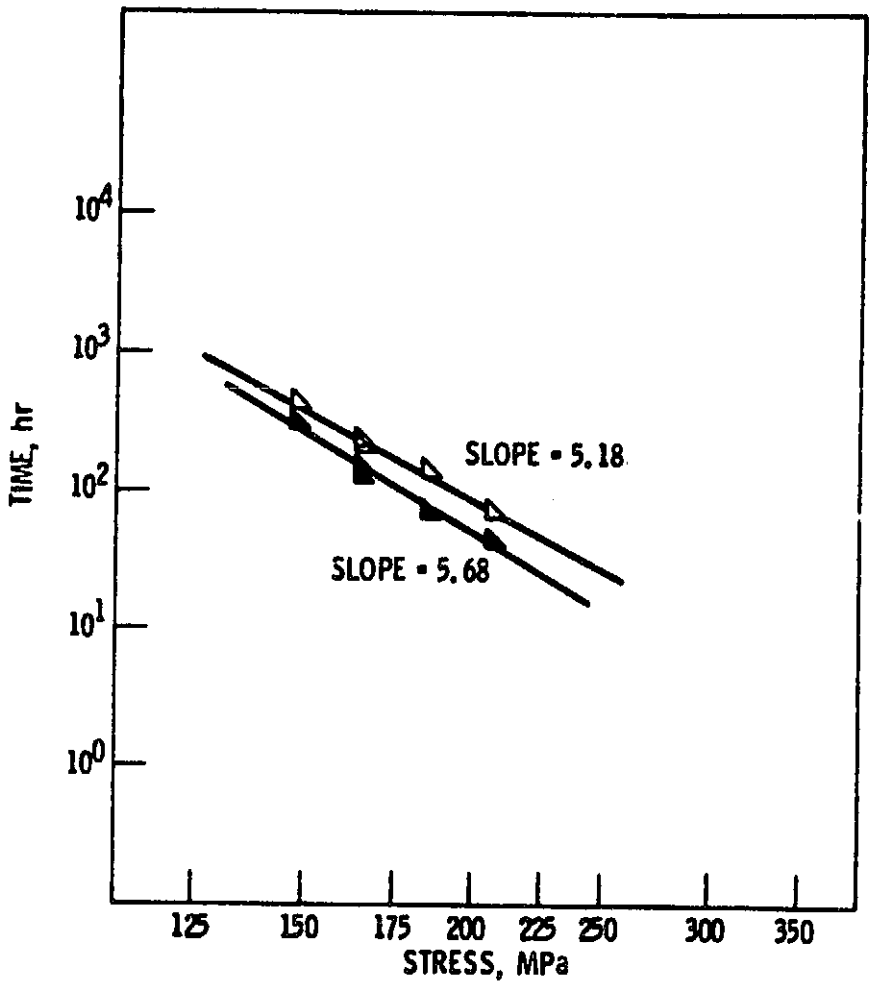

Figure 74. Stress dependence of the time to failure (open symbols) and the time to the onset of tertiary creep (filled symbols) for Alloy G at 1000°C.

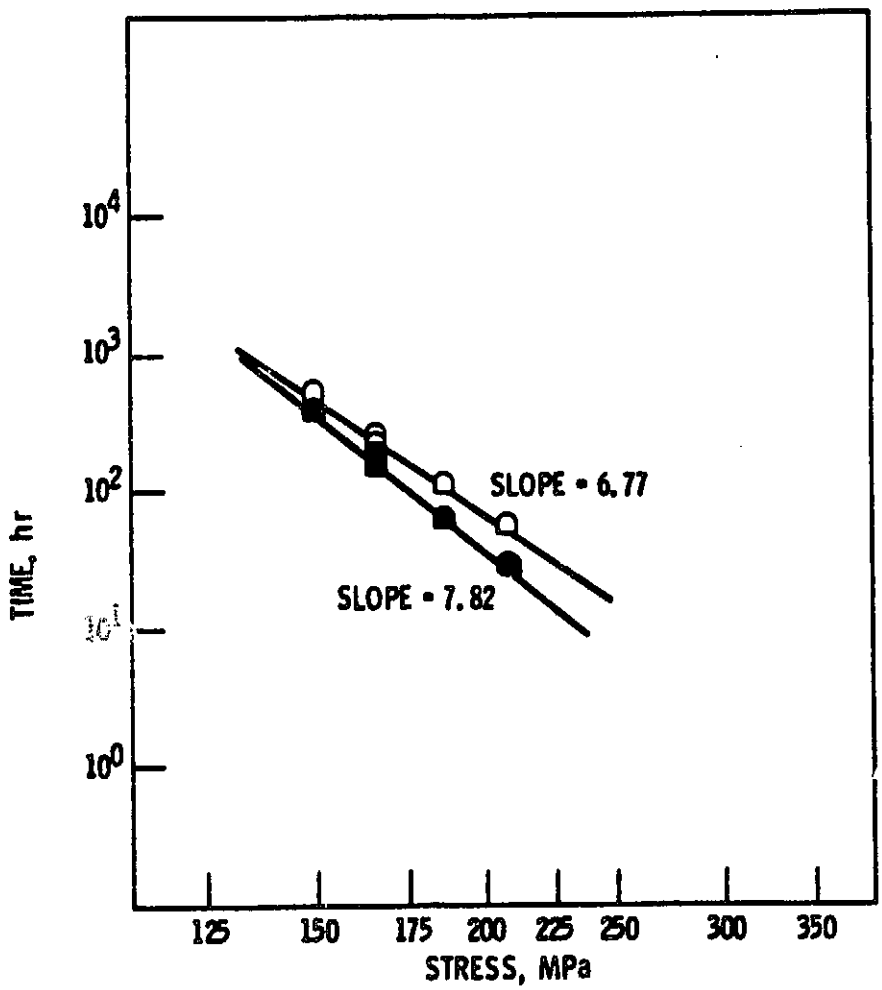

Figure 75. Stress dependence of the time to failure (open symbols) and the time to the onset of tertiary creep (filled symbols) for Alloy H at 1000°C.

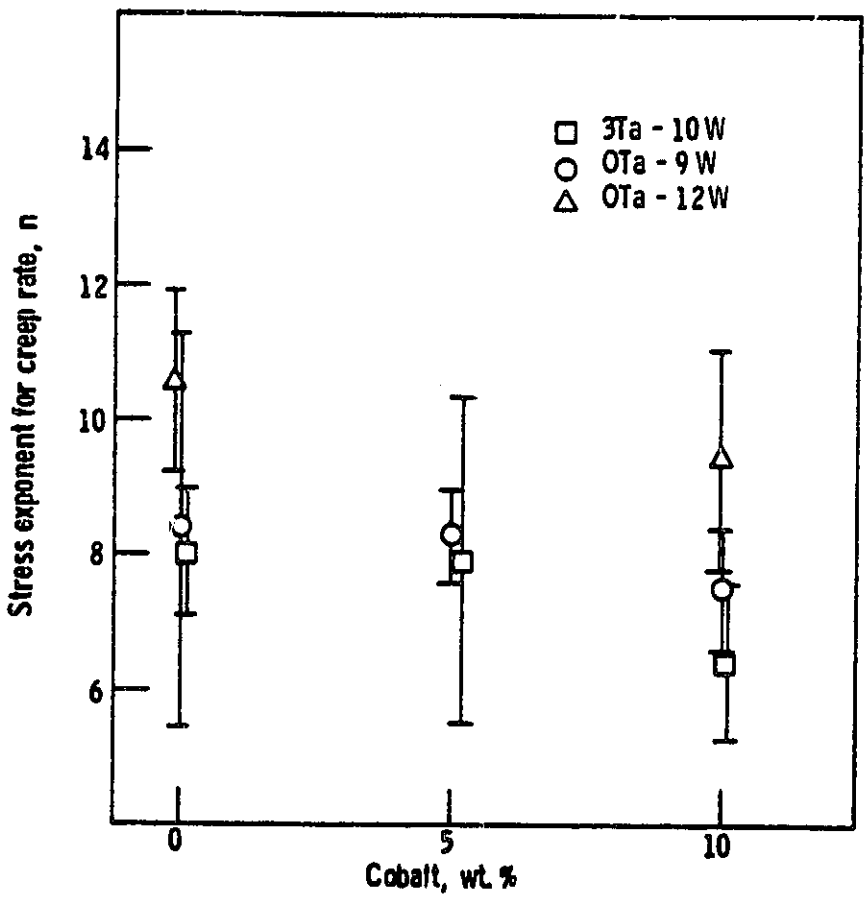

Figure 76. Stress exponent n for steady state creep of single crystal alloys at 1000°C.

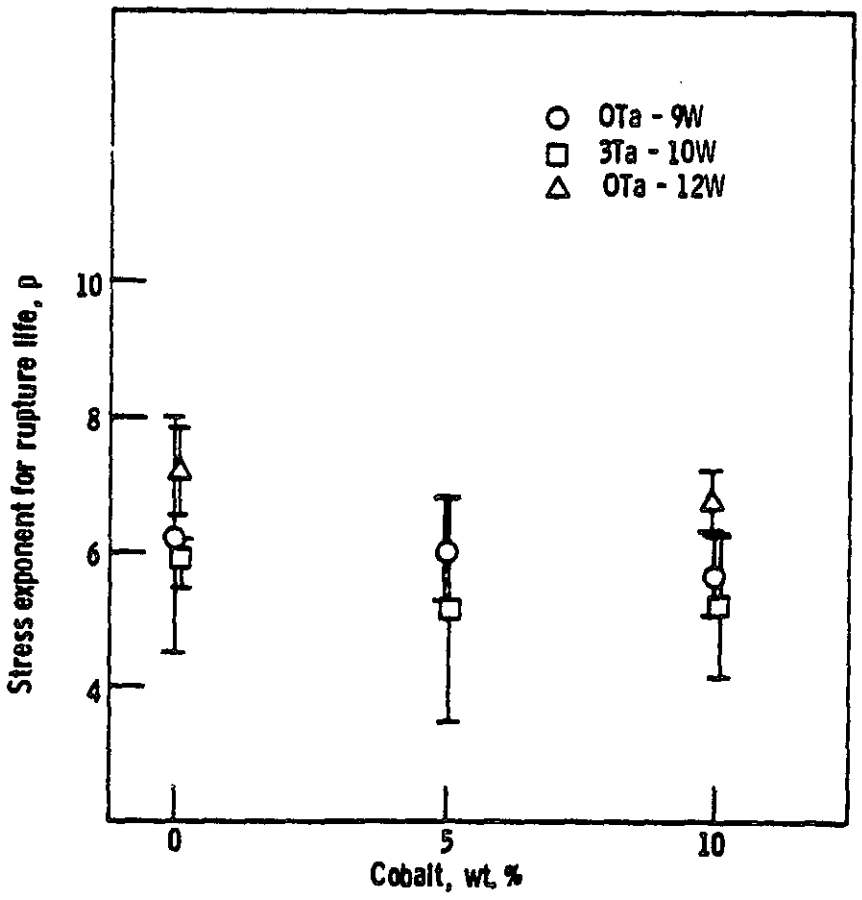

Figure 77. Stress exponent p for the rupture lives of the single crystal alloys at 1000°C.

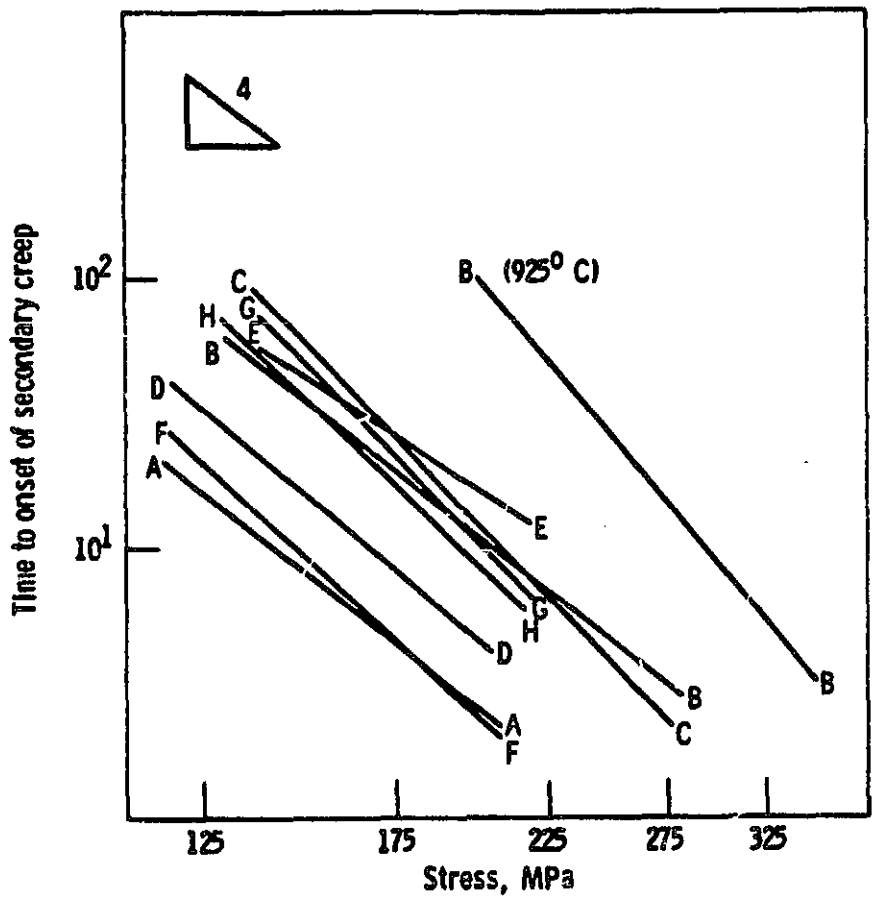

Figure 78. Summary plot of the stress dependence of the time to the onset of secondary creep of the single crystal alloys at 1000°C, and for Alloy B at 925°C.

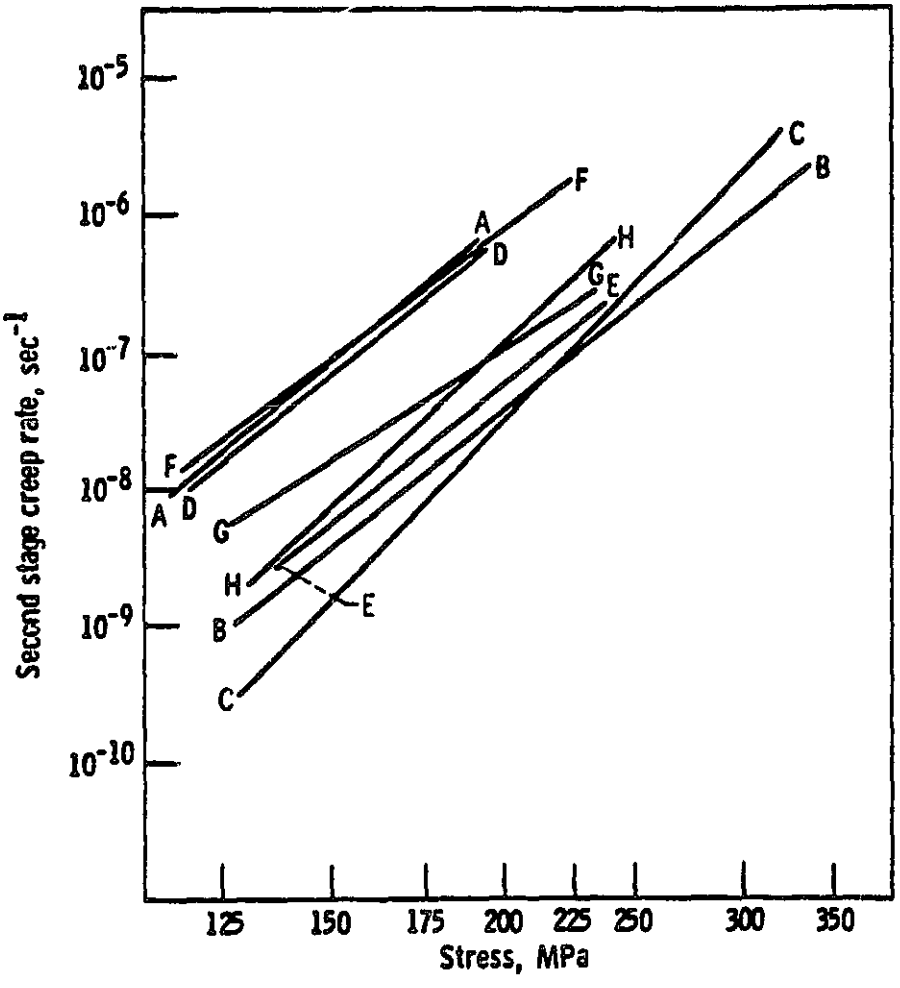

Figure 79. Summary plot of the stress dependence of the steady state creep rate of the single crystal alloys at 1000°C.

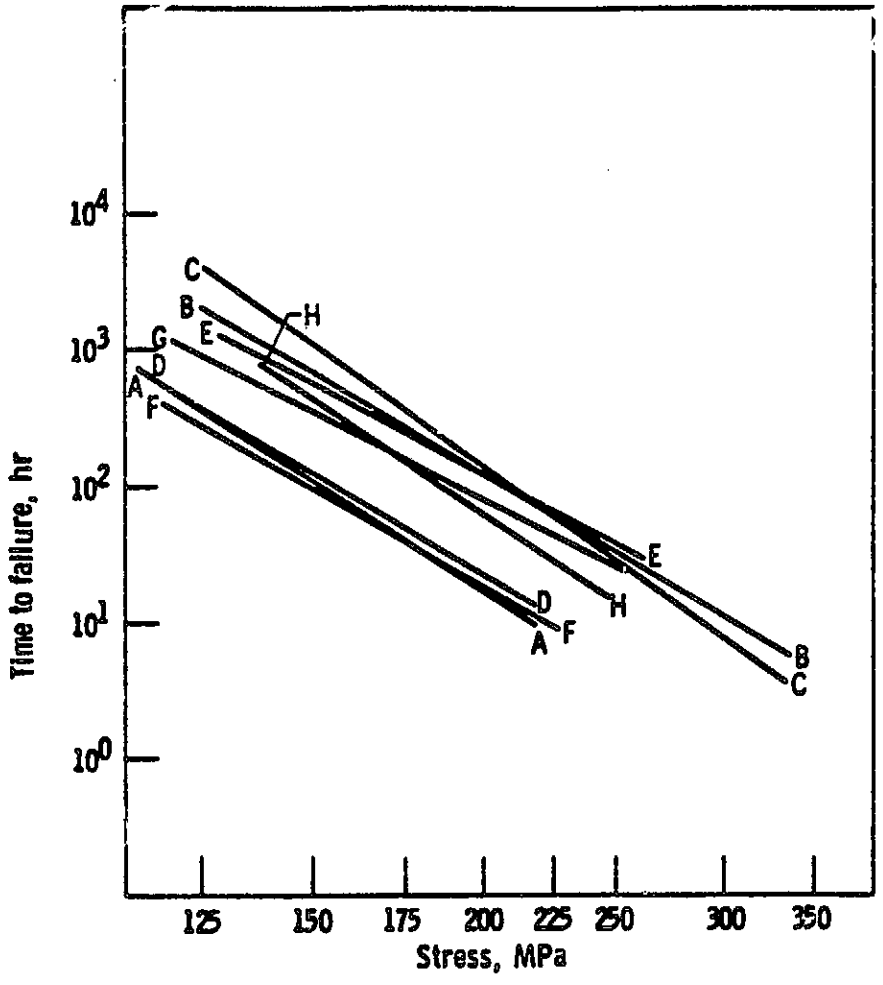

Figure 80. Summary plot of the stress dependence of the rupture lives of the single crystal alloys at 1000°C.

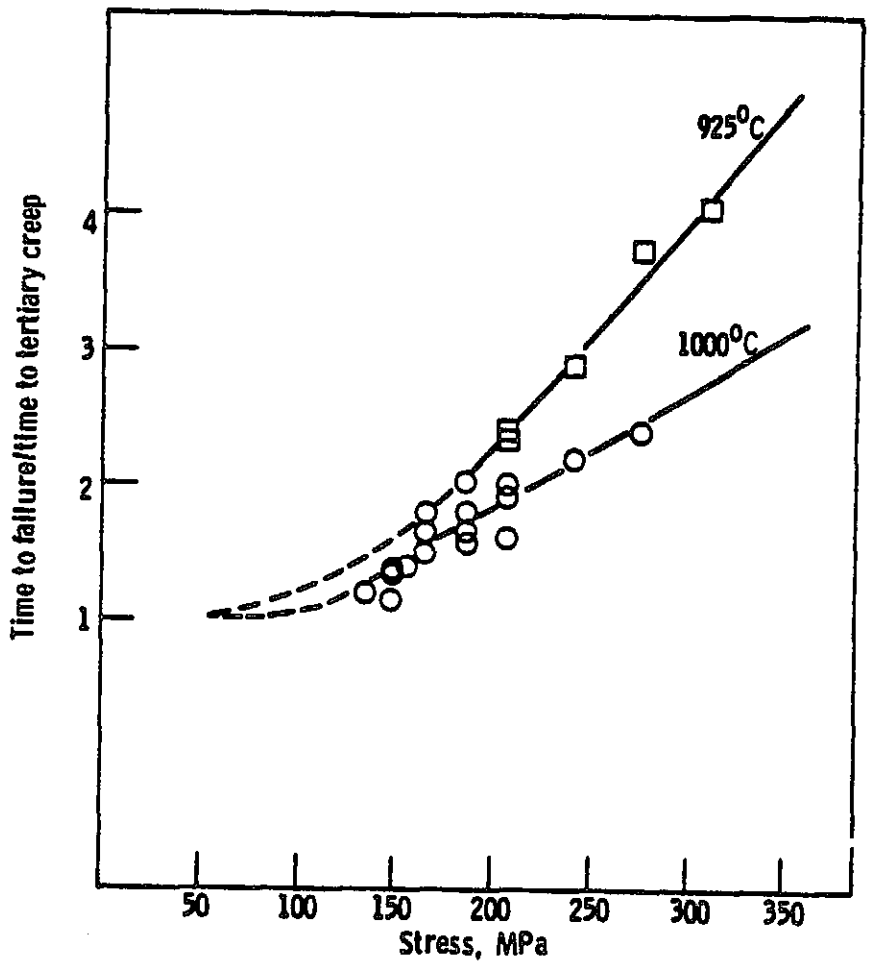

Figuure 81. Stress dependence of the ratio of time to failure over the time to the onset of tertiary creep for Alloy B at 925 and 1000°C.

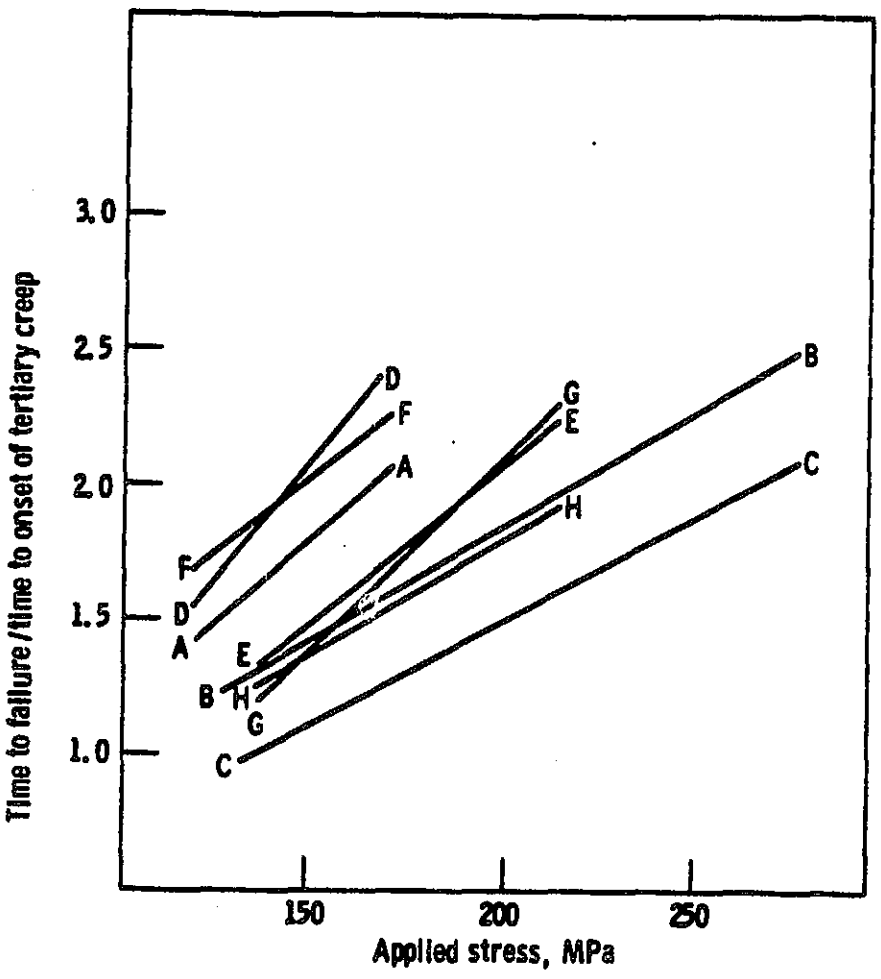

Figure 82. Stress dependence of the ratio of time to failure over the time to the onset of tertiary creep for the single crystal alloys at 1000°C.

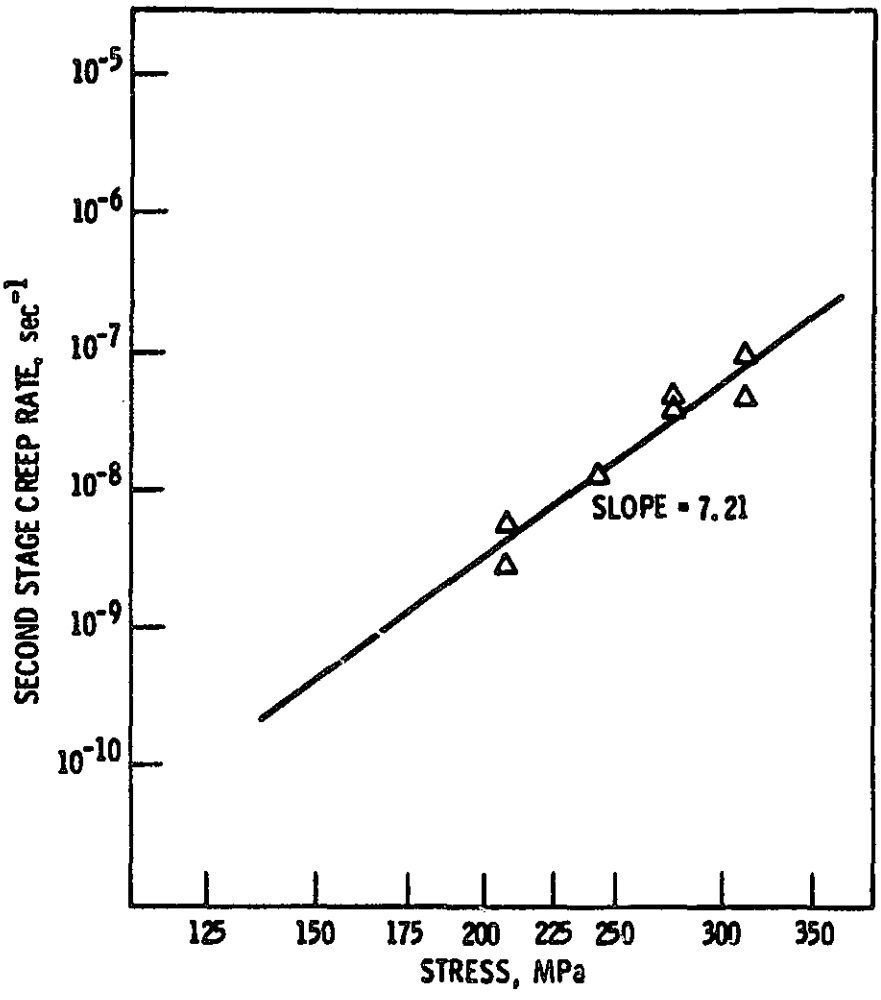

Figure 83. Stress dependence of the steady state creep rate of Alloy B at 925°C.

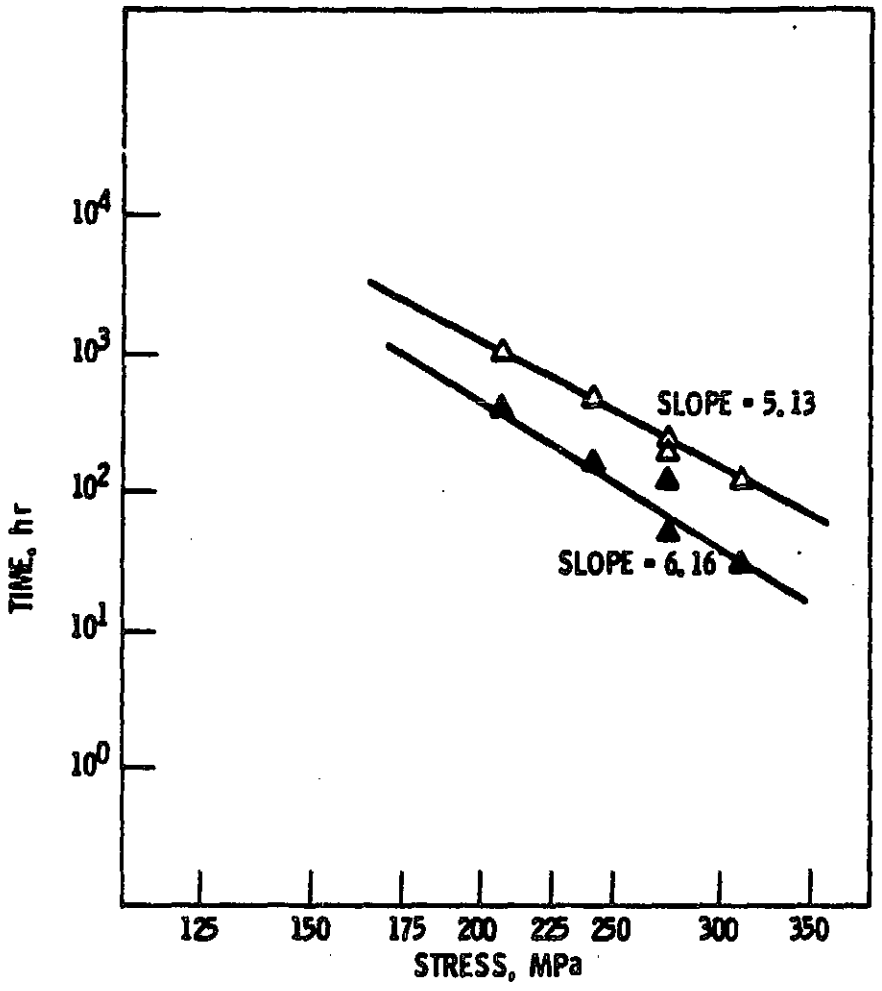

Figure 84. Stress dependence of the time to failure (open symbols) and the time to the onset of tertiary creep (filled symbols) for Alloy B at 925°C.

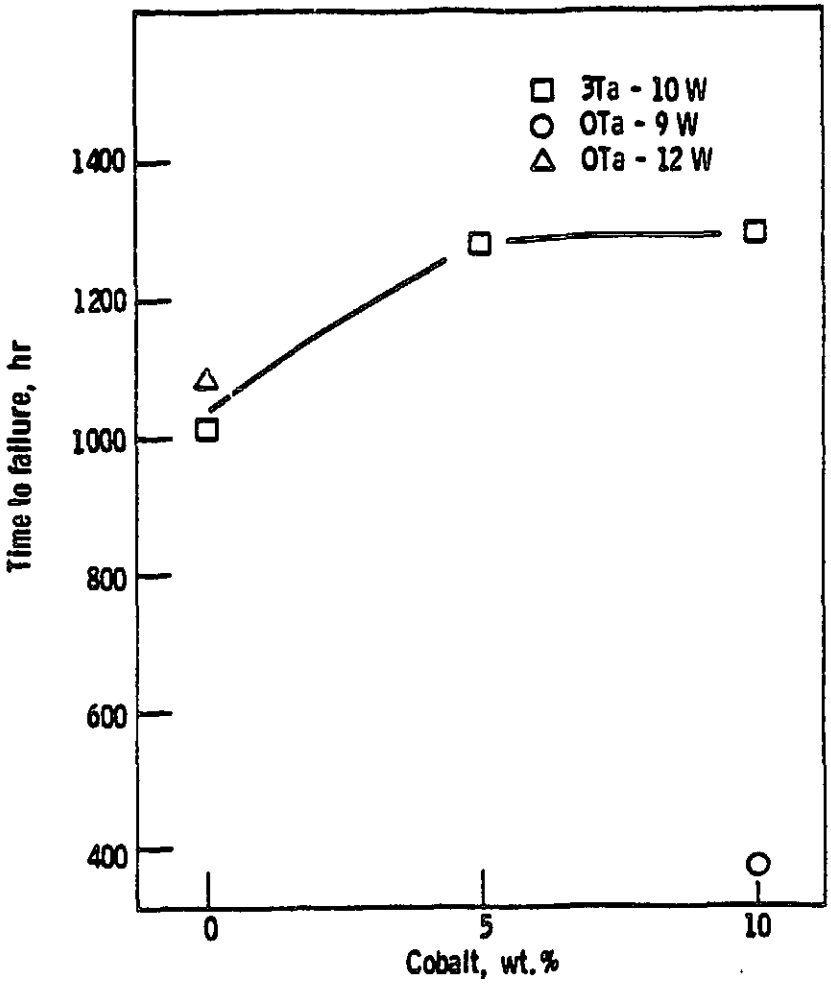

Figure 85. Rupture lives of the single crystal alloys at 925°C and 148 MPa.

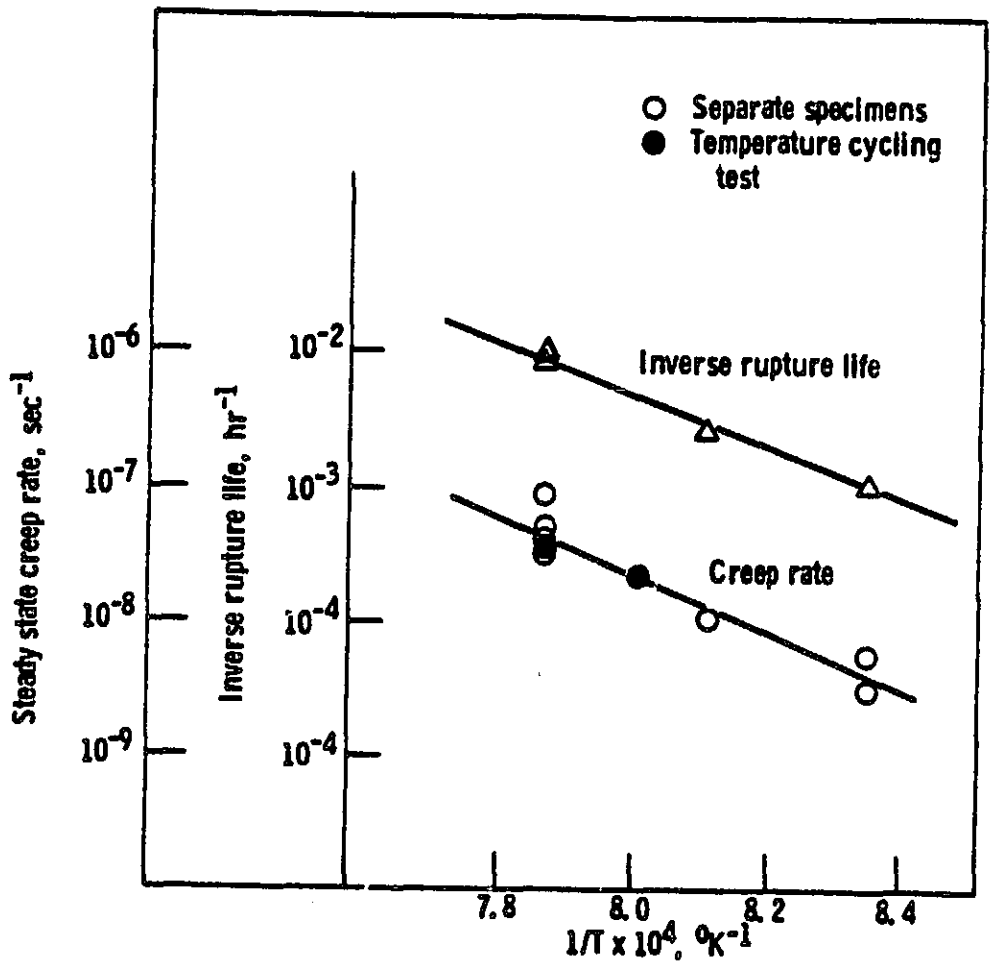

Figure 86. Temperature dependence of the steady state creep rate and the inverse rupture life of Alloy B at 148 MPa.